Republic of Iraq
Ministry of Higher Education
and Scientific Research
University of Babylon / College of Science
Chemistry Department

Adsorption of Human Blood Proteins on the Surface of Some Synthesized Nanocomposite

A thesis
Submitted to the Council of the College of Science,
University of Babylon in a Partial Fulfillment of the
Requirements for the Degree of Doctorate of
Philosophy in Chemistry

By

Assel Amer Hadi Abd Al-Razzaq

B.Sc. College of Science - University of Babylon 2007

M.Sc. College of Science - University of Babylon 2018

Supervised By

Prof.Dr. Nada Yahya Fairooz

Prof.Dr. Hussein Kadhem Al-Hakeim

2022 A.D **1444 A.H**

يَرْفَعِ اللَّهُ الَّذِينَ آمَنُوا مِنكُمْ وَالَّذِينَ
أُوتُوا الْعِلْمَ دَرَجَاتٍ وَاللَّهُ بِمَا
تَعْمَلُونَ خَبِيرٌ

سورة المجادلة: الآية 11

Supervisor Certification

We certify that this thesis entitled, "***Adsorption of Human Blood Proteins on the Surface of Some Synthesized Nanocomposite***" was prepared under my supervision, by "*Assel Amer Hadi Abd Al-Razzaq*". It was done at the Department of Chemistry, College of Science at the University of Babylon in partial fulfillment of the requirement for the degree of **Doctorate** of Philosophy in chemistry at the University of Babylon and this work has never been published anywhere else.

Signature:
Name: **Prof.Dr.**
Nada Yahya Fairooz
Title: Professor
Address: Babylon University
College of Science, Chemistry
Date: / / 2022

Signature:
Name: **Prof.Dr.**
Hussein Kadhem Al-Hakeim
Title: Professor
Address: Kufa University
College of Science, Chemistry
Date: / / 2022

In view of the available recommendation, I forward this thesis for debate by the examining committee.

Signature:
Name: **Prof.Dr.**
Abbas Jasim Atiyah
Title: Professor
Address: Head of Department
Date: / / 2022

Committee Certification

We, the examiner committee, certify that we have read the thesis entitled "**Adsorption of Human Blood Proteins on the Surface of Some Synthesized Nanocomposite**" and examined the student (*Assel Amir Hadi Abd Al-Razzaq*) in its contents at 10 / 10 / 2022, and that in our opinion it is accepted as a thesis for the degree of **Doctorate** of Philosophy in chemistry with (**Excellent**) estimation.

Signature:
Name: **Dr. Abbas Jasim Atiyah**
Title: Professor
Address: Babylon University
College of Sciences, Chemistry
Date: / / 2022
(**Chairman**)

Signature:
Name: **Dr. Mahmoud Hussein Hadwan**
Title: Professor
Address: Babylon University
College of Sciences, Chemistry
Date: / / 2022
(**Member**)

Signature:
Name: **Dr. Amer Musa Juda Al-Shamari**
Title: Professor
Address: Kufa University
College of Sciences, Chemistry
Date: / / 2022
(**Member**)

Signature:
Name: **Dr. Oraas Adnan Hatem**
Title: Assistant Professor
Address: Qadisiyah University
College of Sciences, Chemistry
Date: / / 2022
(**Member**)

Signature:
Name: **Dr. Ahmed Hadi Abdulameer**
Title: Professor
Address: Karbala University
College of Sciences, Chemistry
Date: / / 2022
(**Member**)

Signature:
Name: **Dr. Nada Yahya Fairooz**
Title: Professor
Address: Babylon University
College of Sciences, Chemistry
Date: / / 2022
(**Member and Supervisor**)

Signature:
Name: **Dr. Hussein Kadhem Al-Hakeim**
Title: Professor
Address: Kufa University
College of Sciences, Chemistry
Date: / / 2022
(**Member and Supervisor**)

Approved by the College Committee on Graduate Studies

Signature:
Name: **Prof.Dr. Faiz Ali Rashid Al-Hamad**
Title: Professor
Address: Dean of College of Science – University of Babylon.
Date: / / 2022

Declaration

I, *Assel Amer Hadi Abd Al-Razzaq*, the researcher, who conducted this study entitled **"*Adsorption of Human Blood Proteins on the Surface of Some Synthesized Nanocomposite*"** was submitted in a partial fulfillment of the requirements of a ***Ph.D.*** in Chemistry. The research was carried out during the period **15-9-2019 to 15-9-2022** at the Department of Chemistry, College of Science, University of Babylon**.**

The study was carried out under the supervision of *Prof.Dr. Nada Yahya Fairooz* at the Department of Chemistry, College of Science, University of Babylon and *Prof.Dr. Hussein Kadhem Al-Hakeim* at the Department of Chemistry, College of Science, University of Kufa.

I confirm that the work presented in this thesis has not been previously submitted for a degree Ph.D. at any higher educational institute. In addition, I declare that all the information in this document has been obtained and presented in accordance with academic rules and ethical conduct, I have fully cited and referenced all material and results that are original to this work or where information has been derived from other sources, I confirm that this has been indicated in this thesis.

Assel Amer Hadi

Dedications

To the pure soul that never left me. my father … who taught

me the meaning of life,

To my mother … who light of hope in

my success way,

To my sisters … who supported

me all time

To my love … my wife

To my hope …my sons Karam, Hassan

To my friends … who supported

me all time

I dedicate my little dream

Acknowledgements

In The Name of Allah Most Gracious, Most Merciful

In the beginning, I would like to express my great appreciation to the Almighty, Allah for His support in enabling me to complete this dissertation.

Special thanks go to my supervisor ***Prof.Dr. Nada Yahya Fairooz*** *and* ***Prof.Dr. Hussein Kadhem Al-Hakeim,*** *my supervisors, greatly for enriching my knowledge.*

I would like to express my deep and special thanks to my Mother, my Sisters, my Wife, and my sons, Karam and Hassan.

I wish to thank Babylon University, the Faculty of Science, and the Department of Chemistry for offering me the scholarship and facilitating.

In addition, I would like to thank all Chemistry staff members, the Department of Chemistry for their help and inspiration.

Also, I would like to express my deep and special gratitude to my best friends, who helped and encouraged me a lot three years ago.

Finally, I am deeply indebted to the members of my parent's in-laws' for their love, blessing, and good wishes.

Assel Amer Hadi

Summary

For the first time, the present study involves the separation of valuable proteins (luteinizing hormone (LH) and follicle-stimulating hormone (FSH)) from human serum, which is a novel idea for extracting a trace amount of valuable proteins from the serum of patients with polycystic ovary syndrome (PCOS). Those patients were chosen because they have elevated serum levels of those proteins by new nanoparticle composites (NPs-composites). Three new composites were prepared by coating the metal oxides with graphene oxide (GO) and chitosan (CS) layers. The new synthesized NPs-composites were CS/GO-SeO_2-NPs, CS/GO-MnO_2-NPs, and CS/GO-MoO_2-NPs used to extract LH and FSH from the serum of patients with patients PCOS. A total number of the study's specimens was 150 patients and a control group. They were divided into the following: 120 (PCOS) women patients, and the control group of 30 women. Their age range was 20-45 years for both patients and controls. The samples were collected from Merjan Hospital, Al-Imam Al-Sadiq Hospital, and Babylon Hospital for Women and Children in Babylon Governorate-Iraq during the period from 9 May 2021 until 30 August 2021.

Adsorption-desorption of these hormones on the surface of the prepared NPs-composites was studied extensively to determine the thermodynamic function of the adsorption process, in addition to the study of the effect of the serum components on the quantity of hormone adsorbed on the surface of NPs-composites.

The NPs-composites were prepared by the co-precipitation method and their structures were identified by the usual characterization methods including X-rays diffraction (XRD), fourier transform infrared spectroscopy (FTIR), scanning electron microscopy (SEM), and Energy Dispersive X-rays spectroscopy (EDX), Dynamic light scattering (DLS), and zeta potential analysis (ZPA). The concentrations of hormones in serum and solutions were measured by enzyme-linked immunosorbent assay (ELISA).

The results showed that adsorption percentages of FSH proteins on CS/GO-MnO_2-NPs, CS/GO-SeO_2-NPs, and CS/GO-MoO_2-NPs were 61.97%, 55.91%, and 31.52% ng/gm, respectively. The adsorption percentage of LH proteins on the same NPs-composites sequence were 27.49%, 14.57%, and 12.53% ng/gm, respectively. The adsorption isotherms were calculated using Freundlich's equation at three different temperatures (298, 308, 318K), and the Van't Hoff's lines for adsorption of hormones (FSH, LH) were constructed.

The adsorption of FSH on all the NPs composites was exothermic, while the adsorption of LH on all the NPs composites was endothermic, indicating the effect of the structure of protein on the nature of forces between the hormone and NPs composite surfaces. The adsorption and desorption of the hormones on the surfaces of the prepared NPs composites are affected by the concentration of biochemical that are normally present in the serum such as divalent cations and certain proteins in different ways. The results of the present study indicated the ability of the prepared NPs composites to adsorb FSH and LH effectively from human serum and the quantity adsorbed can be enhanced by modifying temperature and the

serum components as a cheap, easy, and applicable way to extract these valuable hormones in a reasonable amount.

The results also showed various effects of the blood components from PCOS patients (calcium, magnesium, albumin levels, prolactin levels, and μ-opioid receptor (MOR)) on the amounts of LH and FSH that adsorbed on the surfaces of the prepared composites. The relationship between serum components and the amount of FSH hormone uptake on the surface of CS/GO-SeO_2-NPs was a significant correlation between serum albumin ($r = 0.652$, $p < 0.01$) and Albumin / Ca ($r = 0.674$, $p<0.01$) with the amount of FSH adsorbed. There is a significant correlation between the amounts of adsorbed FSH on CS/GO-MoO_2-NPs with serum albumin ($r =0.405$, $p<0.01$) and magnesium ($r =0.321$, $p<0.01$) and prolactin ($r =-0.243$, $p<0.01$). Regarding the adsorption of FSH on CS/GO-MnO_2-NPs surface, the results showed a significant correlation between the FSH adsorbed and serum albumin ($r =0.415$, $p<0.01$), magnesium ($r =0.387$, $p<0.01$), and prolactin ($r =-0.269$, $p<0.01$).

The relationship between serum components and the amount of LH hormone uptake on the surface of CS/GO-SeO_2-NPs was a significant correlation between serum albumin ($r =-0.435$, $p<0.01$) and calcium ($r =0.321$, $p<0.01$) with the amount of LH adsorbed. There is a significant correlation between the amount of LH adsorbed on CS/GO-MoO_2-NPs surface with serum albumin ($r =-0.452$, $p<0.01$) and calcium ($r =0.299$, $p<0.01$). As for the adsorption of LH on CS/GO-MnO_2-NPs surface, the results showed a significant correlation between the LH adsorbed and serum albumin ($r =-0.306$, $p<0.01$), calcium ($r =0.316$, $p<0.01$), MOR ($r =0.280$, $p<0.01$) and prolactin ($r =0.194$, $p<0.01$).

Table of Contents

List of Tables

Table of Figures

Table of Abbreviations and Symbols

Abbreviations and Symbols	*The Meaning*
Abs	Absorbance
ABPs	Androgen Binding Proteins
ASRM	American Society for Reproductive Medicine
BMI	Body Mass Index
B.D.H	British Drug House
β	Linear Broadening
C	Concentration
C_o	Initial Concentration
C_e	Equilibrium Concentration
CD	Circular Dichroism
CS	Chitosan
^0C	Centigrade
CRP	C-reactive protein
D	Crystallite Size
1D	One Dimensional
DLS	Dynamic Light Scattering
DI	Deionized Water
ELISA	Enzyme-Linked Immunosorbent Assay
EIA	Enzyme Immunoassay
EDX	Energy Dispersive X-rays Spectroscopy
FED	Field Emission Devices
FSH	Follicle Stimulating Hormone
FTIR	Fourier Transform Infrared Spectroscopy
GO	Graphene Oxide
GnRH	Gonadotrophin Releasing Hormone
HCG	Human Chorionic Gonadotrophin
HPH	High-Pressure Homogenization
K	The Scherrer Constant
k	Empirical Constants for Adsorbent
Kf	Freundlich Constants
LH	Luteinizing Hormone
m	Mass of Adsorbent

MNPs	Medical Nanoparticles
MS	Mass Spectroscopy
n	Empirical Constants for Adsorbate
NPs	Nanoparticles
NMs	Nanomaterials
NMR	Nuclear Magnetic Resonance
NIH	National Institutes of Health
OHSS	Ovarian Hyperstimulation Syndrome
PC	Protein Corona
PCOS	Polycystic Ovary Syndrome
PCOM	Polycystic Ovary Morphology
PLA	Pulsed Laser Ablation
PLD	Pulsed Laser Deposition
PTH	parathyroid hormone
q	quantity of Adsorbate
rho	The Spearman’s Correlation Coefficient
rpm	Revolutions Per Minute
SEM	Scanning Electron Microscopy
TMB	Tetra methyl Benzidine
TSH	Thyroid Stimulating Hormone
V	Volume of Solution
WR	Working Reagent
X	The Quantity Adsorbed
X	Mass of Adsorbent
XRD	X-rays Diffraction
ZPA	Zeta Potential Analysis
Ɵ	Diffraction angle (Bragg's angle)
ƛ	Wavelength of X-rays reaction

Chapter 1
Introduction & Literature Survey

Introduction

1.1 Nanomaterials

Nanomaterials (NMs) have risen to prominence in technological breakthroughs as a result of their tunable physical, chemical, and biological properties, as well as their superior performance over bulk counterparts. The size, content, shape, and origin of NMs are used to classify them [1]. Nanomaterials are chemical substances or materials manufactured and used at a very small scale [2]. Nanomaterials are created to have unique properties compared to materials that do not have nanoscale features, such as greater strength, chemical reactivity, or conductivity [3].

Nanocomposites are frequently released into the circulation for biomedical purposes such as drug or gene delivery, which is populated by blood cells and a variety of tiny peptides, proteins, carbohydrates, lipids, and complexes of these molecules [4]. Generally, different biomolecules cover a nanoparticle's surface in biological fluids, which influence nanocomposite interactions with tissues and, finally, its fate [5]. The creation of a "corona" is the result of molecules adhering to the nanomaterial. Although small proteins account for the majority of adsorbed chemical moieties, the corona can be formed by any blood particle component [6]. The surface charge and morphology of the nanoparticle appear to distinguish the different coronas, although the specific laws of surface-protein adsorption are unknown [7]. Our comprehensive examination of these issues could aid in the development of appropriate

nanomaterials for specialized medication delivery [8]. Structure of Nanomaterials is shown in figure 1.1.

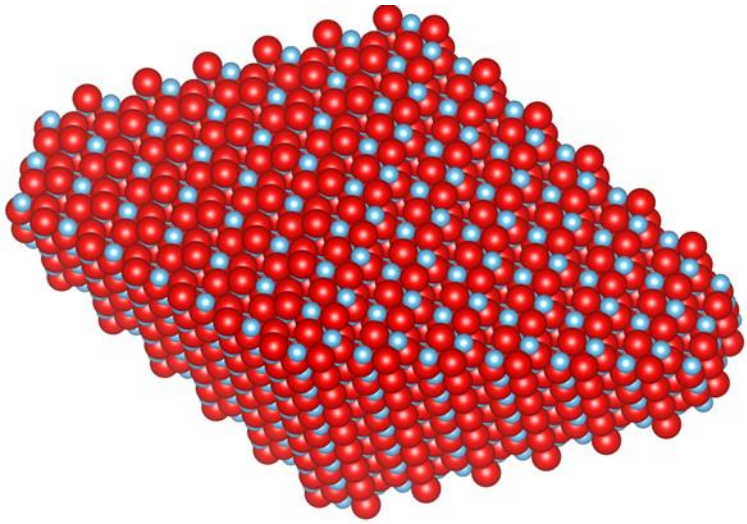

Figure 1.1 Nanomaterials Structure [8]

1.1.1 Definition of Nanomaterial

Nanomaterials are materials with a single unit that is between 1 and 100 nanometers in size (in at least one dimension) [9]. Nanomaterials can occur naturally, be created as the by-products of combustion reactions, or be produced purposefully through engineering to perform a specialized function. These materials can have different physical and chemical properties than their bulk-form counterparts [10]

1.1.2 Properties of Nanomaterials

Nanomaterials have distinct features from their bulk counterparts that confer positive traits; yet, they may also endow them with distinct toxicity pathways. Toxicity is hypothesized to be caused by the size and surface area of nanomaterials, as well as their composition and forms.

1.1.2.1- Size and Surface Area of the Particles

The interaction of materials with biological systems is heavily influenced by particle size and surface area. Reduced material size appears to result in an exponential rise in surface area relative to volume, making the nanomaterial surface more reactive to itself and its surrounding environment. It's worth noting that particle size and surface area have an impact on how the system reacts to, distribute, and remove materials [11]. Various biological systems, such as endocytosis, cellular uptake, and particle processing efficiency in the endocytic pathway, are dependent on the size of the material [12]. NPs of various sizes have been tested in *vitro* for cytotoxicity utilizing a variety of cell types, culture conditions, and exposure lengths by a number of studies [13]; However, due to the more complicated structure of biological systems, in *vivo* evaluation is difficult and requires a more full understanding of the particles [14], Despite the fact that several writers have evaluated their toxicity in biological systems using various in *vivo* methodologies [14]. The ability of nanoparticles to infiltrate biological systems [15] and then affect the structure of numerous macromolecules [16], consequently interfering with important biological activities, is generally attributed to their size-dependent toxicity.

One of the key mechanisms for in *vivo* toxicity is the development of oxidative reactions through the formation of free radicals, in which size plays an important role, as many authors have pointed out: the smaller size, is more capable to formation [17]. Free radicals have been shown to pose a threat to biological systems, primarily through DNA damage, lipid oxidation, and the resulting inflammatory reactions [18]. Although the size and surface area of nanoparticles are significant in determining their toxicity, other factors such as chemical composition of the contents may also contribute to the nanoparticles' inherent toxicity.

1.1.2.2- Effect of Particle Shape and Aspect Ratio

Although significant gains have been made in our understanding of the relationship between particle size and shape in order to create a more effective nanomaterial-based targeted delivery system, this also highlights the necessity to examine their adverse impacts. Nanomaterials come in varied shapes, including fibers, rings, cubes, spheres, and planes [19]. Essentially, shape-dependent nanotoxicity affects the membrane encapsulation processes in *vivo* [20]. It has been observed that spherical nanoparticles are easier and faster than rod-shaped or fiber-like nanoparticles [21]. Furthermore, regardless of whether they are homogeneous or heterogeneous, spherical nanoparticles are less toxic [22]. Nanomaterials that are not spherical are more likely to flow into capillaries, creating additional biological effects [23]. Furthermore, it has been discovered that the higher the aspect ratio, the greater the particle toxicity [24].

The advanced synthesis of nanomaterials makes it possible to obtain their desired size, shape, composition, and surface chemistry, as well as to control their dispersion properties. Nanomaterials, such as zero dimensional (0D) fullerenes, 1D nanotubes, 2D graphene, and 3D graphite, are probably the most promising materials for this purpose because of their excellent properties, e.g., high thermal conductivity coupled with high aspect ratio and low density [25].

1.1.2.3- Effect of Surface Charge

The surface charge of nanoparticles is also crucial for their toxicity since it determines how they interact with biological systems. The selective adsorption of nanocomposites is one of the many characteristics of nanomaterials [26], colloidal behavior, and plasma protein binding [27]. Recently, zwitterion nanocomposites were found to allow long circulation, favorable distribution in the tumor area, and optimal tumor penetration and thus support the hypothesis that zwitterion oxide nanoparticles could be an excellent solution for diagnostic imaging and therapeutic applications in nano-oncology [28]. Positively charged nanoparticles, in contrast to negatively charged and neutral nanoparticles, display considerable cellular absorption due to their improved opsonization by plasma proteins. Furthermore, they have been demonstrated to produce hemolysis and platelet aggregation, resulting in severe system toxicity because the surface charge is a primary regulator of colloidal behavior [29]. It specifically alters the organism's reaction to nanoparticle exposure by modifying the shape and size of the particles through aggregation or agglomeration formation [26].

1.1.2.4- Effect of Composition and Crystalline Structure

Although particle size is important in predicting nanocomposite toxicity, research showing that the chemistry of different nanocomposites with the same dimensions have similar toxicities cannot be ignored. The content and crystalline structure of nanocomposites have an impact on their toxicity, according to these research [30]. The crystal structure also influences the toxicity of nanocomposites [31]. Furthermore, after interacting with water or another dispersion media, nanoparticles can modify their crystal structure, implying that the solvent has a role in the manifestations of toxicities presented by nanoparticulate systems [32].

1.1.2.5- Effect of Aggregation and Concentration

The toxicity of nanoparticles are also influenced by their aggregation states. The size, surface charge, and composition of NPs all influence their aggregation states [33]. In general, when the concentration of nanoparticles increases, the toxicity of the particles decrease at greater concentrations [34].

1.1.2.6- Effect of Surface Coating and Surface Roughness

The surface features of nanoparticles play a vital role in influencing the result of their contact with cells and other biological entities and thus play a substantial influence on their toxicity. Surface coating can alter nanoparticles' cytotoxic capabilities by altering their physicochemical features, including magnetic, electric, and optical properties, as well as chemical reactivity [35, 36]. The generation of reactive oxygen species is known to be caused by the presence of oxygen, ozone, oxygen radicals, and transition metals on nanoparticle surfaces and the induction of inflammation [18, 37, 38]; these certainly influence their associated toxicities issues. Surface coatings can reduce or eliminate the negative impacts of nanoparticles in general. The correct surface coating, in particular, can lead to nanoparticle stability and the release of hazardous ions from nanomaterials [39]. Surface modifications of NPs using chitosan and other surfactant copolymers have been widely exploited in recent years by the research community in this expanding field of nanotechnology to stabilize nanoparticulate systems in the biological environment [40, 41].

Furthermore, as the attribution of nanoparticles such as surface roughness, hydrophobicity, and charge of nanoparticles influence the phenomena of cellular uptake of nanoparticles [42], they effect on the

toxicity of nanoparticles. The strength of nanoparticle-cell interactions is determined by surface coarseness, which enhances cell adherence. In cell-nanoparticle interactions, the pore structure is crucial.

1.1.2.7- Effect of Solvents / Medium

The particle dispersion and agglomeration state of nanoparticles are known to be affected by medium/solvent conditions, which in turn affects their particle size, influencing the toxicity of nanoparticles. It is also consensus that NPs display different diameters in the biological milieu [43, 44]. As a result, the toxic effects of nanoparticles vary depending on the medium composition in which they are suspended; conversely, when the same nanoparticles are dissolved in different mediums, they exhibit diverse hazardous manifestations [45]. While the dispersion agent may improve the physicochemical and solution properties of nanomaterial formulations, it may also have a negative impact on nanomaterial toxicity.

1.1.3 Methods of Synthesis of Nanomaterials

There are two main approaches to synthesizing nanomaterial or nanoparticles. One is the top-down approach, and another is the bottom-up approach.

1.1.3.1 Top-down Approach (Size reduction from bulk materials)

Top-down approaches [46, 47] rely on milling, high-pressure homogenization, and pulsed laser fragmentation to reduce the size of big materials and break them down into nanometer-sized particles [48, 49]. Milling is done with a revolving apparatus in which particles are combined with milling pearls and rotated continuously, resulting in smaller crystals or amorphous particles [50-52]. High-speed rotation, on the other hand, can

generate a lot of heat, leading thermally sensitive compounds to degrade [53]. Milling can also produce surface activation of drug particles, affecting a variety of physicochemical aspects such as flow ability [54].

For nanocrystal manufacturing, high-pressure homogenization (HPH) is also used. The piston-gap homogenizer and the microfluidizer, in particular, are two common types of homogenizers used for particle size reduction [55]. In this regard, several parameters are critical in HPH, including pressure, cycle number, stabilizer type, the temperature of the process, and stabilizing concentration [56, 57]. Pulsed Laser Ablation (PLA) and Pulsed Laser Deposition (PLD) are advanced procedures that break (inter) molecular connections in bulk materials by absorbing energy and converting it to heat and/or chemical energy [49].

Due to the development of new surfaces, the Gibbs free energy will change during the top-down size reduction process. Thermodynamic instability of nanosuspension will emerge as a result of this. To lower the particle-free energy, appropriate stabilizers are necessary [58]. The process of top-down nano-formulation is discussed elsewhere [50] and is beyond the scope of this review.

1.1.3.2 Bottom-up Approach
(Material synthesis from the atomic level)

The bottom-up approach is based on the precipitation of supersaturated solutions [58]. It's commonly used to make nanosuspensions in bulk solutions as well as single droplets [59]. This method is used in several pharmaceutical processes such as solvent–anti-solvent technique, supercritical fluid processing, spray drying, and emulsion–solvent evaporation [60, 61]. Supersaturation, nucleation, solute

molecule diffusion, and nanoparticle development are all phases in the production of nanoparticles [62]. The bottom-up approach has several advantages, including the ability to produce monodisperse particles with a limited size distribution, minimal energy and low processing temperatures for thermolabile medicines, and no need for expensive equipment [63]. The Bottom-up and the Top-down Approaches in Synthesis shown in figure 1.2.

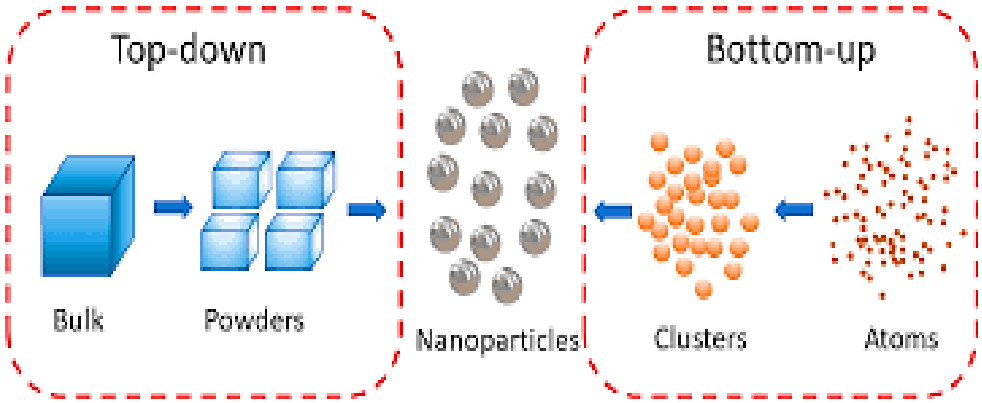

Figure 1.2 Bottom-up and the Top-down Approaches in Synthesis [64].

1.1.4 Types of NPs

1.1.4.1 Metal NPs

Metal nanoparticles offer a wide range of applications in a variety of industries. Because their shapes, sizes, and compositions of nanocomposites are so closely linked to their physical, chemical, and optical capabilities, nanoscale materials-based technologies have been used in a variety of sectors ranging from chemistry to medicine. [65, 66]. Silver nanoparticles (Ag-NPs) are increasingly used in various fields, including medical, food, health care, consumer, and industrial, due to their unique physical and chemical properties. These include biological properties [67], such as antibacterial agents [68], wound dressings, and biomedical devices [69], and for the determination of cytotoxicity [70].

Gold nanoparticles (Au-NPs) are a viable platform for nanobiological assemblies using oligonucleotides due to their ease of functionalization. [71], antibodies [72], and proteins [73]. Au-NPs have many properties that are of great value for diagnosing and treating tumors. Au-NPs are small in size and can penetrate widely and deposit on the tumor site, bind to many proteins and drugs, target delivery drugs, and have good biocompatibility [74].

1.1.4.2 Metal Oxide NPs

1.1.4.2.1 Selenium Oxide (SeO_2)

Selenium (Se) is a vital component of biological processes and a cofactor for antioxidant enzymes including glutathione peroxidases and thioredoxin reductases, which protect the body from free radicals [75, 76]. Selenium is coupled with at least 25 selenoproteins in the human body, each of them has different antioxidant, anti-inflammatory, antiviral, and anticancer properties. [77, 78].

There has been an increase in interest in the manufacture and development of selenium nanoparticles (SeO_2-NPs) in recent years due to their discovery of intriguing (in *vitro* and in *vivo*) biological activity, low toxicity, and high bioavailability [79]. Importantly, these nanoparticles are implicated in antioxidant defense systems and serve a critical role in oxidative stress protection. [80]. SeO_2-NPs are more effective with lower toxicity than Ag-NPs [81]. The most popular chemical approach for generating SeO_2-NPs is a straightforward process involving reducing selenium salts [82]. In the biological synthesis process, microorganisms and plants can synthesize SeO_2-NPs [83]. Water-soluble polymers are excellent stabilizers in the manufacture of selenium colloid by several

researchers [84, 85]. Chitosan is a natural polymer that has been investigated for its high biocompatibility and chemical characteristics, as well as its ability to stabilize various nanoparticles [86].

Selenium nanoparticles (SeO_2-NPs) have a wide range of applications in medical diagnostics and nanobiotechnology due to their increased bioavailability, lower toxicity, and good absorption capacity compared to inorganic and organic forms. [87]. The reduction of oxidative stress [88], anticancer drug delivery carrier [89], protection against metal intoxication [90], and immune-stimulatory effect [91] are some important applications of SeO_2-NPs. Also, SeO_2-NPs were used as chemopreventive agents [92], antimicrobial agents [93, 94], and antifungal agents [95], and therapeutic agents [96]. The SeO_2-NPs have been synthesized via various chemicals [97] and biological methods [98] [75]. Structure of SeO_2-NPs is shown in Figure 1.3.

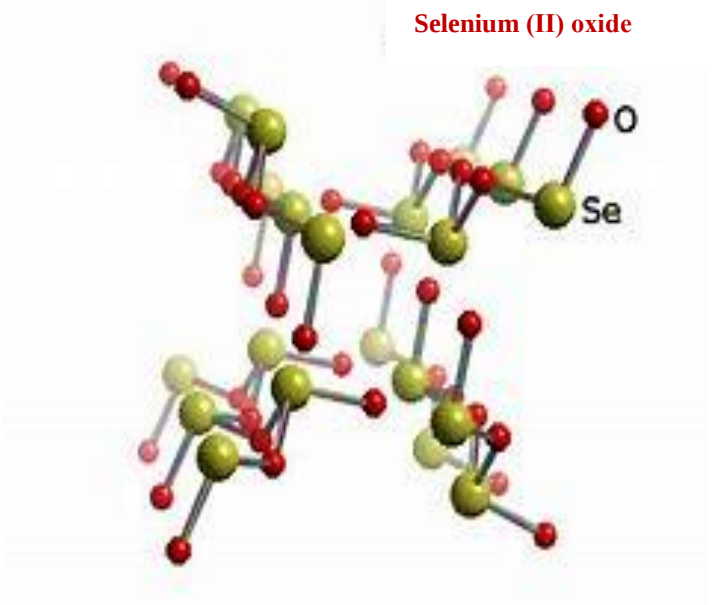

Figure 1.3 Selenium Oxide Structure (SeO_2) [99].

1.1.4.2.2 Molybdenum Oxide (MoO_2)

Molybdenum oxide nanoparticles (MoO_2-NPs) have attracted intensive interest due to their unique catalytic properties. MoO_2 has received a lot of attention as a smart material for catalysis. [100], sensors lubricants, lithium batteries, organic solar cells, and display materials [101]. Recently, significant progress has been made in the size and phase-controlled synthesis of MoO_2 with improved catalytic characteristics. [102, 103]. MoO_2 nanoparticles can be utilized to deliver various novel, profoundly effective, strong, incorporated nanoscale devices, including field emission devices (FED) and photodetectors [104, 105].

Molybdenum not only allows for more cost-effective and practical fuel refining but also helps to create a safer environment. [106]. Structure of MoO_2-NPs is shown in Figure 1.4.

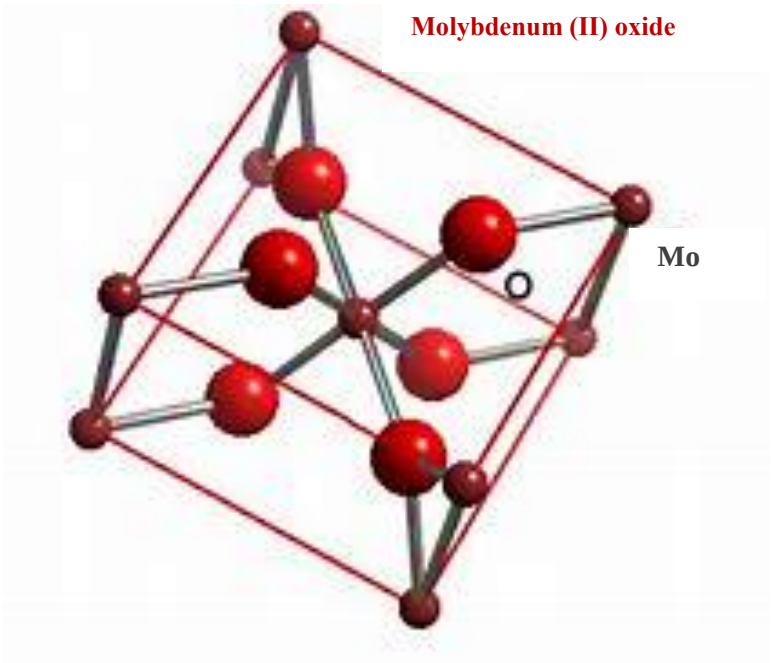

Figure 1.4 Molybdenum Oxide Structure (MoO_2) [107].

1.1.4.2.3 Manganese Oxide (MnO_2)

Manganese dioxide (MnO_2) is an environmentally friendly, low-cost, and plentiful manganese oxide that has outstanding physical and chemical properties under ambient circumstances [108]. Because of its rich polymorphism and structural flexibility, this oxide offers a wide range of applications in catalysis, ion exchange, molecular absorption, microwave absorption, biosensors, and energy storage [109]. These materials are especially important in medical research as contrast agents in magnetic resonance [110] or biosensors [111]. Because of their unique optical, magnetic, mechanical, and electrical properties, nanoscale morphologies have recently received a lot of interest [112]. Low-dimensionality nanostructures, such as one-dimensional (1D), have a distinct behavior among them [108] [113]. To synthesize MnO_2 with discrepant forms, a variety of preparation processes have been used, including hydrothermal [114], sol-gel [115], precipitation [116]. Structure of MnO_2-NPs is shown in Figure 1.5.

Figure 1.5.Manganese Oxide Structure (MnO_2) [117].

1.1.4.3 Organic Nanoparticles (NPs)

Organic nanoparticles (NPs) are templated upon natural or synthetic organic molecules. Nature provides many examples of organic NPs such as protein aggregates, lipid bodies, milk emulsions, or more complex organized structures such as viruses [118]. This nanoparticle is primarily composed of organic substances, such as lipids, proteins, and/or carbohydrates. Examples of these organic NPs are provided, highlighting their synthetic route and their physicochemical properties. Zheng et al. (2017) have designed a top-down method to synthesize water-soluble organic nanoparticles with ultralong luminescent phosphorescent for in *vivo* imaging [119]. Cell labeling, targeted in *vitro* and in *vivo* imaging, blood vessel imaging, cell tracking, inflammatory monitoring, and molecular imaging are all applications of organic NPS. [120-122]. Many commercial food products contain lipid nanoparticles, which are being studied for possible applications in other goods. [123]. The main benefit of utilizing lipid nanoparticles for these applications is that they can improve the bioavailability and/or functional performance of encapsulated components. [123]. There is minimal concern regarding the possible toxicity of this form of nanoparticle because it has been widely ingested by people for centuries. Other protein nanoparticle kinds for food applications have recently piqued people's curiosity. [124].

1.1.4.4 Hybrid Nanoparticles (NPs)

1.1.4.4.1 Definition of Hybrid Nanoparticles

Hybrid nanoparticles can be defined as well-organized nanomaterials consisting of two or more types of individual nanocomponents. The Nano compounds integrating hybrid nanoparticles can be bound via organic/inorganic molecular bridges or directly attached to one another. For example, a gold nanoparticle coated with a nanometric layer of silica

possesses the typical optical properties of gold nanoparticles and the chemical properties of silica as regards stability. This is a clear example of the combination of properties from the two nanoconstituents. Apart from the special type of bonding between the nanocompounds, the exceptional properties of hybrid nanoparticles are due to the highly organized arrangement of the nanoconstituents [125].

1.1.4.4.2 Classification of Hybrid Nanoparticles

Hybrid nanoparticles that contain both structural (therapeutic) and functional (diagnostic) nanocomponents. The functional nanocomponents such as gold nanostructures (for optical imaging), magnetic nanocrystals (for improving MRI contrast or hyperthermia). The structural components of the hybrid nanoparticles are mainly classified based on the therapeutic function they deliver. For example, structural nanocomponents such as a liposome, a micelle, mesoporous silica, a polymer, or a virus can mainly carry a drug cargo, while structural nanocomponents such as a gold nanoparticle or a carbon nanotube enable photoablation therapy [126].

1.1.5 Medical Applications of NPs

Medical applications of NPs are plentiful, owing to their ability to interact with external stimuli, including ultrasonic waves, infra-red radiation, and magnetic fields [127, 128]. As indicated by NPs' greater ability to identify liver metastases and metastatic lymph nodes, paramagnetic and super-paramagnetic NPs offer a lot of potential for cancer detection. [129, 130]. Metallic nanoparticles have the potential to be exploited as medicinal agents. Silver's antimicrobial properties are well known, and gold nanoparticles have been proven to cause cell damage when administered orally. Silver and gold nanoparticles are excellent

candidates for treating multidrug-resistant infections as well as cancer. [127, 131]. Furthermore, Au-NPs have been found to have anti-angiogenic properties, preventing collagen-induced arthritis in human umbilical vein endothelial cells. [132, 133]. In nanomedical research and development, the use of multifunctional NPs that incorporate diagnostic and therapeutic activities in the same system (theranostic) is gaining traction. Nano-theranostics systems, for example, could include enhanced diagnostics, hyperthermia treatment, and tailored administration of anticancer medications for cancer patients. Metal oxide NPs are an excellent example of "multitasking" platforms [127].

1.1.5.1-Treatment using NPs

Medical nanoparticles (MNPs) are employed in an experimental cancer treatment known as magnetic hyperthermia [134], which makes use of the heat generated by NPs when they are exposed to alternating magnetic fields. The attachment of MNPS to free-floating cancer cells, trapping and transporting them out of the body, is another potential cancer treatment [135]. MNPS can also be utilized for it, and these MNPS are kept inside by an externally produced magnetic field while the blood flows freely. Antibodies that target cancer cells or proteins are coated on MNPs [136].

1.1.5.2-Imaging using NPs

MNPs should be biocompatible, nontoxic, and stable. These characteristics can be altered by altering the size and coating properties of nanoparticles. [137, 138]. Metallic magnetic compounds (iron, nickel, and cobalt) are harmful due to oxidation and acid erosion. For these reasons, magnetic nanoparticles must be coated to protect them from deterioration. [139]. The opsonization process begins when nanoparticles are injected into the bloodstream. NPs are coated with plasma proteins and then

destroyed by phagocytic cells, preventing them from reaching the target cells [140, 141]. To prevent this, NPs are coated with organic layers like surfactants and polymers, as well as inorganic species like silica and carbon. MNPs' circulation time and colloidal stability may be improved by adding this additional layer [142, 143].

1.1.5.3-Extraction of Proteins from Biological Fluids

A protein is a macromolecule made up of a chain of amino acid residues that help the body fulfill critical processes. Proteins perform an unlimited number of jobs in the body, from DNA replication to catalyzing chemical processes to giving structural support [144, 145]. Proteins are frequently categorized according to their structure, which takes into account how many chains of amino acids make up their physical shape and pattern. For proper functioning, every component of the body, from individual cells to tissues and entire organs, requires a precise protein balance. As a result, proteins are incredibly important to studying biotechnology [146]. General structure of protein is shown in Figure 1.6.

Proteins are biological macromolecules that are required for the proper functioning of living organisms. Proteins consist of many amino acids bound by peptide bonds. The primary structure of a protein is made up of a sequence of amino acids at the most fundamental level. A protein molecule coils or folds into a secondary structure due to forces between these amino acids, hydrogen bonds, disulfide bridges, and electrostatic interaction between positive and negative charges. The α-helix and β-sheet are two examples of such structures [147, 148].

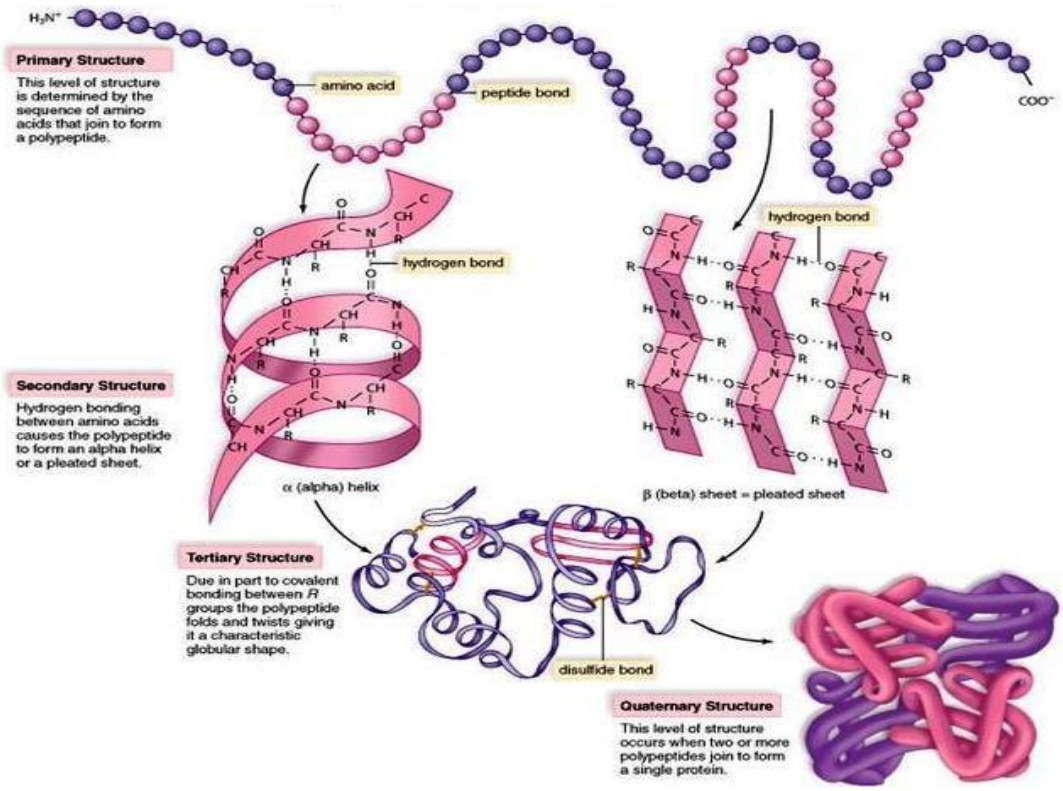

Figure 1.6 Protein Structures. [149].

The protein corona (PC), is a collection of proteins that are bound to the surface of NPs, is important for particle identification by the innate immune system. [150]. Even if isolation procedures were to become standardized, statistical assessments of proteins/nanoparticle interactions would always be required. Galmarini et al. (2018) proved the significance of replicates and statistics in the analysis of proteins adsorbed in vitro onto the surfaces of silica NPs [151].

1.2 Some Important Proteins to be extracted from the Human Serum

1.2.1 Luteinizing Hormone (LH)

Luteinizing hormone (LH) is a hormone that is produced and released in the body, with the anterior pituitary gland being the primary site of release. Because of its involvement in influencing the function of female ovaries and male testes (known as gonads), this hormone is classified as a gonadotrophic hormone. Hormones heavily control the human body's reproductive system, and luteinizing hormone (LH) is one of those hormones. This key hormone plays different roles in men's and women's bodies, but it's essential for a healthy reproductive system. [152].

1.2.1.1 Function of LH Hormone

In females: ovulation maintains corpus luteum, and secretion of progesterone, in males: testosterone secretion. In women, the hormone stimulates the ovaries to produce estradiol. A spike up in luteinizing hormone happens two weeks into a woman's cycle during ovulation, causing the ovaries to create an egg [153]. The luteinizing hormone activates the corpus luteum, causing it to generate progesterone to keep the pregnancy going if fertilization happens. Luteinizing hormone boosts testosterone production in the Leydig cells of men's testes [154]. Testosterone, in turn, promotes sperm production and enhances male traits such as a deep voice and facial hair growth.

1.2.1.2 Effects of LH Hormone

Since luteinizing hormone (LH) has a direct effect on the reproductive system, those with high amounts of the hormone may have infertility. Women's health, Too much luteinizing hormone is commonly linked to the polycystic ovarian syndrome, which results in unacceptably high testosterone levels. [155]. Hereditary illnesses can also induce high levels of hormones. These illnesses commonly prevent people from reproducing [156].

Low luteinizing hormone levels can also induce infertility because they inhibit sperm production and the ovulation process from taking place. In women, a shortage of luteinizing hormone hinders ovulation, whereas, in men, it prevents the release of gonadotrophin-releasing hormone (GnRH) [157].

1.2.1.3 Structure of LH Hormone

LH is a heterodimeric glycoprotein. Each monomeric unit is a glycoprotein molecule; the whole, functioning protein is made up of one alpha and one beta subunit. The structures of follicle-stimulating hormone (FSH), thyroid-stimulating hormone (TSH), and human chorionic gonadotropin are all identical (hCG). The protein dimer is made up of two glycopeptide subunits, designated alpha, and beta, that are not covalently linked [152]. Structure of LH hormone is shown in Figure 1.7.

Figure 1.7 Luteinizing Hormone (LH) [152].

1.2.1.4 Level of LH Hormone

LH levels are typically low during childhood and high following menopause in women. Because LH is secreted in pulses, it's important to track its concentration over time to gain an accurate picture of its blood level. Typical values during the reproductive years are 1–20 IU/L. Reference values for males over the age of 18 have been calculated to be 1.8–8.6 IU/L [153].

1.2.2 Follicle-Stimulating Hormone (FSH)

Follicle-stimulating hormone (FSH) is secreted by the gonadotropic cells of the anterior pituitary gland regulates the development, growth, pubertal maturation, and reproductive processes of the body. FSH and luteinizing hormone (LH) work together in the reproductive system ("Luteinizing and Follicle Stimulating Hormones") [158].

1.2.2.1 Function of FSH Hormone

FSH regulates the development, growth, pubertal maturation, and reproductive processes of the human body. In females, FSH initiates follicular growth, specifically affecting granulosa cells. With the concomitant rise in inhibin B, FSH levels decline in the late follicular phase. FSH helps control the menstrual cycle and stimulates the growth of eggs in the ovaries. FSH levels in women change throughout the menstrual cycle, with the highest levels happening just before the ovary releases an egg. This is known as ovulation [159]. In males, FSH causes Sertoli cells to secrete androgen-binding proteins (ABPs), which are controlled by the anterior pituitary's negative feedback mechanism, inhibin. FSH-stimulated Sertoli cell activation maintains spermatogenesis and induces inhibin B production [160].

1.2.2.2 Effects of FSH Hormone

In females, FSH increases the development and recruitment of immature ovarian follicles in the ovary. FSH is a critical survival factor in early (small) follicles, preventing apoptosis in these small follicles (programmed death of the somatic cells of the follicle and oocyte). During the luteal-follicle phase transition period, blood levels of progesterone and estrogen (mostly estradiol) fall and no longer prevent the release of FSH;

as a result, FSH peaks around day three (day one is the first day of menstrual flow) [153].

In males, FSH causes primary spermatocytes to undergo the first stage of meiosis, resulting in secondary spermatocytes. FSH stimulates the creation of androgen-binding protein in the Sertoli cells of the testes by binding to FSH receptors on their basolateral membranes, and spermatogenesis must begin [153].

1.2.2.3 Structure of FSH Hormone

FSH is a 35.5 kDa glycoprotein heterodimer made up of alpha and beta polypeptide units. It has a similar structure to luteinizing hormone (LH) and thyroid-stimulating hormone (TSH). The alpha subunits of the glycoproteins LH, FSH, and TSH are all 96 amino acids long, however, the beta subunits are different. The presence of both subunits is required for biological activity. FSH has a 111-amino-acid beta subunit (FSH) that interacts with the follicle-stimulating hormone receptor and gives the hormone its particular physiological activity. The sugar portion of the hormone, which is covalently bonded to asparagine, is made up of mannose, N-acetylgalactosamine, galactose, and sialic acid [153]. Structure of FSH hormone is shown in Figure 1.8.

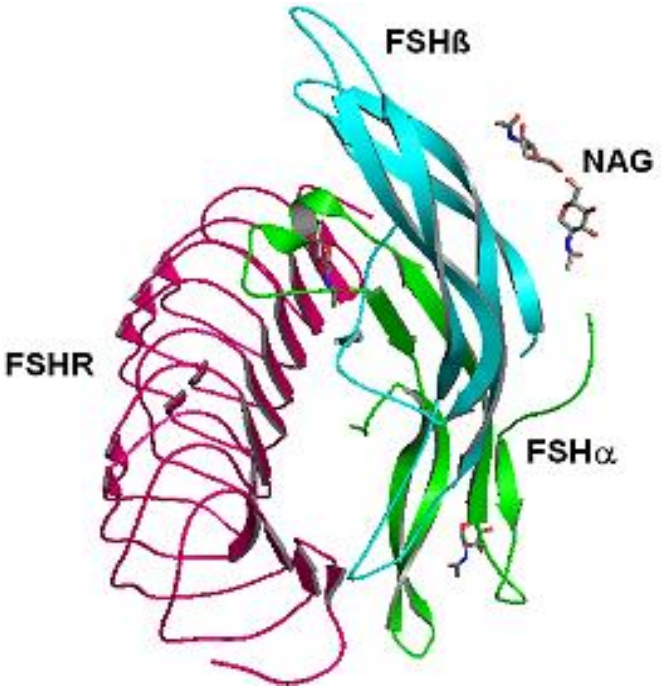

Figure 1.8 Follicle-Stimulating Hormone (FSH) [153].

1.2.2.4 Level of FSH Hormone

FSH levels that are too high the most common cause of a high serum FSH concentration is a woman who is going through or has recently gone through menopause. High FSH levels indicate that the gonad's typical limiting feedback is missing, resulting in unrestrained pituitary FSH production. FSH may play a role in osteoporosis and cardiovascular disease in postmenopausal women [161]

Low FSH levels and decreased FSH output can cause gonadal dysfunction (hypogonadism). The failure to produce normal amounts of sperm is the most common symptom of this illness in males. The termination of reproductive cycles in females is a regular occurrence [162].

1.3 Adsorption of Proteins

Adsorption is the adhesion of atoms, ions, biomolecules, or molecules of the gas, liquid, or dissolved solids to a surface [163]The adsorbate (the molecules or atoms being gathered) forms a film on the surface of the adsorbent during this process. It varies from absorption, which occurs when a liquid or solid permeates or dissolves a fluid [164]. Both processes are referred to as sorption, while desorption is the opposite of adsorption.

In nature, the adsorption of soluble proteins at solid-liquid interfaces is essential. Proteins have an important part in blood coagulation, for example. Adsorption of proteins is crucial in a variety of industrial and biological processes [165]. Blood proteins, for example, tend to adsorb onto the surfaces of foreign objects. This is the initial stage in the process of preventing surface-induced thrombosis [166].

The physiological behavior and fate of the NPs are dictated by the corona components that change the original properties of the particles. Protein coronas confer a "biological identity" on the NPs [167], making cell membranes sense. The adsorbed molecular composition poses a difficulty for practical medical applications of NPs since it affects nanotherapeutic biodistribution and efficacy [168].

When corona proteins interact with NPs surfaces, they can elicit reversible or persistent peptide rearrangements. These changes are influenced by both physicochemical surface qualities and the surrounding environment [169]. Although minor modifications such as the loss of β-sheets or α-helixes can be repaired after detachment from the NPs, larger modifications, such as the loss of β-sheets or α-helixes, cannot be restored and affect protein function. Surface chemistry, size, shape, protein

sequence, conformation, and hydrophobicity of NPs are all regulated by a range of parameters, as previously indicated. Only a few of the techniques used to discover structural alterations in adsorbed proteins include Dynamic Light Scattering (DLS), Electron Microscopy, Electrophoresis, Fourier Transform Infrared Spectroscopy (FTIR), Mass Spectroscopy (MS), and Nuclear Magnetic Resonance (NMR) [170].

The ratio between NPs and protein size is an important factor in determining the number of adsorbed proteins and alterations in their structure. If the NPs are significantly larger than a single protein, it is reasonable to assume that numerous peptides can be carried on its surface. Furthermore, globular proteins may expand and attach to a quasi-flat surface if the NPs surface has a low curvature. On the other hand, smaller NPs of the same substance make less interaction with protein domains and are less likely to cause structural change [169]. According to the authors, [171] a multilayered interaction occurs, with a cationic protein binding the anionic gold surface at one location and another anionic protein binding the anionic gold surface at the other. For several nanomaterials, the size of NPs has been shown to impact the composition of a protein corona (NMs) [172]. Although determining if corona proteins have undergone structural changes is not always straightforward, non-specific aggregation of multiple biomolecules sometimes results in unanticipated folding and loss of tertiary structures. It has been demonstrated that the adsorption of specific proteins on 100 nm NPs causes more protein alteration than particles smaller than 5 nm of the same substance [173].

Along with the importance of NPs size, the importance of NPs shape and surface morphology in protein corona formation should not be overlooked. The surface chemical moieties and charge of NPs, as

expected, have a significant impact on protein adsorption and interactions with cell membrane components [173, 174]. Changes in the complexity and abundance of corona biomolecules can also be connected to differences in free energy in protein folding and unfolding produced by distinct surface groups of the same size [175]. As indicated by the loss of α-helixes in adsorbed albumin, changing the NP polymeric composition and polymer size induces structural changes in adsorbed proteins (Rashad et al. 2021) [176]. Neutral-shelled NPs typically bind fewer proteins than negatively or positively charged NPs [8].

1.3.1 Adsorption isotherms

Adsorption is usually described through isotherms, that is, the amount of adsorbate on the adsorbent as a function of its pressure (if gas) or concentration (if liquid) at a constant temperature. To allow the comparison of different materials, the quantity adsorbed is almost typically standardized by the mass of the adsorbent. The ideal Langmuir model equation, which is given by, was found to be well verified by the adsorption isotherms produced for proteins [177].

$$q = \frac{q_s bC}{1 + bC} \quad \text{……..(1.1)}$$

Where: C is the concentration of adsorbate at equilibrium, q is the quantity of adsorbate at equilibrium (x/m) (where x=weight of adsorbent per m weight of adsorbent), b is a constant representing the maximum constant representing the intensity of adsorption. The transformed form of the Langmuir equation is given by Equation 1.2 [178], which will be used to calculate the Langmuir parameter constants by fitting adsorption isotherm data obtained for protein.

$$\frac{q}{C} = \frac{1}{q_s b} + \frac{1}{q_s} C \quad \text{.....(1.2)}$$

The kinetic mechanism is used to derive the Langmuir isotherm. The following hypotheses underpin it:

1. The surface of the adsorbent is uniform; hence all the adsorption sites are uniform.
2. Adsorbed molecules do not interact with each other.
3. All adsorption occurs through the same mechanism.
4. Only a monolayer of adsorbed molecules is formed. They do not deposit on other adsorbed molecules [179].

Freundlich isotherm: This isotherm is normally used to describe the adsorption of a wide variety of antibiotics, steroids, and hormones and is given by equation (3):

$$q_e = K_f C_e^{1/n} \quad \text{.....(1.3)}$$

Where: k and n are empirical constants for each adsorbent-adsorbate pair at a given temperature. The applicability of the Freundlich equation can be studied through the linear form of the equation:

$$\log q_e = \log K_f + \left(\frac{1}{n}\right) \log C_e \quad \text{.....(1.4)}$$

Freundlich equation applicability indicated heterogeneity of the surface.

1.3.2 Forces Involved in the Adsorption Process

The four fundamental classes of forces and interaction in protein adsorption are:

1) Ionic or electrostatic interaction [180].

2) Hydrogen bonding [181].

3) Hydrophobic interaction (largely entropically drive) [182].

4) Interactions of charge-transfer [183].

I.4 ELISA Technique

Enzyme-linked immunosorbent assay (ELISA), also known as an enzyme immunoassay (EIA), is a biochemical technique used as an analytical tool in biomedical research to detect and quantify specific antigens or antibodies in a given sample. ELISA is a novel technique to detect and measure biological molecules in very small quantities ng/ml to pg/ml, paving the way for analyzing and detecting countless other biological molecules, including hormones, peptides, and proteins [184]. The basic immunology principle of an antigen-binding to its specific antibody is used in ELISA / EIA, which permits the detection of very amounts of antigens in a fluid sample, such as proteins, peptides, hormones, or antibodies. To detect biological substances, ELISA and EIA use protein-labeled antigens and antibodies, with FSH and LH being the most widely used proteins.

ELISA has been used as a diagnostic tool in medicine and plant pathology and as a quality-control check in various industries [185]. In simple terms, in ELISA, an unknown amount of antigen is affixed to a surface of the microwells plate (Figure 1.9), and then a specific antibody is then applied over the surface to bind to the antigen. This antibody is

linked to a protein, and in the final step, a substance is added that the protein can convert to some detectable signal, most commonly a color change in a chemical substrate.

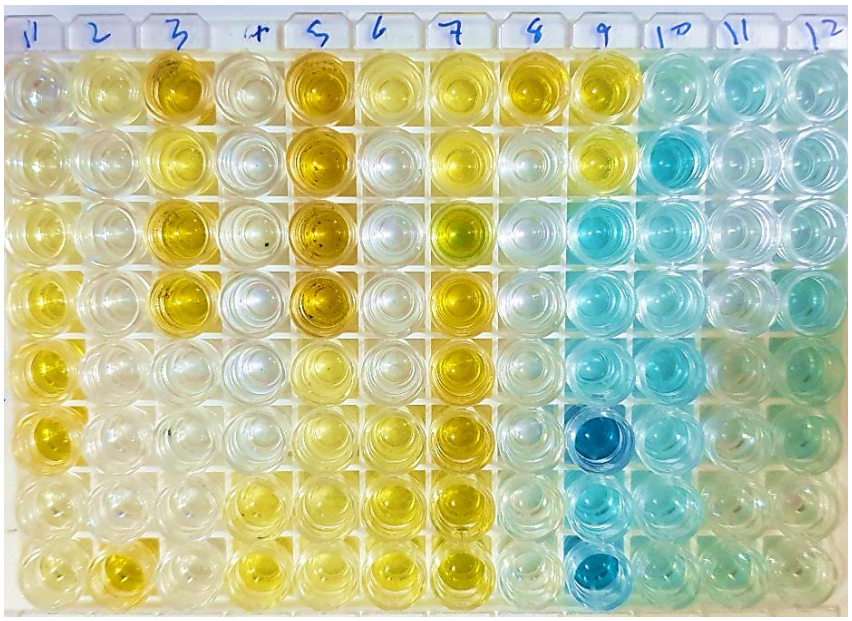

Figure 1.9 A 96-Well Microtiter Plate being used for ELISA.

At least one antibody that is specific to a certain antigen is required for an ELISA. A sample containing an unknown amount of antigen is immobilized either non-specifically (by adsorption to the surface) or specifically (by adsorption to the surface) on a solid substrate (usually 96-well microtiter plates) (via capturing by another antibody specific to the same antigen, in a "sandwich" ELISA). The detecting antibody is added after the antigen has been immobilized, generating a combination with the antigen. The detection antibody can be covalently attached to a protein or can be detected by a secondary antibody that has been bioconjugated to a protein.

The protein works as a signal, producing many signal molecules even if only a few protein-linked antibodies remain bound. The plate is usually cleaned with a mild detergent solution between each step to eliminate any non-specifically bound proteins or antibodies. The plate is developed after the final wash phase by adding an enzymatic substrate, which produces a visual signal that reflects the amount of antigen in the sample. A color change is produced when proteins (such as LH, and FSH) react with suitable substrates (such as 3,3',5,5'-Tetramethylbenzidine (TMB), which is employed as a signal. The signal, on the other hand, must be linked to the presence of an antibody or antigen, which is why the protein must be linked to a suitable antibody [186, 187]

ELISAs can be performed with several modifications to the basic procedure as shown in Figure1.10.

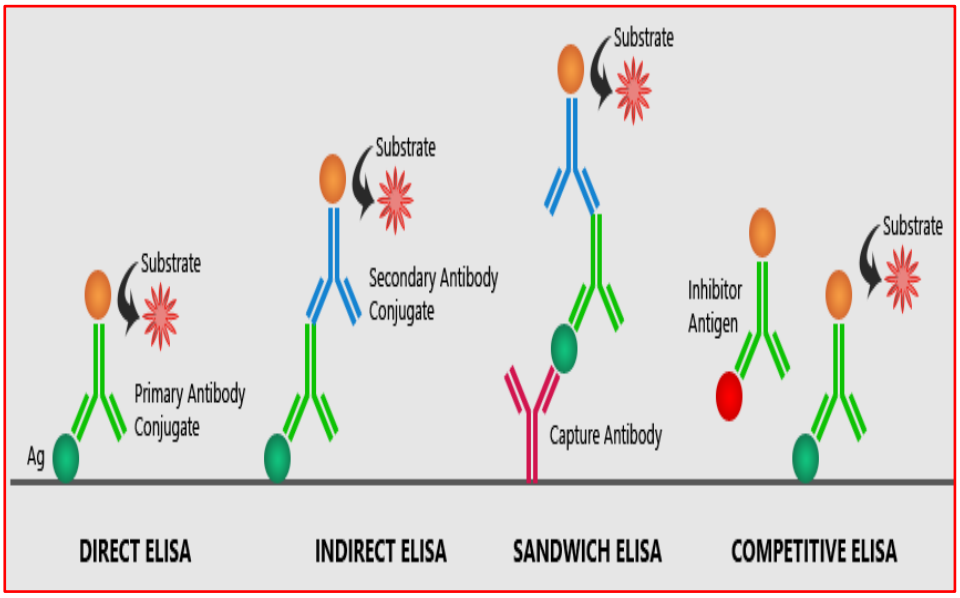

Figure 1.10 Common ELISA Formats [188].

The main step, immobilization of the antigen of interest, can be achieved either directly on the assay plate or indirectly via a capture antibody linked to the plate. The antigen is then detected either directly

(with a tagged primary antibody) or indirectly (with a secondary antibody) (labeled secondary antibody). The sandwich test is the most potent ELISA assay format. Because the analytic to be evaluated is bound between two primary antibodies: the capture antibody and the detection antibody, this form of capture assay is referred to as a "sandwich" test. Sandwiches are employed because they are delicate and durable [189]. Figure 1.10 depicts the ELISA technique in general.

Various ELISAs have been used, with the basic procedures are shown in Figure 1.11 being modified. The direct or indirect detection of antigen by adhering or immobilizing the antigen or antigen-specific capture antibody directly onto the wall surface is the most important step in the ELISA experiment [190].

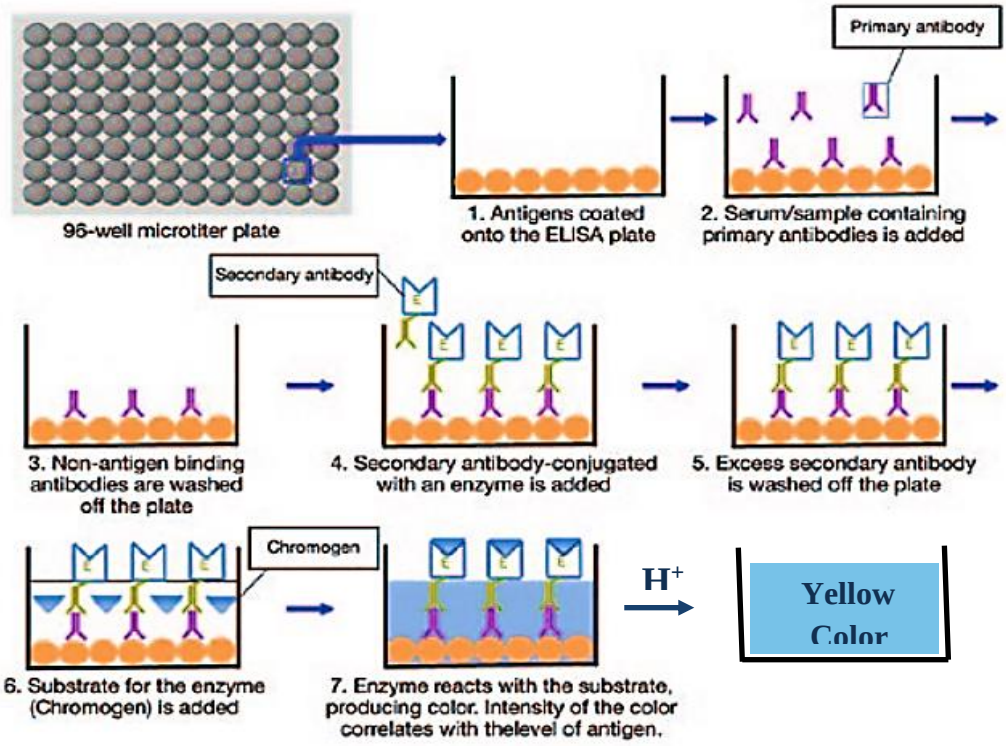

Figure 1.11 An Enzyme-Linked Immunosorbent Test (ELISA) is a Technique for Detecting an Antigen in a Sample [191].

The antigen can be carefully chosen out of a sample of mixed antigens using a "capture" antibody for sensitive and reliable readings. As a result, the antigen is "sandwiched" between detection and capture antibodies. Assume the antigen in question is small and has only one epitope for antibody binding. In this case, a competitive method is used, in which the antigen is labeled and competes for the binding antigen and antigen in the sample, or the antibody is labeled and competes for the binding antigen and antigen in the sample. Each of these ELISA tweaks can be used for both qualitative and quantitative purpose[189, 190].

1.5 Polycystic Ovary syndrome (PCOS)

Polycystic ovary syndrome (PCOS) is a condition that affects 5–20 % of women of reproductive age around the world. Hyperandrogenism, ovulatory dysfunction, and polycystic ovarian morphology (PCOM) are all symptoms of PCOS, with high androgen production by the ovaries being a significant component. The majority of those affected have metabolic dysfunction, which is characterized by insulin resistance and compensatory hyperinsulinemia. PCOS increases the risk of type 2 diabetes, gestational diabetes, and other pregnancy difficulties, as well as venous thromboembolism, cerebrovascular and cardiovascular events, and endometrial cancer.

PCOS is an exclusionary diagnosis characterized by hyperandrogenism and ovulatory dysfunction. Treatment may include metabolic abnormalities, androgen suppression and endometrial protection, reproductive therapy, and the detection and treatment of psychological features, as well as lifestyle changes, medication, and possibly surgery for the prevention and management of excess weight, androgen suppression and/or blockade, endometrial protection, reproductive therapy, and the detection and treatment of psychological features [192].

1.5.1 Definition of disease

The conjunction of hyperandrogenism with chronic anovulation in women without particular underlying disorders of the adrenal or pituitary glands is the most widely accepted clinical description of polycystic ovary syndrome [193]. Hyperandrogenism is defined clinically by hirsutism, acne, and androgen-dependent alopecia, as well as biochemically by high serum levels of androgens, especially testosterone and androstenedione. Obesity is widespread, but it is not universal [194]. These characteristics are usually associated with luteinizing hormone and androgen hypersecretion, but normal or low follicle-stimulating hormone serum concentrations [195, 196]. The recent application of modern, high-resolution diagnostic ultrasonography has moved the scales in favor of morphology-based diagnosis once again [197, 198] (Figure 1.12 A and Figure 1.12B). Nonetheless, the outcomes of studies in which diagnoses were made based on ultrasonographic criteria and those in which polycystic ovarian syndrome was defined based on clinical and biochemical criteria show a surprising degree of agreement [199, 200].

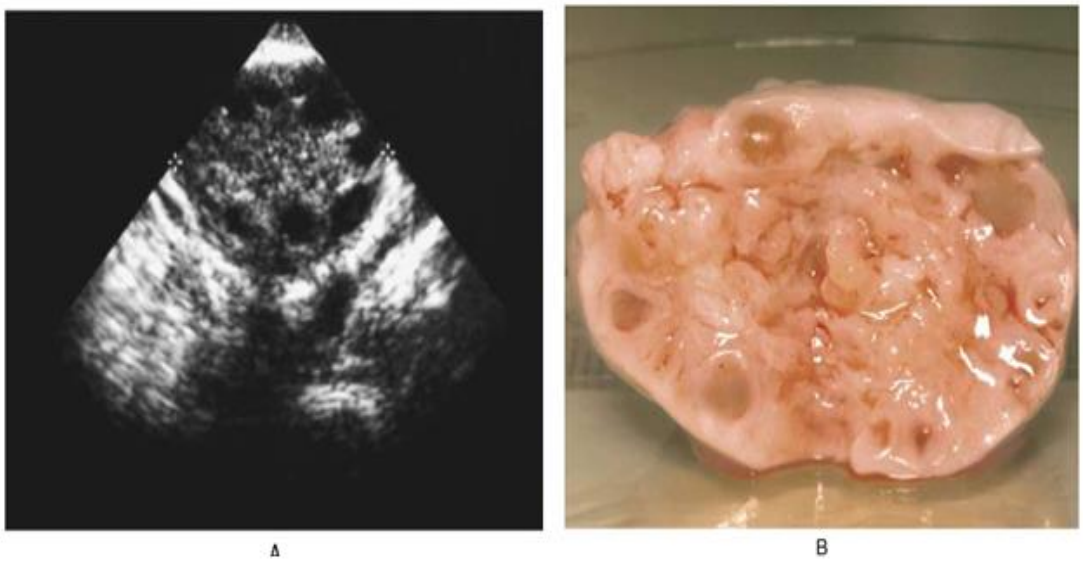

Figure 1.12 Ultrasonographic (Panel A) and Gross Histologic (Panel B) Appearance of a Typical Polycystic Ovary [201].

1.5.2 Symptoms of Polycystic Ovary syndrome

Symptoms of the polycystic ovarian syndrome in women who have polycystic ovaries but no other PCOS traits are considered asymptomatic, and they do not report a longer time to conceive [202]. They do, however, show susceptibility to the development of ovarian hyperstimulation syndrome (OHSS) as follows:

1-Menstrual disturbance

The majority of women with PCOS have an irregular menstrual cycle, with infrequent menstruation and anovulation being the most common pattern [203].

2-Obesity

Obesity appears to exacerbate anovulation in PCOS by interacting with the hypothalamic-pituitary-ovarian axis, leading to high LH levels that impede follicular maturation [204]. Weight gain can cause oligo- or amenorrhea, while weight loss can bring ovulation and regular cycles back [205]. In most big studies, however, 35–50% of women with PCOS are overweight (BMI>25 kg/m^2) or obese (BMI>27 kg/m^2), according to the findings [206].

3-Hirsutism

Hirsutism in women describes terminal hair growth in an adult male distribution. Common presentations are excess facial hair, hair on the chest between the breasts, and hair on the lower abdomen [207].

4-**Acne**

Acne is a skin condition that affects the hair follicle and is linked to the sebaceous and apocrine glands. It can be found in up to one-third of PCOS women [203, 208]. Unlike androgenic alopecia and hirsutism, the main issue for women with acne is increased secretion production, with serum androgen levels rarely rising [209, 210].

1.5.3 Diagnosis

The diagnosis of polycystic ovary syndrome is usually made based on a combination of clinical, ultrasonographic, and biochemical criteria. If a woman has oligomenorrhoea with one or more of the following three symptoms, she is likely to have polycystic ovary syndrome: Ultrasonography reveals polycystic ovaries, hirsutism, and hyperandrogenemia [211].

Although normal luteinizing hormone serum concentrations do not rule out the diagnosis, many women with the syndrome show hypersecretion of the hormone. The diagnosis of polycystic ovary syndrome in a woman with hirsutism and regular cycles is more difficult, but the presence of polycystic ovaries on ultrasonography in conjunction with moderate hyperandrogenemia (i.e., serum testosterone concentrations of 85 to 150 ng per deciliter [3 to 5 nmol per liter]) points to a benign, ovarian cause of the hirsutism [212].

1.5.4 Epidemiology

Epidemiology according to 1990 national institutes of health (NIH) criteria [213, 214], PCOS affects 6–10% of women worldwide, making it one of the most frequent human illnesses and the single most common endocrinopathy in women of reproductive age. PCOS is more likely to

occur in women who have clinical hyperandrogenism (such as hirsutism, acne, or alopecia), menstrual disruption, PCOS, and hyperinsulinemia from adiposity-dependent insulin resistance, or a family history of PCOS [215].

1.5.5 Treatment of PCOS

Currently no universal treatment for PCOS is available, and therefore, treatment must always be individualized and adapted to the actual needs of the individual patient [216]. There are currently no drugs approved for the indication of PCOS [217]. But Glucophage was used as a treatment for the purpose of increasing the reaction of insulin in the body.

1.6 Aims of the Study

This thesis will first examine the following points

1- Separation of important proteins from the serum of patients with diseases that are well-known to have an increase in the levels of these proteins such as LH and FSH hormone.

2- Synthesis and identifiqation some Nanoparticles compounds.

3- Study the ability of the synthezed compounds to interact with the LH and FSH hormones as a means to extract or immobilize the hormones on the surface of these compounds. All hormones concentration would measure using the ELISA technique at a nanogram per milliliter scale.

4- Estimation the surface activity and homogeneity via the adsorption isotherms of the protein-surface interaction and desorption process.

Chapter 2
Materials and Methods

2.1 Chemicals

Table 2.1 lists the chemical components utilized in this study, along with their purity and suppliers.

Table 2.1 Chemicals Used in This Study, along with Their Purity and Suppliers.

No.	Chemicals	Chemical formula	Company Supplied	Purity %
1	Sodium Selenite	Na_2SeO_3	Sigma-Aldrich/ Germany	99%
2	Chitosan (CS)	$C_6H_{11}NO_4$	British Drug House/ British	98%
3	Glucose	$C_6H_{12}O_6$	Sigma-Aldrich/ Germany	99%
4	Graphite powder	Graphite (C)	Sigma-Aldrich/ Germany	99%
5	Ammonium hepta molybdate	$(NH_4)_6Mo_7O_{24}.4H_2O$	Sigma-Aldrich/ Germany	99%
6	Boric Acid	H_3BO_3 or $B(OH)_3$	Sigma-Aldrich / United *States*	99%
7	Urea	NH_2CONH_2	Sigma-Aldrich/ Germany	99%
8	Manganese(II) chloride Tetrahydrate	$MnCl_2.4H_2O$	CHEM-SUPPLY/ Australia	99%
9	Isopropanol	C_3H_8O	British Drug House/ British	98%
10	Potassium permanganate	$KMnO_4$	Sigma-Aldrich / United *States*	99%
11	Hydrochloric acid	HCl	British Drug House/British	99%
12	Sodium hydroxide	NaOH	British Drug House/ British	99%
13	Sulphuric acid	H_2SO_4	British Drug House/ British	99%
14	Ethanol	C_2H_5OH	British Drug House/ British	98%
15	FSH Test System ELISA Kit	Test System	Monobind/ USA	100%

16	LH Test System ELISA Kit	Test System	Monobind/ USA	100%
17	Prolactin ELISA Kit	Test System	Monobind/ USA	100%
18	Serum Calcium	Reagent	SPACTRUM	100%
19	Albumin	Reagent	SPINREACT	100%
20	Magnesium	Reagent	SPACTRUM	100%

2.2. Instruments.

Table 2.2 lists the instruments used in this study, along with their models and companies.

Table 2.2 The Instruments Utilized in This Study, as well as Their Models and Manufacturers.

No.	Instrument	Model	Company, Source	Location
1	X–rays Diffraction (XRD)	Lab X XRD 6000 SHIMADZU	JAPAN	Baghdad University Ibn Al-Haytham
2	Scanning Electron Microscope (SEM)	HITACHI S-3000 N	JAPAN	kufa University Department of Chemistry
3	Energy Dispersive X-rays Spectroscopy (EDX)	HITACHI S-3000 N	JAPAN	kufa University Department of Chemistry
4	Fourier Transform Infrared (FTIR)	FTIR 8400S Shimadzu	JAPAN	Babylon University Department of Chemistry
5	Dynamic Light Scattering (DLS)	Brook haven V. 2.5	GERMANY	Ministry of Sciences and Technology
6	Zeta Potential Analysis (ZPA)	Zeta plus, Brook haven	GERMANY	Ministry of Sciences and Technology
7	Furnace (300-1200) ˚C	Muffle Furnace, Gallenkamp	GERMANY	Babylon University Department of Chemistry
8	PH-Meter	WTW-Inolab PH	GERMANY	Babylon University Department of Chemistry

9	**Sensitive Balance**	**Sartorius HR-200**	**GERMANY**	**Babylon University Department of Chemistry**
10	**Centrifuge**	**Cyan, CL008**	**MALAYSIA**	**Babylon University Department of Chemistry**
11	**Thermo-Stirred Heater**	**Heidolph MR Hei standard, IKA-RH**	**BRITISH**	**Babylon University Department of Chemistry**
12	**Magnetic-Stirred Hot Plate**	**Gallenkamp, England**	**GERMANY**	**kufa University Department of Chemistry**
13	**Oven**	**Memmert**	**USA**	**Babylon University - Department of Chemistry**
14	**Elisa**	**Modal 6+/ metertech**	**USA**	**kufa University - Department of Chemistry**
15	**UV/VIS 721 Spectrometer Double Beam**	**PG Instruments Ltd**	**UNITED KINGDOM**	**Kufa University Department of Chemistry**
16	**Vortex**	**Cyan, CL001**	**MALAYSIA**	**kufa University - Department of Chemistry**
17	**Micropipettes 5-50µl, 10-100 µl**	**HW LAB**	**GERMANY**	**kufa University - Department of Chemistry**

2.3 Preparation of the Nanocomposite

2.3.1 Synthesis of Selenium Oxide (SeO_2-NPs)

This study used a modified co-precipitation approach to synthesize SeO_2 nanoparticles. Fifty milliliters of distilled water were added to 0.08 gm of sodium selenite (Sigma-Aldrich-USA) in flask A and then spun until complete dissolution at room temperature for 30 minutes. In flask B, 0.20 g gelatin (Sigma-Aldrich -United States) was added to 50 ml distilled water until complete dissolution, whereas 0.2 g glucose (Sigma-Aldrich-USA) was added to 25 ml H_2O in flask C. At room temperature, the combination of both containers (B & C) was swirled until they were dissolved completely.

After that, the solution from flask B was gradually added to flask A, and the combination was stirred at 80 °C for another 60 minutes. The flask C solution was added dropwise to the flask A solution as a reductant. The rate at which the reductant was added is important for completely reducing selenium ions to selenium NPs and limiting the final nanoparticle size range. The mixture was spun for 24 hours after fully incorporating flask C into flask A before being transferred to the oven heated at 80 °C until complete solvent evaporation. The precipitate was then calcinated for 2 hours at 600 °C to remove gelatin species and generate selenium oxide powder [218].

2.3.2 Synthesis of Molybdenum Oxide (MoO_2-NPs)

Synthesis of (MoO_2-NPs) was conducted as follows: in 40 mL ultrapure water, 0.6184 g boric acid, 12.2122 g urea, and 5.0 g $(NH_4)6Mo_7O_{24}4H_2O$ were dissolved and heated at 55 °C until the water was boiled away and a white solid was obtained. The white solid was then moved to a tube

furnace and heated to 700 °C for two hours under an N_2 environment at a heating rate of 5 °C min^{-1} before being allowed to cool to ambient temperature. The result was a dark brown substance known simply as "MoO_2-NPs" [219].

2.3.3 Synthesis of Manganese Oxide (MnO_2-NPs)

All of the chemical reagents were analytical grade, and they were utilized exactly as they were given. $MnCl_2.4H_2O$ (0.18 g) was mixed with isopropanol (50 ml) in a round-bottomed flask with refluxing equipment in a typical method for generating MnO_2. With vigorous stirring, the solution was heated to around 83 ^{0}C, and then $KMnO_4$ (0.10 g) dissolved in 5ml deionized (DI) water was swiftly added to the boiling solution, resulting in a substantial amount of black precipitate. After 10 minutes, the mixture was brought to room temperature. The precipitate was centrifuged and rinsed in DI water before being air-dried at 60 °C overnight [220].

2.3.4 Synthesis of Graphene Oxide (GO)

A modified Hummers method was used to synthesis graphene oxide [221]. Graphite powder (3.0 g) was first stirred into concentrated H_2SO_4 (24 ml), which had already been pre-dissolved at 80 ^{0}C with $K_2S_2O_4$ (2.5 g) and P_2O_5 (2.5 g). In an oil bath, the mixture was agitated for 4.5 hours at 80 °C. The solution was diluted with distilled water and allowed to settle overnight after cooling to room temperature. Filtration was used to collect the as-prepared product, which was subsequently washed with distilled water and dried for ten hours at 80 °C. The pre-oxidized graphite (2.5 g) and $NaNO_3$ (1.25 g) were then combined and placed in a flask with an ice bath to dissolve in concentrated H_2SO_4 (115 ml). To keep the temperature below 20 ^{0}C, $KMnO_4$ (7.5 g) was progressively added to the mixture with

vigorous stirring. The mixture was agitated at 35 ^{0}C for 0.5 hours after the ice bath was removed, followed by the addition of H_2O. (300 ml). After 1 hour of stirring at 98 °C, the color of the solution turned yellow. The solution was then diluted further with distilled water before adding H_2O_2 (30%, 30 ml). The residual product was centrifuged and rinsed with distilled water until the pH was neutralized after being rested overnight. The brown flake graphene oxide (GO) is next dried in a vacuum.

2.3.5 Synthesis of CS/GO-NPs Composite

To synthesis a graphene oxide solution, 0.5 g graphene oxide and 0.1 g chitosan (CS) were distributed in 500 ml deionized water. After that, 0.5 g nanoparticles were added to the graphene oxide solution, which was then agitated for two hours at room temperature. The resulting precipitate was centrifuged and carefully washed with deionized water to eliminate contaminants before being dried overnight at 80 ^{0}C to give CS/GO-NPs composite [222].

2.4 Techniques of Characterization

2.4.1 X-rays Diffraction (XRD)

Using a (Shimadzu-XR-6000) device with a copper target, voltage (40 KV), and current, the produced materials were analyzed by X-rays diffraction (30 mA). Scanning was done constantly on the range (2θ = 10.000-80.000) at a speed of 5 degrees per minute and a receiving slit (0.3 mm). Scherrer's formula was used to calculate the mean crystallite size (D) using XRD data in the following equation [223, 224].

$$\mathcal{D} = \frac{k\lambda}{\beta \cos\theta} \qquad \text{…….. (2.2)}$$

D: is the mean crystallite size (in nm).

k: the Scherrer constant (0.94), which varies depending on the crystal structure.

λ: is the wavelength of X-rays radiation (0.15406 nm for CuKα).

β: is the Full width half maximum (FWHM) then multiplied by (π/180) to convert to radians

Θ: is diffraction (Bragg's angle).

2.4.2 Scanning Electron Microscopy (SEM)

A scanning electron microscope (SEM) scans a material with a focused beam of electrons to obtain pictures. When electrons collide with atoms in a sample, a variety of signals are produced that can be detected and contain information about the sample's surface topography and composition. The electron beam is scanned in a raster scan pattern in most circumstances, and the position of the beam is combined with the acquired signal to generate an image. At a 1nm scale, SEM can reach a greater resolution. At high and low vacuums, as well as in wet environments, specimens can be observed (environmental SEM). The emission of secondary electrons from atoms energized by the electron beam is the most common way of detection.

The number of secondary electrons is determined by the angle between the surface and the beam. On a flat surface, the sample's plume of secondary electrons is mostly confined; but, on a tilted surface, the plume is partially exposed, and extra electrons are emitted. Scanning the sample and detecting secondary electrons produces an image revealing the tilt of the surface.

The protocol for identifying NPs by SEM is described below; One milligram of the prepared nanocomposites powder and sputtered with gold before analysis for better conductivity and resolution of the sample. Put the sample in the SEM S 50 then the image was taken.

2.4.3 Energy Dispersive X-rays Spectroscopy (EDX).

This technique is used to determine the elements present in pure nanocomposites CS/GO-M_xO_2-NPs and to give information about the composition ratio of elements for nanomaterials. As a result, moving electrons beam through the atoms of the sample and image of each element. This technique correlates with the scanning electron microscope.

2.4.4 Fourier Transform Infrared Spectrophotometer (FTIR).

The preferred method of infrared spectroscopy is Fourier transform infrared (FTIR). In IR spectroscopy, IR radiation is passed through a substance, with part of it absorbing or transmitting. The resulting spectrum is a molecular fingerprint of the material, representing molecule absorption and transmission. IR spectroscopy is useful for a variety of analyses since no two unique molecular structures create the same IR spectra, similar to a fingerprint. Molecular vibrations and rotations are used in IR spectrometry. The dipole moment of a molecule changes as a result of these actions. The radiation from an infrared source collides with the mirror, and the resulting beam is sent through the cell. The radiation is then focused on the detector, which records the amount of energy that passes through the sample at each frequency, yielding a spectrum that maps intensity versus frequency [225, 226]. The protocol of FTIR

measurements is as follows: two hundred milligrams of dry KBr were ground with 2 mg of nanocomposites, then 40-50 mg of the mixture was taken to make KBr pellets/disks. KBr used as background for analysis spectrophotometer in the range (400-4000) cm^{-1}. Before starting the scanning process by FTIR.

2.4.5 Dynamic Light Scattering (DLS)

DLS is one of the methods for determining particle sizes. Its experimental theory is founded on two assumptions in particular. The particles are first assumed to be moving in Brownian motion. The second hypothesis is that the particles seen in the experiment are spherical and have a lower diameter than the molecular dimensions. When light strikes a moving particle, it undergoes a Doppler shift, changing the wavelength of the incoming light. This variation is proportional to the particle's size. The spherical size distribution, which measures the particle's diffusion coefficient, can be calculated and used to represent the particle's mobility in the medium. Because light scattering can provide information about the position of the particles, the formulas above the radius of the particles are simple to calculate.

A zeta sizer is used to make DLS determinations [227]. The particle size distribution of the nanocomposites powders was determined by DLS techniques using (Model: 90 Plus Particle Sizer, Brookhaven Instruments) at the ministry of sciences and technology. The measurements were carried out at a wavelength of 657 nm at 25 °C. Samples were prepared by dispersing small amounts of powder in 100 % water / H_2SO_4 followed by sonication for 10 min.

2.4.6 Zeta Potential Analysis (ZPA)

The potential difference between the dispersion medium and the stationary layer of fluid adhering to the dispersed particle is theoretically defined as zeta potential analysis. The zeta potential is a fundamental indication of colloidal dispersion stability. The zeta potential's magnitude shows the degree of electrostatic repulsion in the dispersion between neighboring and similarly charged particles. A high zeta potential confers stability to molecules and particles of sufficient size, preventing aggregation in the solution or dispersion. At tiny potentials, attractive forces may outweigh repulsion, causing the dispersion to break and flocculate. Colloids with a high zeta potential (positive or negative) are electrically stable, whereas colloids with a low zeta potential coagulate or flocculate [228]. The zeta potentials of the nanocomposites powders was determined by zeta potentials analysis techniques using (Model: 90 zeta Plus Instruments) at the ministry of sciences and technology. The measurements were carried out at a wavelength of 657 nm at 25 °C.

The following Helmholtz-Smoluchowski equation was used to convert the electrophoretic mobility to zeta potential $\zeta = E\,(4\pi\eta / \varepsilon)$, where: ζ = zeta potential (mV), E = electrophoretic mobility, η = viscosity of the dispersion medium, ε = dielectric constant of the solvent [229].

2.4.7 ELISA Reader

The intensity of colored solutions in Microwells was measured at a set wavelength using an ELISA reader (Metertech / USA model 6+). (450 nm).

2.5 Polycystic Ovary Syndrome (PCOS)

2.5.1 Patients

A total of 150 patients and control groups, 120 (PCOS) women patients took part in the research and the control group of 30 women. Their age range was 20 ± 45 years for both patients and controls. The samples were collected from the "Diabetes and Endocrinology Center" in Marjan Hospital, Al-Imam Al-Sadiq Hospital, and Babylon Hospital for Women and Children in Babylon Governorate-Iraq during the period from 9 May 2021 until 30 August 2021.

PCOS is a set of symptoms caused by a hormonal imbalance that affects women and girls of reproductive age. At least two of the three conditions listed below are common in women with PCOS [230].

1. Ovulation failure causes irregular menstrual periods or no periods at all.
2. Excessive body or facial hair, which is an indication of elevated androgen levels (a type of hormone).
3. Cysts (fluid-filled sacs) on one or both ovaries "polycystic" indicates "many cysts."
4. PCOS is the most prevalent cause of ovulatory infertility, which refers to infertility caused by a lack of ovulation, the monthly release of a mature egg from the ovary.

Exclusion Criteria: The study excluded patients with any significant obvious systemic disease, including heart disease, smoking, or other endocrine disorders.

2.5.2 Controls

A control group of thirty healthy women was chosen. Their ages ranged from 20 to 45, which was similar to that of the patients. None of the women in this study were infertile, had irregular periods, or had any other endocrine issues.

2.5.3 Blood Samples

In this study, a disposable needle and plastic syringes were used to collect five milliliters (5 ml) of venous blood from each patient and control at room temperature (25 ℃).. The serum was separated and transported into new disposable plain tubes after being centrifuged at 3000 rpm for 5 minutes.

2.6 Measurements

2.6.1 Luteinizing Hormone (LH)

2.6.1.1 Principle

For an immune-enzymometric assay, high affinity and specificity antibodies (enzyme and immobilized) with variable and different epitope recognition, as well as native antigens, are required reagents. The interaction between streptavidin-coated wells and exogenously given biotinylated monoclonal anti-LH antibody causes immobilization at the surface of a microplate well during the experiment. The natural antigen and antibodies react without competition or steric hindrance to form a soluble sandwich complex when the monoclonal biotinylated antibody, enzyme-labeled antibody, and a serum containing the native antigen are combined. The interaction is depicted in the following equation:

$$^{Enz}Ab_{(p)} + Ag_{LH} + {}^{Btn}Ab_{(m)} \underset{K\text{-}a}{\overset{Ka}{\rightleftharpoons}} {}^{Enz}Ab_{(p)}\text{-}\ Ag_{LH}\ \text{-}\ {}^{Btn}Ab_{(m)}$$

Where:

$^{Btn}Ab_{(m)}$ = Biotinylated Monoclonal Antibody (Excess Quantity)

Ag_{LH} = Native Antigen (Variable Quantity)

$^{Enz}Ab_{(p)}$ = Enzyme labeled Antibody (Excess Quantity)

$^{Enz}Ab_{(p)}$-Ag_{LH}-$^{Btn}Ab_{(m)}$=Antigen-Antibodies Sandwich Complex

Ka = Rate Constant of Association

K-a = Rate Constant of Dissociation

During the high-affinity interaction of streptavidin and biotinylated antibody, the complex is simultaneously deposited in the well. This interaction is illustrated below:

$$^{Enz}Ab_{(p)}\text{-}Ag_{LH}\text{-}{}^{Btn}Ab_{(m)} + Streptavidin_{cw} \Rightarrow \text{immobilized complex}$$

Where:

$Streptavidin_{cw}$ = Streptavidin immobilized on well

Immobilized complex=Antibodies-Antigen sandwich bound

After equilibrium is attained, the antibody-bound fraction is separated from the unbound antigen by decantation or aspiration. The enzyme activity in the antibody-bound fraction is directly proportional to the native antigen concentration.

2.6.1.2. Reagents of the kit:

1. LH standards: Six vials of standards for LH antigen at levels of 0, 5, 25, 50, 100, and 200 mIU/ml.
2. LH Enzyme Reagent: containing enzyme-labeled affinity purified antibody, dye, and preservative.

3. Streptavidin Coated Plate (96 wells): One 96-well microplate coated with streptavidin.
4. Wash Solution Concentrate: containing a surfactant in buffered saline. A preservative has been added.
5. Substrate A: containing tetramethylbenzidine (TMB) in a buffer.
6. Substrate B: containing hydrogen peroxide (H_2O_2) in a buffer.
7. Stop Solution (1N HCl).

2.6.1.3. Procedure

1. Pipettes were used to pipette 50 microliters of the appropriate serum reference, control, or specimen into the designated well.
2. To each well, 100 microliters of LH-enzyme reagent were applied.
3. The microplate was gently stirred for 20-30 seconds before being incubated at room temperature for 60 minutes.
4. The contents of the microplate were discarded by decantation, and the plate was dried and blotted with absorbent paper.
5. A total of 350 microliters of diluted wash buffer was applied and then decanted (tap and blot). This process was performed three times.
6. To each well, 100 microliters of working substrate solution (A+B) were added.
7. The wells were incubated for 15 minutes at room temperature.
8. To each well, 50 microliters of stop solution was added and carefully stirred for 15-20 seconds.
9. An ELISA reader was used to measure the absorbance in each well at 450 nm.

2.6.1.4. Calculation of Results

On linear graph paper, the absorbance of each standard was plotted against the corresponding LH content in ng/ml (Fig.2.1). Through the plotted points, the best-fit curve was drawn. The concentration was calculated using the graph's horizontal axis and the intersection point on the curve.

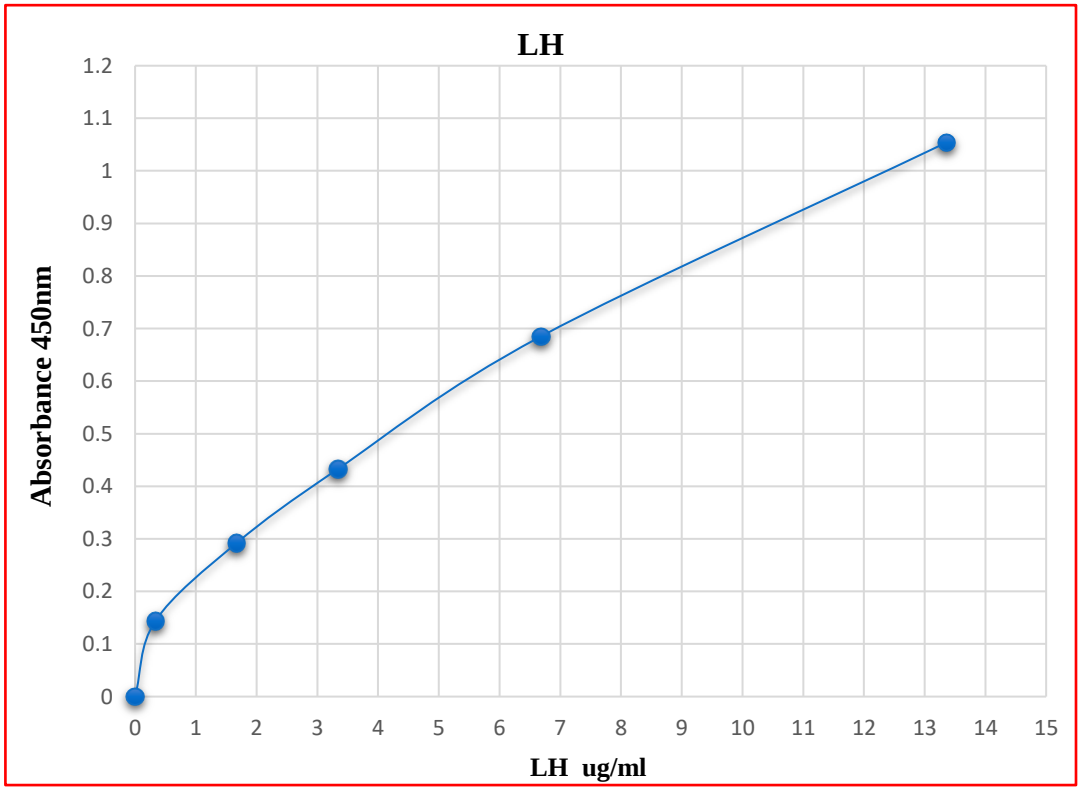

Figure 2.1 Calibration Curve of LH.

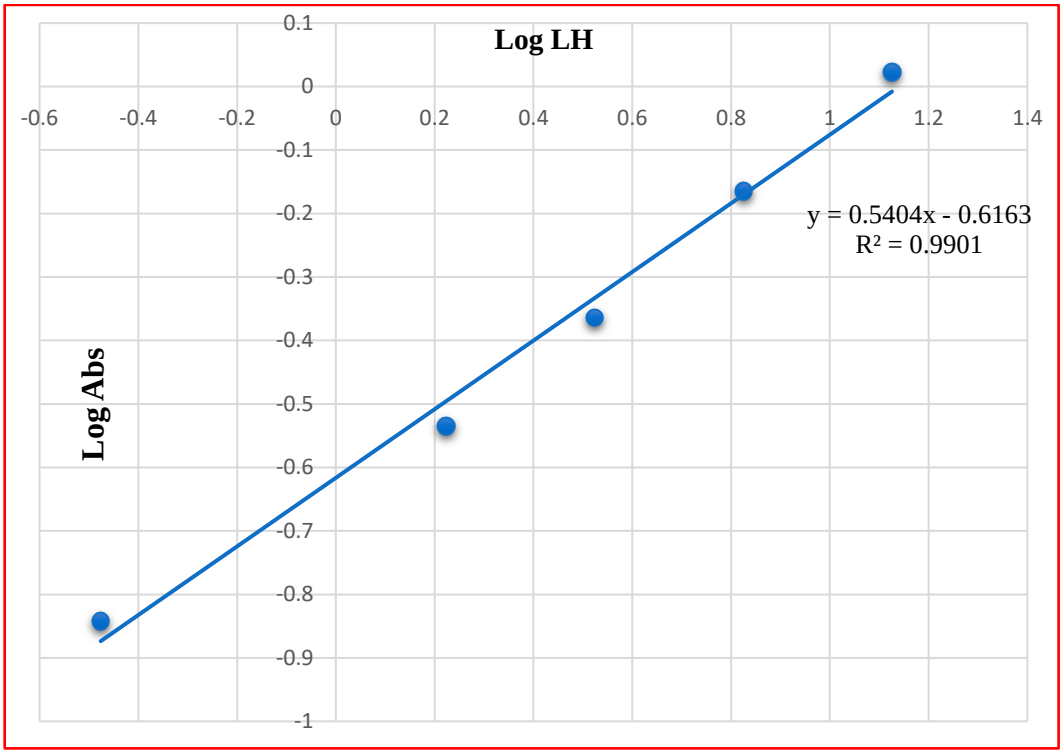

Figure 2.2 Calibration Curve of Log LH / Log Abs LH.

2.6.2 Follicle Stimulating Hormone (FSH)

2.6.2.1 Principles

An immune-enzymometric assay requires high affinity and specificity antibodies (enzyme and immobilized), as well as natural antigen. Because of the interaction between streptavidin-coated wells and exogenously injected biotinylated monoclonal anti-FSH antibody, the immobilization procedure occurred at the surface of a microplate well during the experiment. The native antigen forms a soluble sandwich complex with monoclonal biotinylated antibodies, enzyme-labeled antibodies, and a serum containing the native antigen without competition or steric hindrance. The interaction can be seen in the equation below:

$$^{Enz}Ab_{(p)} + Ag_{FSH} + {}^{Btn}Ab_{(m)} \underset{K\text{-}a}{\overset{Ka}{\rightleftharpoons}} {}^{Enz}Ab_{(p)}\text{-}Ag_{FSH}\text{-}{}^{Btn}Ab_{(m)}$$

Where:

$^{Btn}Ab_{(m)}$ = Biotinylated Monoclonal Antibody (Excess Quantity)

Ag_{FSH} = Native Antigen (Variable Quantity)

$^{Enz}Ab_{(p)}$ = Enzyme labeled Antibody (Excess Quantity)

$^{Enz}Ab_{(p)}$- Ag_{FSH} - $^{Btn}Ab_{(m)}$ = Antigen-Antibodies Sandwich Complex

Ka = Rate Constant of Association

K-a = Rate Constant of Dissociation

A high-affinity interaction between streptavidin and biotinylated Antibody deposits the complex in the well at the same time. This interaction is illustrated below:

$$^{Enz}Ab_{(p)}\text{- } Ag_{FSH} \text{ - } {}^{Btn}Ab_{(m)} + Streptavidin_{cw} \Rightarrow \text{Immobilized complex}$$

Where:

$Streptavidin_{cw}$=Streptavidin immobilized on well

Immobilized complex= Antibodies-Antigen sandwich bound

Sandwich complex bound to the solid surface.

The antibody-bound fraction is separated from the unbound antigen by decantation or aspiration once equilibrium has been achieved. The native antigen concentration is directly proportional to the enzyme activity in the antibody-bound fraction. The complex is simultaneously deposited in the well due to a high-affinity interaction between streptavidin and biotinylated Antibody.

2.6.2.2 Reagents of the kit:

1. FSH standards: Six vials of standards for FSH antigen at levels of 0, 5, 10, 25, 50, and 100 mIU/ml.

2. FSH Enzyme Reagent: containing enzyme-labeled affinity purified antibody, dye, and preservative.

3. Streptavidin Coated Plate (96 wells): One 96-well microplate coated with streptavidin.

4. Wash Solution Concentrate: containing a surfactant in buffered saline.

5. Substrate A: containing tetramethylbenzidine (TMB) in a buffer.

6. Substrate B: containing hydrogen peroxide (H_2O_2) in a buffer.

7. Stop Solution (1N HCl).

2.6.2.3 Procedure:

1. Fifty microliters of the appropriate serum reference, control, or specimen were pipettes into the assigned well.
2. To each well, 100 microliters of FSH-enzyme reagent were added.
3. After swirling the microplate for 20-30 seconds, it was incubated at room temperature for 60 minutes.
4. After decanting the contents of the microplate, it was dried and blotted with absorbent paper.
5. Three hundred and fifty microliters of diluted wash buffer were added and then decanted (tap and blot). This step was repeated for three washes.
6. All wells were filled with 100 microliters of working substrate solution (A+B).
7. The wells were incubated for 15 minutes at room temperature.
8. Each well was filled with 50 microliters of stop solution and gently stirred for 15-20 seconds.
9. An ELISA reader read the absorbance in each well at 450 nm.

2.6.2.4 Calculation of Results

On linear graph paper, the absorbance of each standard was plotted against the corresponding FSH concentration in g/ml (Figure 2.3). Through the plotted points, the best-fit curve was drawn. The concentration was calculated using the graph's horizontal axis and the intersection point on the curve.

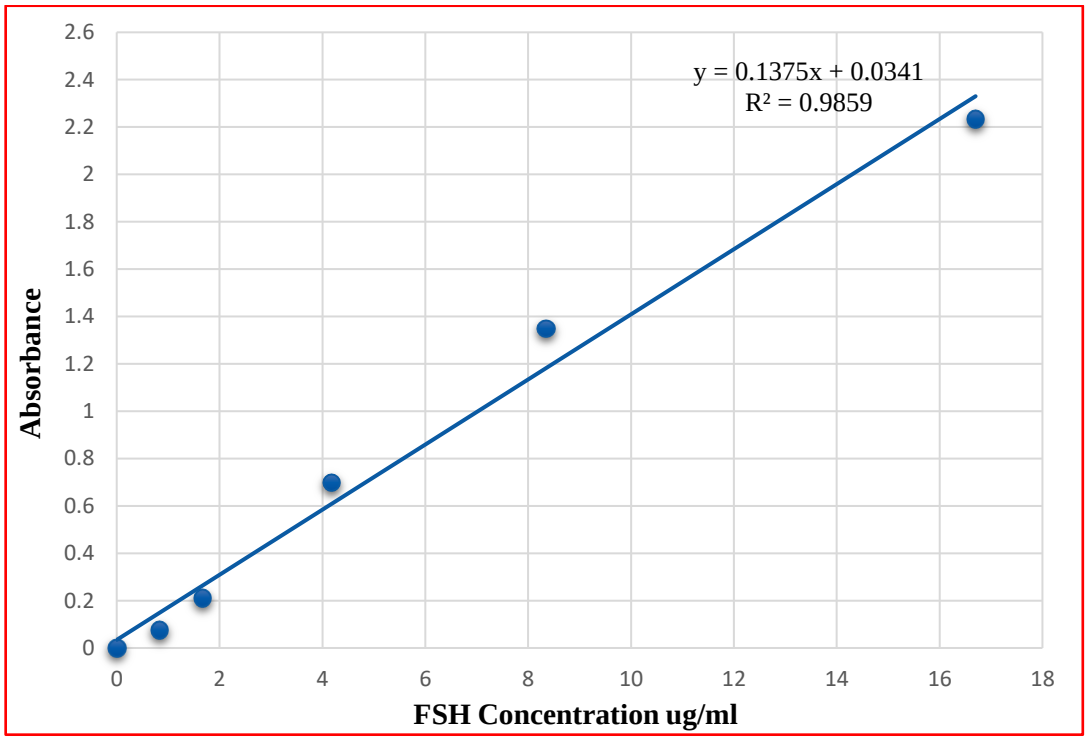

Figure 2.3 Calibration Curve of FSH.

2.6.3 Serum Calcium

2.6.3.1 Principle

At neutral pH, calcium reacts with Arsenazo III [1,8-Dihydroxy-3,6-disulpho-2,7-naphthalene-bis (azo)-di benzene arsonic acid] to form a blue complex whose intensity is proportional to calcium content.

2.6.3.2 Reagents

Arsenazo III	Imidazol Buffer pH 6.75…….100 mmol/l Arsenazo III……..0.120 mmol/l
Standard	Calcium aqueous…….. 10 mg/dl

2.6.3.3 Procedure

1. The spectrophotometer was adjusted to 0 at 620 nm with distilled water.
2. The following quantities were pipetted into a cuvette:

	Blank	Standard	sample
Standard	---	10 µl.	---
Sample	---	---	10 µl.
Reagent	1,0 ml	1,0 ml	1,0 ml

After mixing, the mixture was incubated at 15-25°C for 5 minutes. The standard and sample absorbance's (Abs) were compared to a blank. For at least 1 hour, the color is stable.

2.6.3.4 Calculations

S. Calcium (mg/dl)= (Abs. Sample/Abs. Standard) x 10 (standard conc.)

2.6.4 Albumin

2.6.4.1 Principle

At pH 4.0, serum albumin binds to the color bromocresol green preferentially. At 630 nm, the rise in absorbance of the resultant albumin-dye combination is proportional to the albumin content.

2.6.4.2 Reagents

Reagent 1	Bromocresol green, pH 4.0…….0.12 mmol/l
Standard	Albumin aqueous…….....50g/l

2.6.4.3 Procedure

1. The spectrophotometer was adjusted to 0 at 630 nm with distilled water.
2. The following quantities were pipetted into a cuvette:

	Blank	Standard	Sample
Standard	---	5 µl	---
Sample	---	---	5 µl
Reagent	1.0 ml	1.0 ml	1.0 ml

Incubate for 10 minutes at room temperature after thoroughly mixing. The sample's and standard's absorbance (Abs) were measured against a blank. For 1 hour, the color remains steady.

2.6.4.4 Calculations

Albumin (g/dl) = (Abs Sample / Abs Stand.) x (Standard Conc.)

2.6.5 Magnesium

2.6.5.1 Principle:

When Magnesium is treated with Calmagite in an alkaline solution, it creates a purple-colored complex. The reaction is particular when EGTA is present. The purple hue intensity is proportional to Mg content.

2.6.5.2 Reagent composition:

R1 (Chromogen)	Calmagite……..0.30 mmol/l EGTA……0.21 mmol/l
R2 (Buffer)	Amino-methyl propanol……1mmol/l
Standard	Magnesium aqueous sol……..2 mg/dl

2.6.5.3 Preparation:

Working reagent (WR): 1 volume of Calmagite solution (R1) was mixed with 1 volume of buffer solution (R2).

2.6.5.4 Procedure:

1. The spectrophotometer was adjusted to zero at 520 nm with distilled water.

2. The following quantities were pipetted into a cuvette:

	Blank	Standard	Sample
Standard	---	10 µl	---
Sample	---	---	10 µl
WR	1.00 ml	1.00 ml	1.00 ml

After a 5-minute incubation period at room temperature, the solutions were combined and read. The sample's and standard's absorbance (Abs) were measured against a blank. For at least 45 minutes, the color remains steady.

2.6.5.5 Calculations

S.Mg (mg/dl) = (Abs. Sample / Abs. Standard) x 2 (stand. conc.)

2.6.6 Total Protein

2.6.6.1 Principle

Protein generated a violet-blue color complex with a basic copper-sulfate solution containing tartrate (Biurett Reagent). The total protein concentration in the sample determines the intensity of the colored solution that forms.

2.6.6.2 Reagent composition:

BIURET solution	Potassium-Sodium-Tartrate…….15 mmol/l Sodium Hydroxide……..100 mmol/l Potassium Iodide……. 5 mmol/l Copper (II) Sulphate……... 19 mmol/l
Standard	Bovine albumin……..... 70 g/l

2.6.6.3 Procedure

1. The spectrophotometer was adjusted to zero at 546 nm with distilled water.

2. Pipette the following amounts into a cuvette: The mixes were combined and incubated at 15-25 °C for 10 minutes. The standard and sample absorbance (Abs) were compared to a blank. The color will last at least 1 hour.

	Blank	Standard	Sample
Standard	---	25 µl	---
Sample	---	---	25 µl
R.1 Biuret	1000 µl	1000µl	1000µl

2.6.6.4 Calculations

Total protein (g/dl) = (Abs. Sample / Abs. Stand.) x stand. Conc.

2.7 Statistical Analysis

The distribution types of the variable's results were examined using the Kolmogorov-Smirnov test. According to the statistical distribution, the variables were split into two types: normally distributed variables and nonparametric variables.

The t-test was used to compare the patients and control groups, as well as subdivided groups, in the measured parameters for normally distributed variables. To estimate the correlation between parameters, correlation coefficients (r) were determined.

The results have been expressed as medians in addition to (mean standard deviation) for nonparametric variables that are not normally distributed. The Spearman's correlation coefficient (rho) test was used to compare the measured parameters between the patients and control groups, as well as between subdivided groups.

2.8 Estimation of Equilibrium Time of Adsorption

The time required for full saturation (equilibrium time) of the surface of organometallic compounds (adsorbent) by FSH, and LH protein (adsorbate) has been determined by the following procedure:

100 µL of an initially fixed concentration (100 ng/ml) of hormones solution was shaken with 20 mg of each NPs compound in an Eppindroff® tube. Five tubes for each compound were prepared. The tubes were incubated with shaking. The hormone FSH, and LH concentration in the solution was measured in the tubes every 30 minutes using the ELISA technique as mentioned previously. Before measurement, the tubes were centrifuged at 4000 rpm for 20 minutes to precipitate the NPs compounds, and hormone level was estimated in the aspirated supernatant. The concentrations were plotted against time until the concentration of proteins in the solution was constant (No further uptake of adsorbate by adsorbent as the time proceeds).

2.9 Adsorption Isotherms for Proteins on NPs

One hundred microliters of proteins solution at concentrations 0, 5, 10, 25, 50, and 100 ng/ml were added to 20 mg of each nanocomposite in an Eppindroff® tube. The tubes were shaken for an hour, which was longer than the equilibrium time calculated in the previous paragraph. The solution's hormone concentration was measured using the ELISA technique, as mentioned previously. Before measurement, the tubes were centrifuged at 4000 rpm for 5 minutes to precipitate the nanocomposite, and the hormone level was estimated in the aspirated supernatant.

The amount of hormone adsorbed was calculated from the initial and final concentrations and the volume of the solution. This yields the equation:

$$Qe = \frac{x}{m} = \frac{V(Co-Ce)}{m} \quad \text{.....(2-1)}$$

X: The quantity adsorbed (ng)

V: Volume of solution (ml)

Co: Initial concentration (ng/ml)

Ce: Equilibrium concentration (ng/ml)

m: Weight of adsorbent (Organometallic compound)

Qe values were plotted versus the equilibrium concentrations (Ce).

The resulting diagrams are the adsorption isotherms required to understand and interpret the systems under investigation.

2.10 Desorption process for Proteins on NPs

The intensity of the hormone-nanocomposite interaction was investigated by desorption experiments. Each hormone was adsorbed from solution onto the nanocomposite using an adsorption-like technique, with one initial hormone concentration (100 µl) for each nanocomposite. To avoid hormone denaturation, the supernatant was withdrawn and replaced with 100 µl of normal saline solution (0.9 percent NaCl) after incubation and centrifugation as indicated above. After that, each sample was incubated at room temperature to allow desorption to take place. The tubes were centrifuged for 5 minutes at 4000 rpm to precipitate the nanocomposite, and the hormone level was estimated in the aspirated supernatant before measurement. The desorption percentages were

computed using the ratio of hormone quantity released into the solution to hormone quantity adsorbed on the nanocomposite originally, i.e., the weight of hormone in 100 µl/weight of hormone in 20 mg:

$$\%\text{Desorbed} = \frac{Ce/10}{Qe/20} * 100\% \text{.....(2-2)}$$

2.11 Interaction of Hormone FSH and LH with CS/GO-NPs

To study the interaction of hormones with CS/GO-NPs, 100 µl of FSH and LH hormones solution into different concentrations (0,5, 10, 15, 20, 25, 30, 35, and 40 mIU/ml was added of CS/GO-NPs in the Eppendorf tubes. According to WHO standards, the units of hormone concentrations were converted to ng/ml. [231]. The tubes were shaken for an hour, longer than the equilibrium duration that was determined in prior research. The mixture was then centrifuged for 20 minutes at 4000 rpm. The hormone content in the aspirated supernatant was determined using Monobind / USA Enzyme-Linked Immunosorbent Assay (ELISA) Kits. The following equation was used to compute the amount of hormone adsorbed on the surfaces $Qe=X/M=[V(C_o-C_e)]/m$.

Where:

X: the quantity adsorbed (ng)

V: volume of solution (ml)

C_o: initial concentration (ng/ml)

C_e: equilibrium concentration (ng/ml)

m: weight of adsorbent.

The adsorption isotherms needed to understand and interpret the systems in question were plotted against the equilibrium concentrations (Ce), and the resulting graphs show the Qe versus Ce values. Log Qe = LogKf + 1/nLogCe is the linear form of the Freundlich isotherm. It has been proven to be the most appropriate adsorption isotherm equation for hormone adsorption on CS/GO-NPs. Kf is a function of adsorption energy and temperature. It is a marker of the adsorbent's absorptive capacity and evaluates the interaction process. **n** is an empirical constant proportional to the adsorption driving force's magnitude (intensity of adsorption) [232]. The adsorption process was repeated using human serum as a source of FSH and LH.

Chapter 3
Results and Discussion

3.1 Characterization of the Synthesized Nanoparticles SeO_2-NPs and CS/GO- SeO_2-Nps

The characterization of the synthesized SeO_2-NPs and CS/GO-SeO_2-Nps was studied using different analytical instruments such as X-ray diffraction (XRD), Scanning electron microscopy (SEM), Energy dispersive X-rays spectroscopy (EDX), Fourier transform technique (FT-IR), UV-Visible spectroscopy, Dynamic Light Scattering (DLS), and Zeta potential analysis (ZPA).

3.1.1 X-rays Diffraction (XRD) of SeO_2-NPs and CS/GO-SeO_2-Nps.

X-rays diffraction examinations of as-synthesized SeO_2-NPs and CS/GO-SeO_2-Nps revealed the crystalline structure, as shown in Figure 3.1.

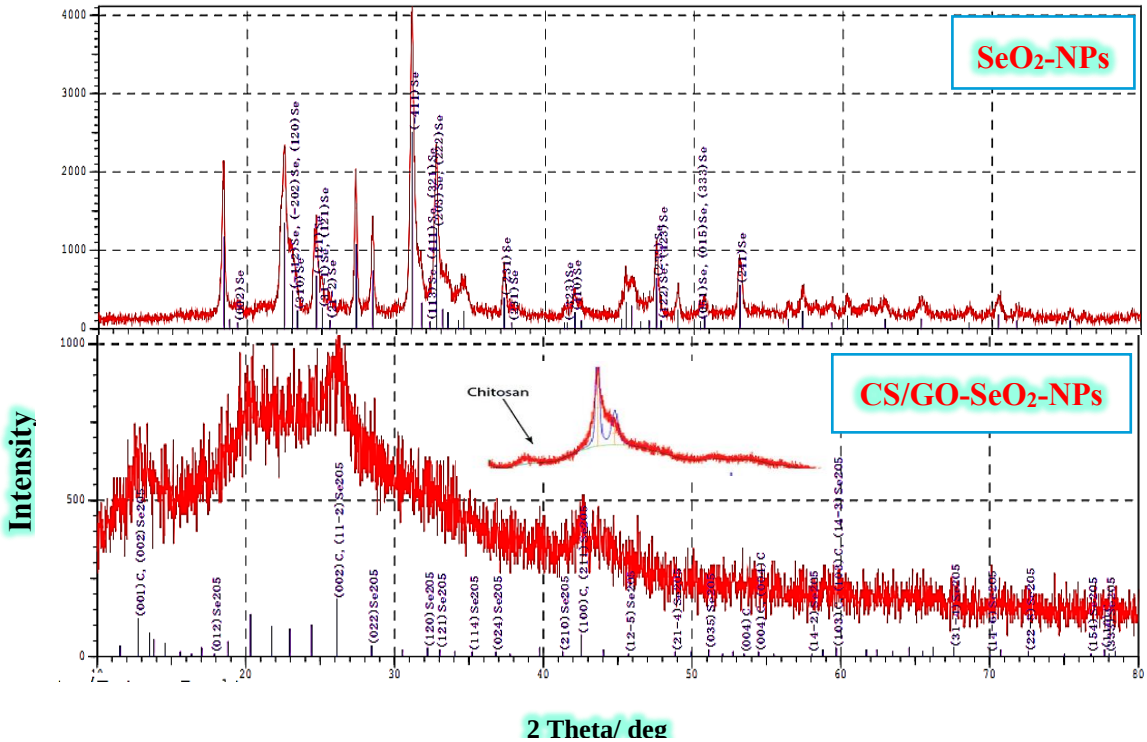

Figure 3.1 XRD Patterns of SeO_2-NPs and CS/GO-SeO_2-NPs.

The X-rays diffraction patterns of Cs/GO-SeO_2-NPs is shown in Figure 3.1. There are three prominent peaks of SeO_2-NPs at $2\theta = 24.1°$, 37.7°, 53.4°, and 64.9°, which confirms a high level of crystalline structure. Chitosan (Cs) show one slightly broad peak at $2\theta = 20.2°$. After graphene oxide (GO) crosslinking, the initial peaks remained although with lower intensity. New peaks at 18° and 24° appeared, indicating that the crystal lattice was being affected by ionic interactions. XRD peaks depend on crystal size, but the distinctive peaks of SeO_2-NPs may overlap, perhaps because of the well-dispersion of selenium into the nanocomposite matrix [233, 234].

According to the literature, the triple-helical crystalline structure of gelatin is responsible for these distinctive peaks [235]. In addition, the characteristic diffracted peaks at 2θ = 24.1, 26.2, 31.0, 37.7, 42.4, 47.4, 53.4, 60.2, 68.4, 70.4, and 75.2 correspond to the (100), (101), (102), (112), (120), (201), (013), (202), (210), and (231) reflections in Figure 3.1, which are in good agreement with the standard JCPDS data (JCPDS Card No. 06-0362) for the phase of pure selenium oxide crystals [236]. The average crystalline size of SeO_2-NPs was obtained using The Debye–Scherrer formula (Eq.1) [218]. According to the Scherrer formula:

$$D = k \lambda / \beta \cos\theta \quad \ldots\ldots\ldots (3.1)$$

Which, is D is the crystallite size in nm, λ marks the X-rays wavelength of radiations, β is the width at half maximum (FWHM), and θ is the diffraction angle, with $k = 0.94^o$ as the Scherrer's formula constant. The average size of CS/GO-SeO_2-NPs was 15.3 nm as a result of this, which agrees with SEM analyses.

3.1.2 Scanning Electron Microscopy (SEM) of SeO_2-NPs and CS/GO-SeO_2-Nps.

The morphology and size of the synthesized SeO_2-NPs and CS/GO-SeO_2-Nps were investigated by the field-emission scanning electron microscopy (SEM) image are shown in Figure 3.2.

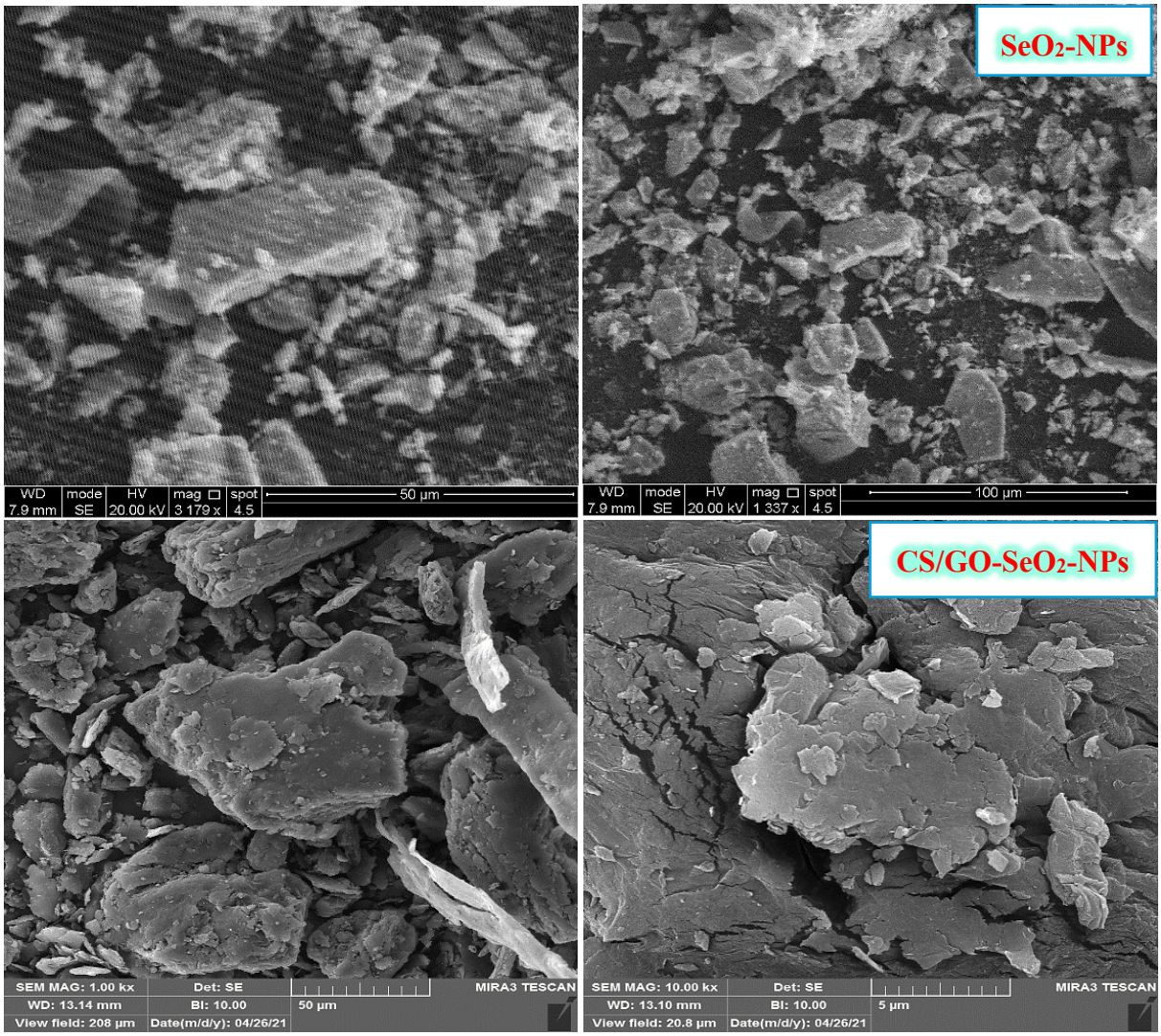

Figure 3.2. SEM Images of SeO_2-NPs, and CS/GO-SeO_2-NPS.

SEM images of chemically synthesized SeO_2 nanoparticles revealed that it is uniformly distributed and that the NPs were nanoscale in size. Also indicates that the surface morphology of chitosan is smoother and less porous than that of CS/GO-SeO_2 nanocomposites. The SeO_2-NPs show an irregular agglomerated grain-like morphology, while the

CS/GO-SeO_2-Nps exhibited densely rough and crunchy morphology compared with CS. Based on the literature, results herein show that CS/GO-SeO_2-Nps nanocomposites are a rough surface rich in porous particles [237].

3.1.3 Energy Dispersive X-rays Spectroscopy (EDX) of SeO_2-NPs and CS/GO-SeO_2-Nps.

EDX analysis of SeO_2-NPs and CS/GO-SeO_2-NPs proves that the obtained nanoparticles are pure in nature as shown in Figure 3.3.

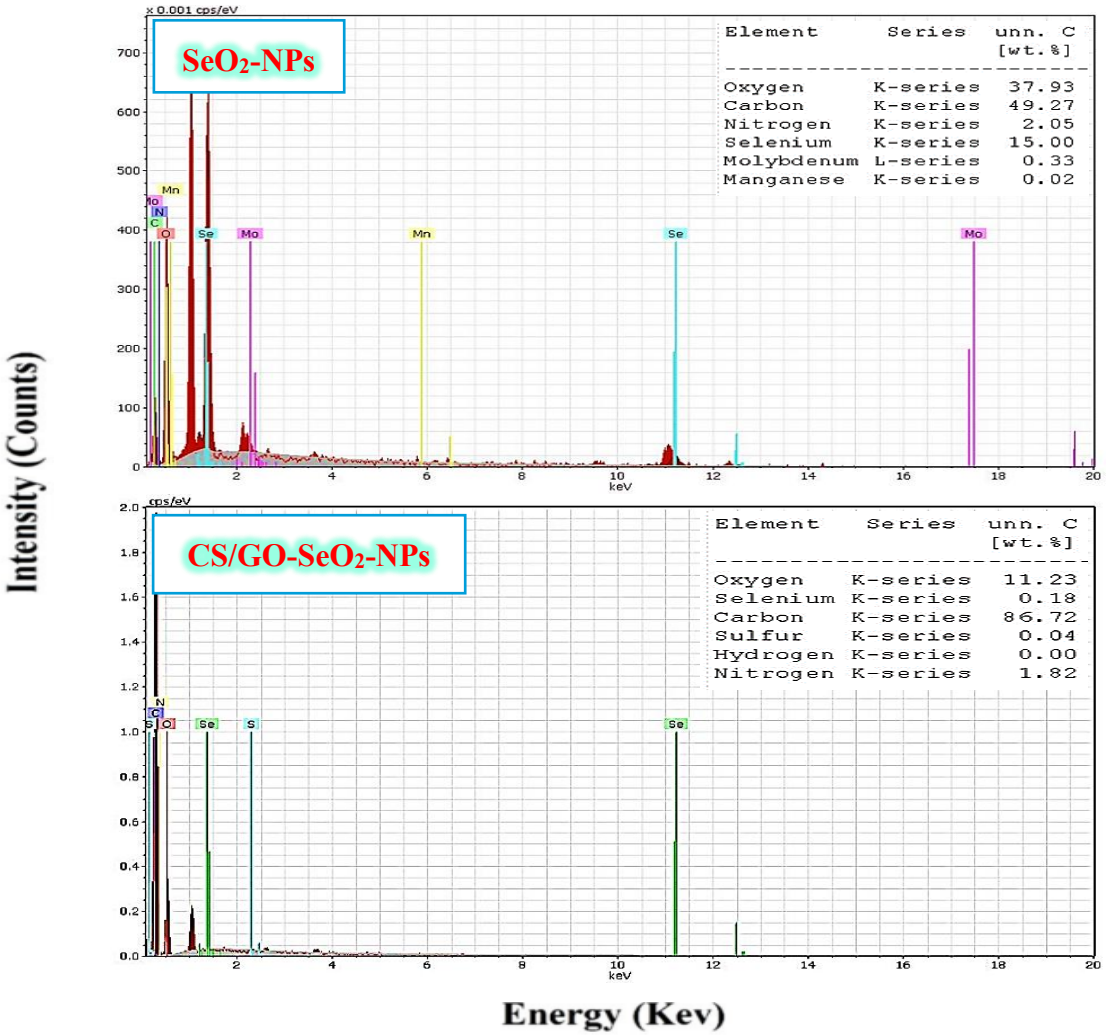

Figure 3.3 EDX Spectra of SeO_2-NPs, and CS/GO-SeO_2-NPs.

The chemical constituents of the sample were analyzed by EDX, which yielded about 85% pure selenium. For the SeO_2-NPs, the models are

illustrious as C, N, O, and Se. Figure 3.3 shows oxygen and Se elements in the synthesized sample. It can be observed that the present atoms were distributed similarly to C (49.2 wt.%), N (2.05 wt.%), O (37.9 wt.%), and Se (15.0 wt.%) atoms in the produced CS/GO-SeO_2-NPs. Furthermore, based on the literature, the C, N, and O atoms correspond to the CS molecule[238]. The produced SeO_2-NPs (brilliant NPs; red color) extended endlessly within CS atoms, as seen in the photos (C, N, and O) [239, 240].

3.1.4 Fourier Transform Infrared Spectrophotometry of SeO_2-NPs and CS/GO-SeO_2-Nps.

FTIR spectroscopy analysis was conducted to confirm the functional groups present in the colloidal form of the chitosan embedded SeO_2 nanoparticles and CS/GO-SeO_2-NPs as shown in Figure 3.4.

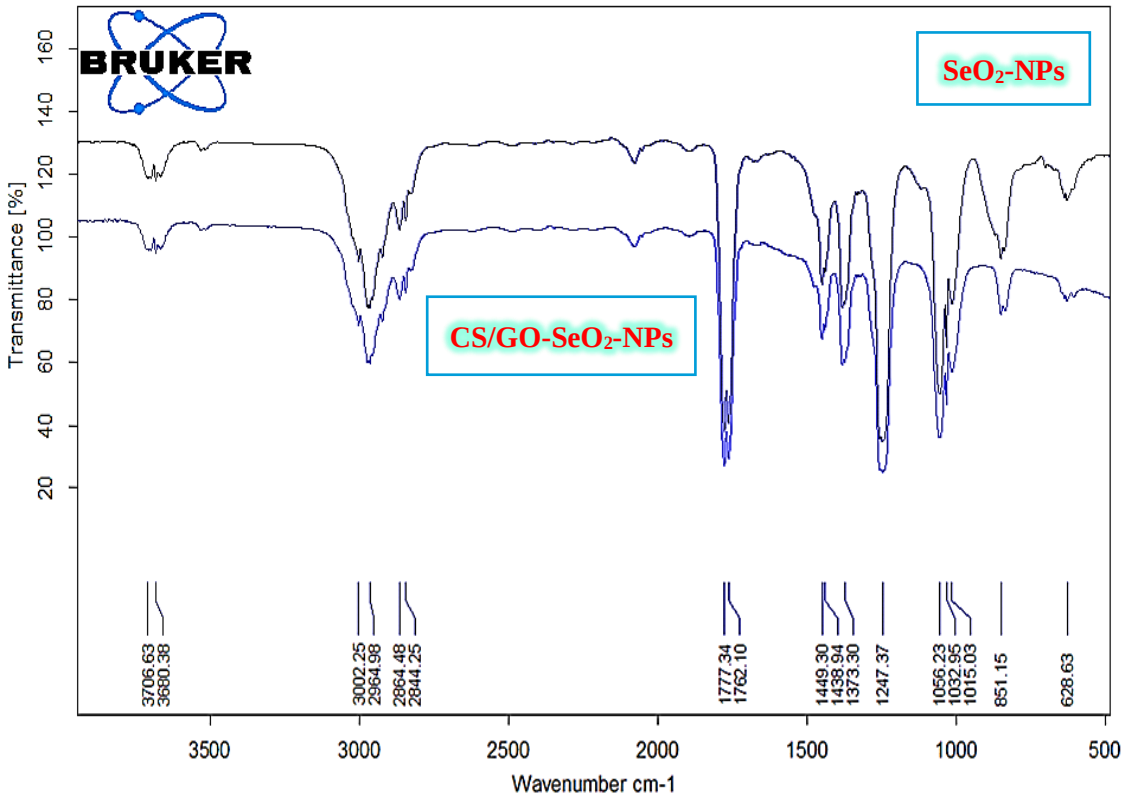

Figure 3.4. FTIR Spectra of SeO_2-NPs, and GO /CS-SeO_2-NPs.

The band at 1562.39 cm^{-1} in the spectra of CS/GO-SeO_2-NPs is assigned to the stretching vibration of the amino group (NH_2) of chitosan (CS). The C–O stretching vibration peak in CS-SeO_2-NPs was 1076.32 cm^{-1}. The peaks around 851.15 and 1247.37 cm^{-1} correspond to Chitosan's saccharide structure, showing that CS is present on the surface of these nanoparticles, (C–H) vibration has another peak at 1438.94 cm^{-1}. The amine (NH) symmetric vibration in CS/GO-SeO_2-NPs produces a band at 3412.19 cm^{-1}. The absorption peak at 3425.69 cm^{-1} is attributed to the (OH) stretching frequency of CS, and it can be identified as OH on the surface of Se-NPs. The symmetric and antisymmetric stretching vibrations of the C–H groups are related to the absorption bands at 2864.48 cm^{-1} and 2964.98 cm^{-1}, respectively. Furthermore, stretching vibration maxima for C–, O and C–C emerge at 1076.32 and 1373.30 cm^{-1}, respectively.

SeO_2-NPs feature a variety of fundamental vibrational modes, according to the literature. The peaks at 628 and 851 cm^{-1} ascribed to the v2 and v3 vibrational modes, respectively. Typical characteristic peaks of the saccharide moiety, with absorption peaks about 1157 and 1082 cm^{-1} [241, 242]. The bending and rocking vibrational modes of the C–H and C bands are responsible for the peaks below 1500 cm^{-1}. The distinct peaks at 1677, 1581 cm^{-1} represent –NH_2 bending vibration, whereas the inter and intramolecular hydrogen bonds with –OH, carboxyl, and amine groups were found at roughly 3200–3680 cm^{-1} corresponding to –OH and –NH_2 stretching vibration [243].

3.1.5 Dynamic Light Scattering of SeO_2-NPs and CS/GO-SeO_2-Nps

The dynamic light scattering (DLS) of SeO_2-NPs and CS/GO-SeO_2-Nps are presented in Figure 3.5.

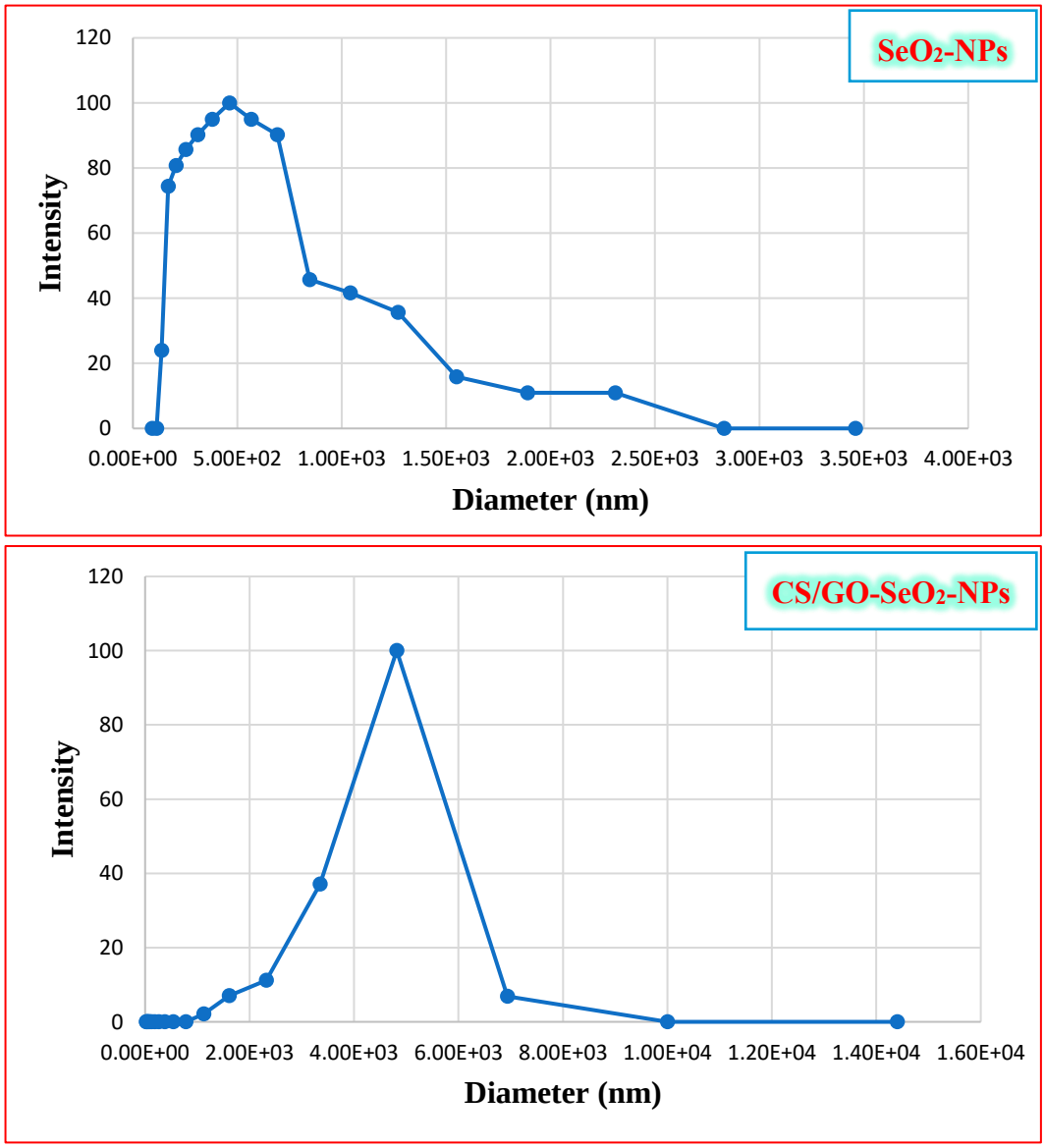

Figure 3.5 Dynamic Light Scattering of SeO_2-NPs, and CS/GO-SeO_2-NPS.

The average particle diameter and particle diameter distribution of nano-sized particles scattered in a liquid were measured using dynamic light scattering (DLS). A measuring method and measurement case for particle diameter analysis of nanoparticle products utilizing laser light were discussed previawly. The existence of two-dimensional zones in the dispersion diagram and the large size distribution of CS/GO-SeO_2-NPs in the samples are likely related to differences in nanocomposites' production circumstances.

The formation of CS/GO-SeO_2-NPs in an aqueous solution is a multi-stage process that may be divided into four stages [244, 245]. The first stage involves the production of selenium atoms through the reduction of previously synthesized extremely reactive selenide anions. The creation of a metastable phase with subsequent transition to a thermodynamically stable state, as well as an increase in the amount of local fluctuations in the bulk of the first phase, describe the second stage.

As a result of the reversible connection of ensembles of selenium atoms, the crucial nucleus of a new phase is formed (after overcoming energy barriers). The nuclei generated in the first step continue to expand in the third stage due to sorption. GO Nano sheet create nanoparticles and then stabilize them covalently and electrostatically (fourth stage).

3.1.6 Zeta Potential Analysis of SeO_2-NPs and CS/GO-SeO_2-Nps

Zeta potential results of SeO_2-NPs and CS/GO-SeO_2-Nps are shown in Figure 3.6.

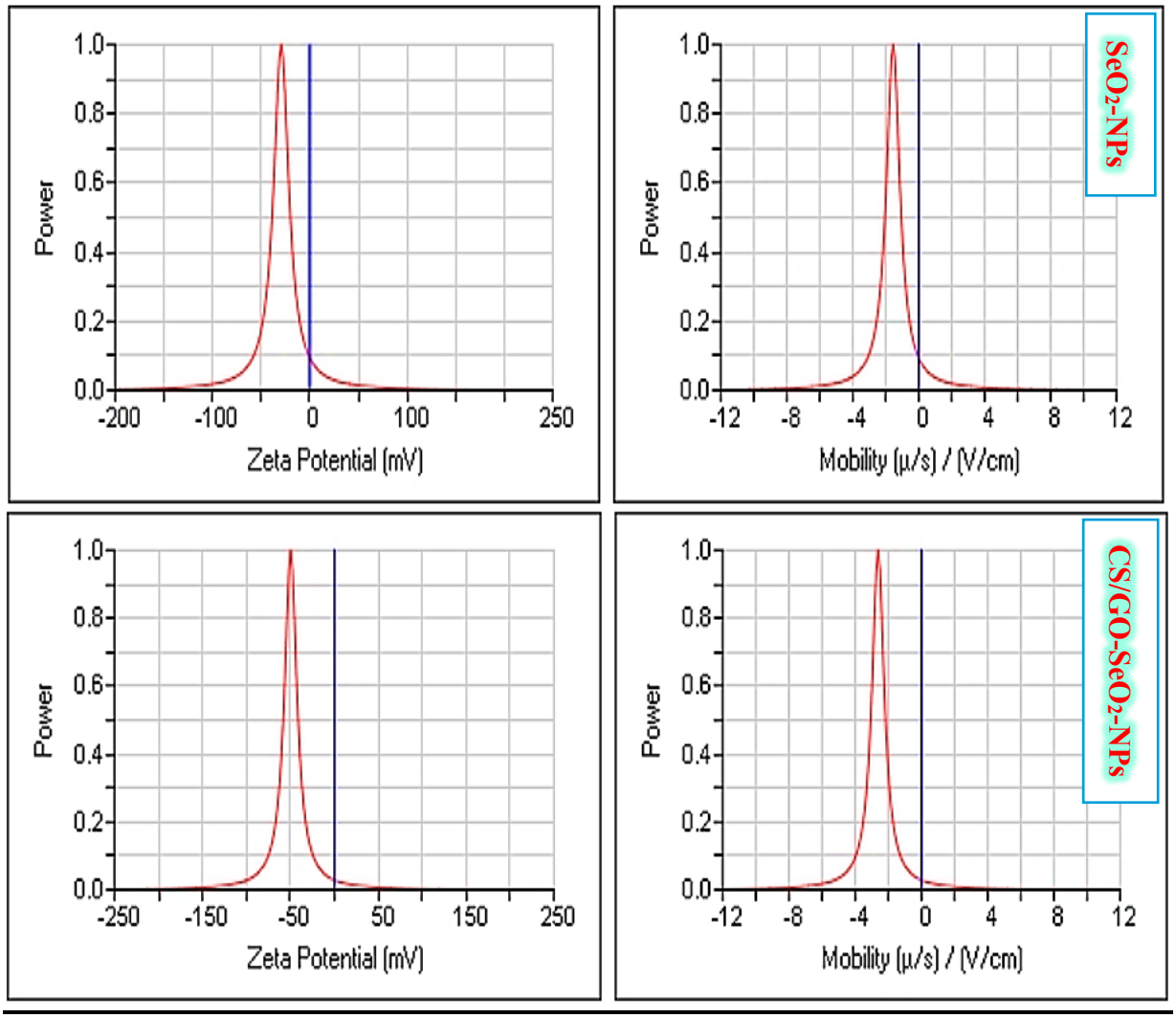

Figure 3.6. Zeta Potential Analysis of SeO_2-NPs, and CS/GO-SeO_2-NPS.

The zeta potential, which shows the NPs' surface charge and potential attraction to the cells, was also measured, with values ranging from -29.38 to -49.61 mV. Because all samples have CS on their surfaces, and CS has positive groups at pH = 7.4, the range is negatively charged. In general, the rate at which NPs are internalized by cells is determined by their surface charges, with positively charged NPs being taken up more quickly than

neutral and negatively charged NPs. This is due to negatively charged molecules on surfaces repelling negatively charged nanoparticles. However, other researchers believe that there are just a few cationic spots on cell surfaces that can adsorb and bind to negatively charged particles [246]. They theorized that when negatively charged NPs connect to cationic sites, they form clusters (agglomerates) due to the repulsion shown by the vast negatively charged domains of the cell surface [247]. Furthermore, the charge density on the cell surface is reduced by the bound NPs, which may facilitate the adsorption of other free NPs.

3.2 Adsorption Experiments

Initially, the results of the adsorption were entered in Langmuir and Freundlich equation. All the results did not obeyed Langmuir equations ($r<0.3$). While the application of Freundlich equation produce a high r-values (>0.7). Therefore, we consider only the Freundlich equation for all adsorption processes of the present study.

3.2.1 Adsorption of Follicle-Stimulating Hormone (FSH) on CS/GO-SeO_2-NPs

The adsorption isotherms of FSH on CS/GO-SeO_2-NPs surface are presented in Figure 3.7 and the logarithmic form in Figure 3.8.

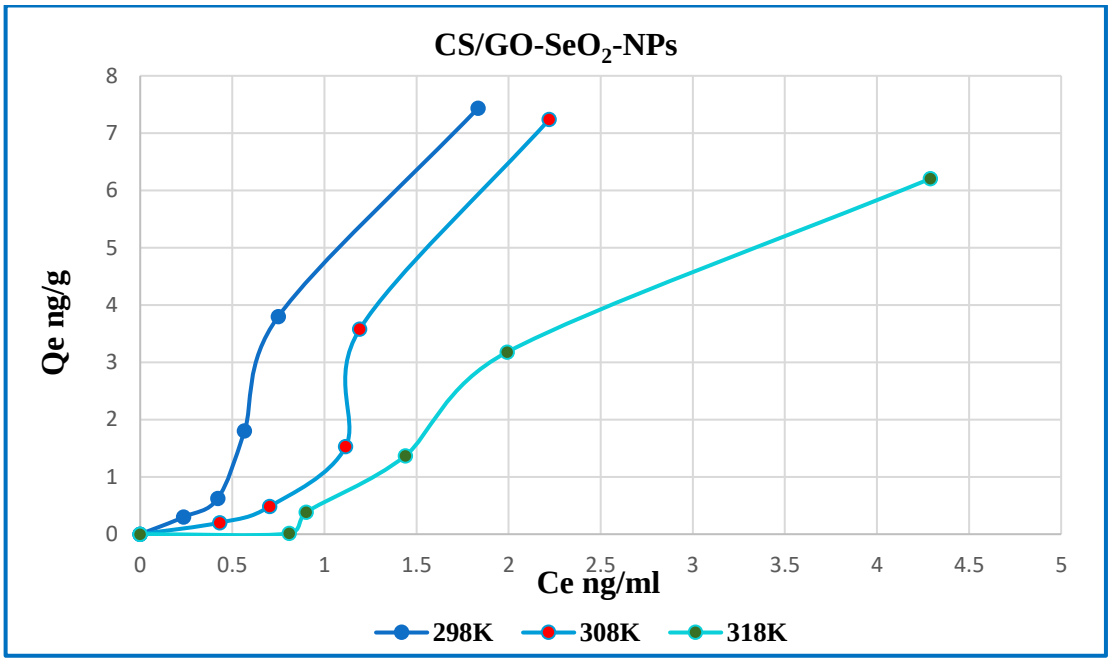

Figure 3.7 Adsorption Isotherms of FSH Hormone on the CS/GO-SeO$_2$-NPs surface.

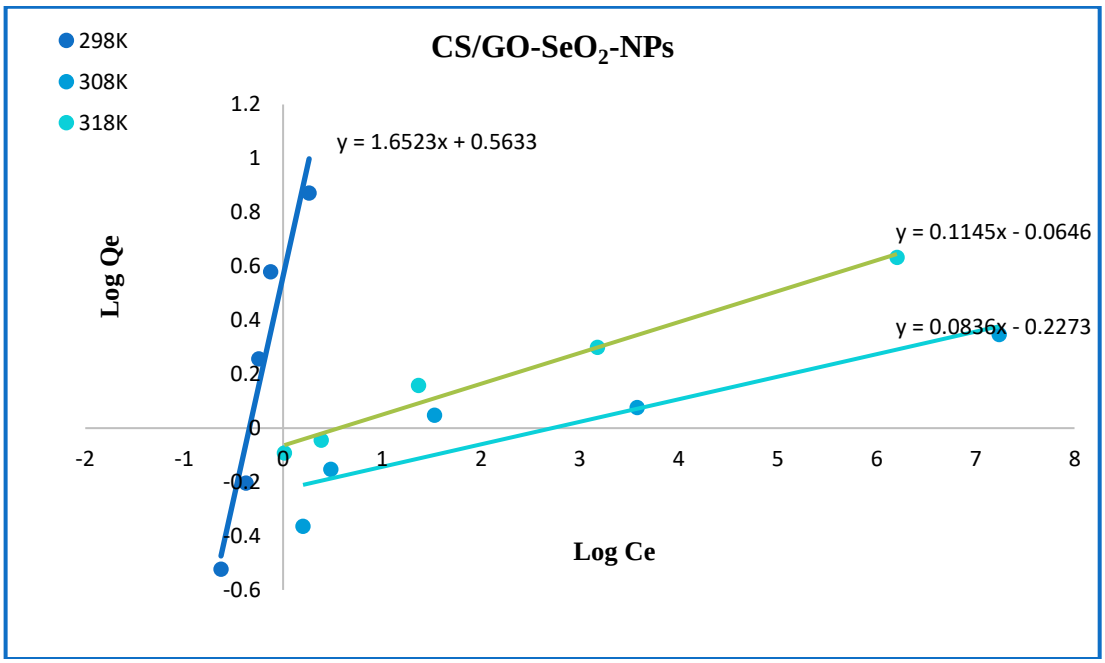

Figure 3.8 Freundlich Lines of the Adsorption of FSH Hormone on the CS/GO-SeO$_2$-NPs Surface.

Table 3.1 Adsorption of FSH on CS/GO-SeO_2-NPs

Temp ^{0}C	C_o FSH ng/ml	C_e FSH ng/ml	Qe ng/g	Log Ce	Log Qe
25 ^{0}C	0.835	0.236	0.300	-0.628	-0.523
	1.670	0.421	0.624	-0.376	-0.204
	4.175	0.567	1.804	-0.247	0.256
	8.350	0.750	3.800	-0.125	0.580
	16.700	1.834	7.433	0.263	0.871
35 ^{0}C	0.835	0.432	0.202	-0.365	-0.696
	1.670	0.703	0.483	-0.153	-0.316
	4.175	1.116	1.530	0.048	0.185
	8.350	1.192	3.579	0.076	0.554
	16.700	2.221	7.239	0.347	0.860
45 ^{0}C	0.835	0.809	0.013	-0.092	-1.886
	1.670	0.902	0.384	-0.045	-0.416
	4.175	1.439	1.368	0.158	0.136
	8.350	1.993	3.179	0.299	0.502
	16.700	4.290	6.205	0.632	0.793

FSH hormone can be adsorbed on the surface of CS/GO-SeO_2-NPs spontaneously. Changes in protein structure are linked to this adsorption. The current study's findings shed light on the effect of CS/GO-SeO_2-NPs on protein structures and, as a result, adsorption isotherms were constructed for the adsorption of FSH on NPs at 25, 35, and 45 °C (Figures 3.7, and 3.8). The isotherms generally showed a slight increase in the quantity of adsorbed FSH (Qe) as FSH equilibrium concentration (Ce) increased. Thus, the adsorption tendency is very low at low FSH concentration and showed a rapid increase in Qe at higher FSH concentration. The applicability of the Freundlich equation (Figure 3.8) indicates the heterogeneity of a surface. By non-covalent protein-CS/GO-SeO_2-NPs conjugation, Freundlich isotherms indicate various forces on the surface or hormone molecules to induce heterogeneity. The initial direction of curvature of the adsorption isotherms (Figure 3.7) shows that

as the concentration rises, adsorption becomes easier, and more adsorbate is adsorbed over the first monolayer of protein. That is, molecules interact with one another side by side, causing them to stick to the surface more. The opposite force of the protein molecules' attraction to water pulls this molecule as far as possible into the water phase, and the net of these forces represents the adsorption intensity [248].

Protein molecules lose their ability to move in solution freely and are organized on the surface of the CS/GO-SeO_2-NPs by various forces. Conformational variations can considerably influence the driving force for adsorption in the protein. These results have been noticed previously [249]. In hormone adsorption, electrostatic interactions between the protein and the NPs are unimportant. When the protein and the sorbent have the same charge sign, adsorption can still happen spontaneously and even exothermic. This complicated dependence implies that no single interaction is responsible for the enthalpy shift. As a result, ΔH° of the adsorption can only be evaluated if enough other information about the whole adsorption process is known [250].

Because of the increased molecular interactions that generate a negative ΔH°, the enthalpy (ΔH°) of transfer of polar groups from the protein inside to the outside section to touch water molecules tends to be negative as temperature rises [251]. While the ΔH° of the non-polar group transfer from the protein inside into water is positive above 25 ^{0}C to overlap the repulsion, the ΔH° of polar group transfer from the protein interior into water is negative below 25 ^{0}C [252]. Both non-polar and polar groups have negative hydration entropies at room temperature [253]. They indicate that both create order in the aqueous environment. However, these entropies differ concerning how they change with increasing temperature.

Non-polar groups' hydration entropy decreases as temperature rises, indicating that they are less able to order water at higher temperatures and may contribute to its disorder by interfering with the size of the hydrogen-bonded network and permitting simpler water molecule rotation. When the protein is unfolded, there is also an entropy gain due to the increased freedom of the non-polar groups.

On the other hand, polar groups have a lower entropy of hydration, which becomes more negative as the temperature rises because they can construct ordered hydration shells even from more disordered water. As a result, compared to merely water, the water is more organized around hydrophilic groups as the temperature rises, and the negative heat capacity of this hydrophilic hydration [254]. Hormones spontaneously bind to the surface of NPs due to changes in protein structure and an electrostatic attraction mechanism [255]. Adsorption parameters of the adsorption of FSH hormone on the NPs surface. Figure 3.9 shows the Vant’s Hoff lines of the adsorption of FSH on the CS/GO-SeO_2-NPs composites surface.

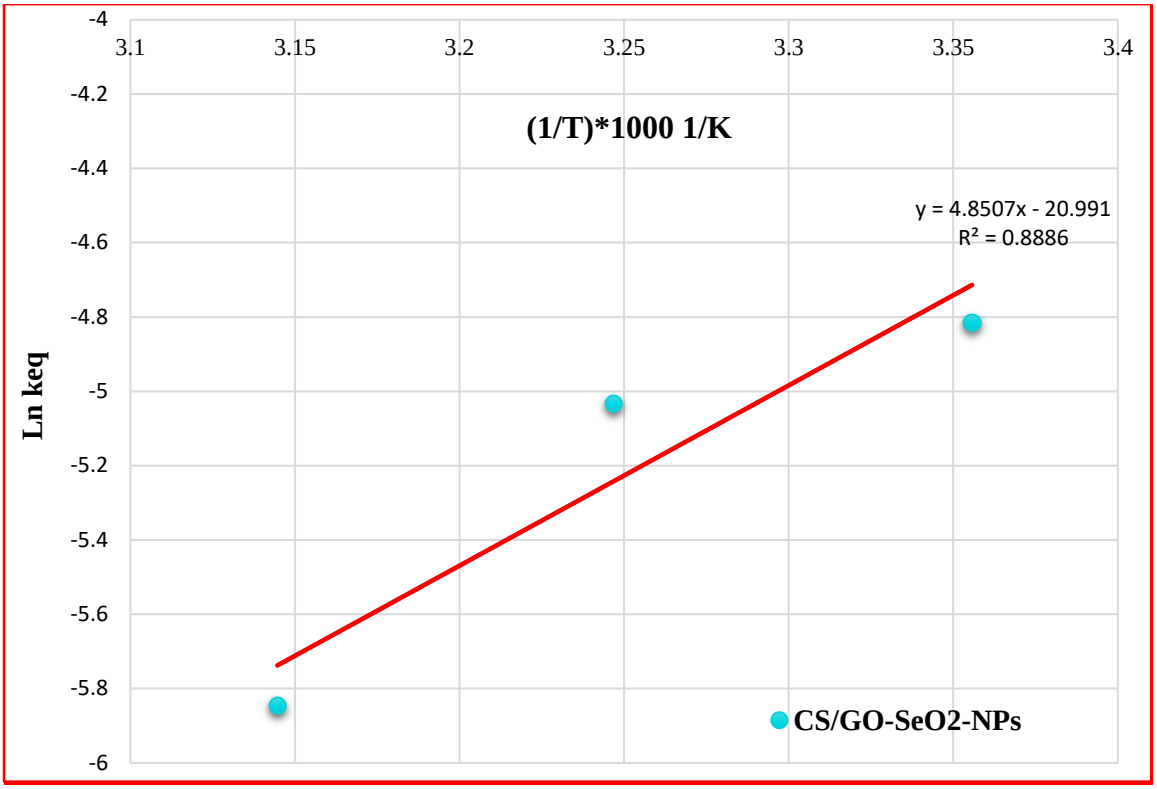

Figure 3.9 Vant's Hoff Lines of the Adsorption of FSH on the NPs Composites.

Table 3.2 Thermodynamic Functions of the Adsorption of FSH on the CS/GO-SeO_2-NPs Composites.

NPs	(1/T)*1000	Xm=Keq	ln Xm	Slope	ΔG° KJ/mol	ΔH° KJ/mol	ΔS° J/mol.k
CS/GO-SeO_2-NPs	3.356	0.008107	-4.815	4.851	11.930	-40.329	-175.364
	3.247	0.006519	-5.033				
	3.145	0.002893	-5.846				

The Vant-Hoff's lines for the adsorption of FSH on CS/GO-SeO_2-NPs are presented in Figure 3.9. The results of the thermodynamic parameters are presented in Table 3.2. Results showed that the adsorption process is exothermic because of the fixation of FSH onto the NPs surfaces. The free energy reveals many small proteins, comparable to the contribution from only a few hydrogen bonds. Because changes in the protein's environment

or the mutation of only a few interactions out of thousands in the native state can tip the balance and shift an active protein into a nonfunctional, misfolded, or aggregated form, this thermodynamic stability has far-reaching implications [256]. The reason for the stability of many natural proteins is only the analysis of forces that stabilize the native state and the design principles that disfavor non-native, misfolded, or aggregated forms. Proteins from hyperthermophilic species have several molecular characteristics that explain why they are more thermally stable than their mesophilic homologs [257, 258].

3.2.2 Adsorption of Luteinizing Hormone (LH) on CS/GO-SeO_2-NPs

Figure 3.10 shows the spontaneous adsorption of LH hormone on the surface of CS/GO-SeO_2-NPs and the applicability of the Freundlich equation.

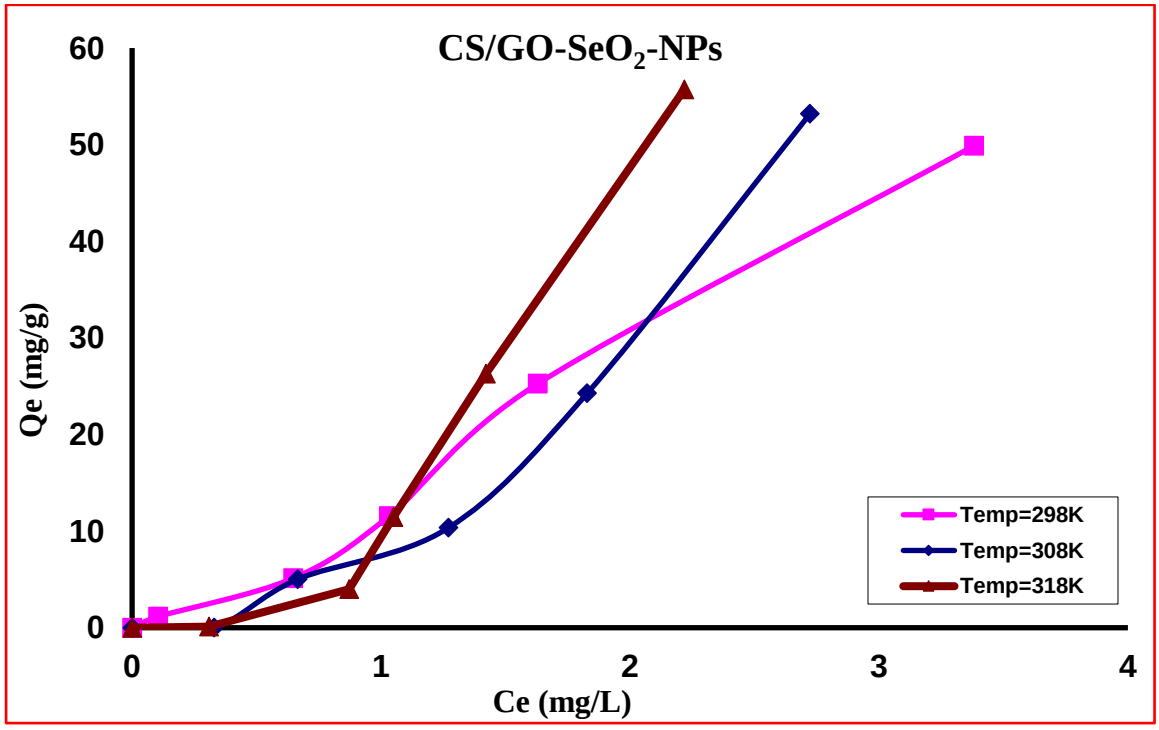

Figure 3.10 Adsorption Isotherms of LH Hormone on The CS/GO-SeO_2-NPs Surface.

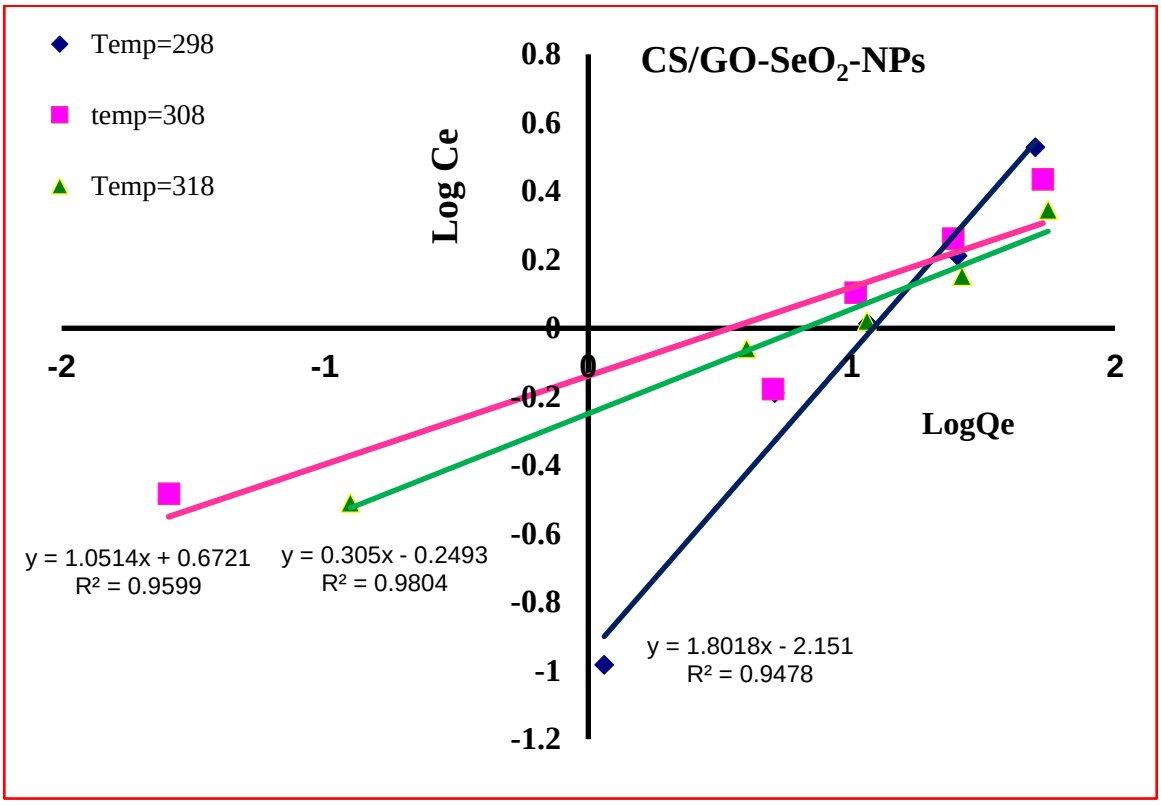

Figure 3.11 Freundlich Lines of the Adsorption of LH Hormone on the CS/GO-SeO_2-NPs Surface.

The main finding of the present study is the ability of the LH hormone to be adsorbed spontaneously on the surface of CS/GO-SeO_2-NPs. Whether the changes in protein structure accompany the adsorption process or not needs further studies. The applicability of the Freundlich equation (Figure 3.11) indicates the heterogeneity of a surface [259].

Table 3.3 Adsorption of LH on CS/GO-SeO_2-NPs

Temp ^{0}C	Co ng/g	Ce ng/g	Log Ce	Co-Ce	Qe ng/g	Log Qe	Ce/Qe
25 °C	0.000	0.000	0.000	0.000	0.000	0.000	0.000
25 °C	0.334	0.104	-0.983	0.23	1.15	0.060698	0.090435
25 °C	1.67	0.647	-0.189	1.0231	5.1155	0.708888	0.126459
25 °C	3.34	1.032	0.014	2.308000135	11.54	1.062206	0.089428
25 °C	6.68	1.629	0.212	5.050609	25.25305	1.402314	0.064523
25 °C	13.36	3.382	0.529	9.977594962	49.88797	1.697996	0.0678
35 °C	0.000	0.000	0.000	0.000	0.000	0.000	0.000
35 °C	0.334	0.329	-0.483	0.005108147	0.025541	-1.59277	12.87715
35 °C	1.67	0.665	-0.1769	1.004567647	5.022838	0.700949	0.132481
35 °C	3.34	1.271	0.104081	2.069189317	10.34595	1.01477	0.122832
35 °C	6.68	1.828	0.261983	4.851973191	24.25987	1.385	0.075352
35 °C	13.36	2.723	0.435035	10.63708141	53.18541	1.725792	0.051197
45 °C	0.000	0.000	0.000	0.000	0.000	0.000	0.000
45 °C	0.334	0.309	-0.51004	0.025	0.125	-0.90309	2.472
45 °C	1.67	0.872	-0.05951	0.798054158	3.990271	0.601002	0.218518
45 °C	3.34	1.049	0.020775	2.291	11.455	1.058995	0.091576
45 °C	6.68	1.421	0.152495	5.259324375	26.29662	1.4199	0.054025
45 ^{0}C	13.36	2.218	0.345983	11.14189216	55.70946	1.745929	0.039816

Through the protein-CS/GO-SeO_2-NPs conjugation, Freundlich isotherms (Figure 3.11) indicate various forces on the surface or hormone molecules to induce heterogeneity. The initial direction of curvature of the adsorption isotherms (Figure 3.10) shows that as the concentration rises, adsorption becomes easier, and more adsorbate were adsorbed over the first monolayer of protein. That is, molecules interact with one another side by side, causing them to stick to the surface more. The opposite force of the protein molecules' attraction to water pulls this molecule as far as

possible into the water phase, and the net of these forces represents the adsorption capacity [260].

Protein molecules lose their ability to move in solution freely and are organized on the surface of the CS/GO-SeO_2-NPs by various forces. Conformational variations can considerably influence the driving force for adsorption in the protein. These results were noticed previously [249]. In hormone adsorption, electrostatic interactions between the protein and the NPs are unimportant. When the protein and the sorbent have the same charge sign, adsorption can still happen spontaneously and even exothermic. This complicated dependence implies that no single interaction is responsible for the enthalpy shift. As a result, ΔH° of the adsorption can only be evaluated if enough other information about the whole adsorption process is known [250].

Because of the increased molecular interactions that generate a negative ΔH°, the ΔH° of transfer of polar groups from the protein inside to the outside section to touch water molecules tends to be negative as temperature rises [261]. While the ΔH° of the non-polar group transfer from the protein inside into water is positive above 25 °C to overlap the repulsion, the ΔH of polar group transfer from the protein interior into water is negative below 25 °C [262]. Both non-polar and polar groups have negative hydration entropies at room temperature [263]. Both establish order in the watery environment, according to their findings. However, the way these entropies alter as temperature rises is different. The hydration entropy of non-polar groups diminishes as temperature rises, showing that they are less able to order water at higher temperatures and may even contribute to its disorder by interfering with the size of the hydrogen-bonded network and allowing for easier water molecule rotation. Because

the non-polar groups have more freedom when the protein is unfolded, there is an increase in entropy.

On the other hand, polar groups have a lower entropy of hydration, which becomes more negative as the temperature rises because they can construct ordered hydration shells even from more disordered water. As a result, compared to merely water, the water is more organized around hydrophilic groups as the temperature rises, and the negative heat capacity of this hydrophilic hydration [254]. Hormones spontaneously bind to the surface of CS/GO-SeO_2-NPs due to changes in protein structure and an electrostatic attraction mechanism [255].

Adsorption parameters of the adsorption of LH hormone on the NPs surface. Figure 3.12 shows the Vant's Hoff lines of the adsorption of LH on the CS/GO-SeO_2-NPs composites surface.

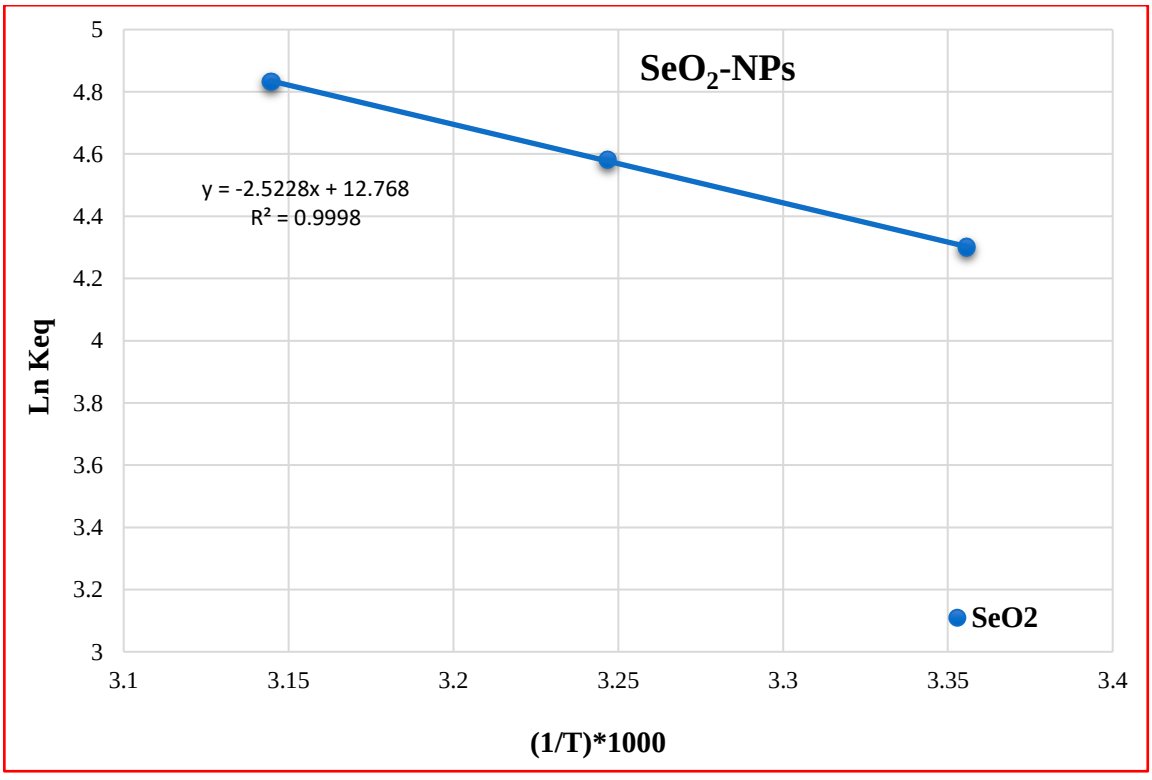

Figure 3.12 Vant's Hoff Lines of the Adsorption of LH on the NPs Composites.

Table 3.4 Thermodynamic Functions of the Adsorption of LH on the CS/GO-SeO_2-NPs Composites.

NPs	(1/T)*1000	Xm=Keq	ln Xm	Slope	ΔG° KJ/mol	ΔH° KJ/mol	ΔS° J/mol.k
CS/GO-SeO_2-NPs	3.356	73.74631	4.300631	-2.523	-10.655	20.975	106.140
	3.247	97.6625	4.581518				
	3.145	125.5788	4.832933				

The Vant-Hoff's lines for the adsorption of LH on NPs are presented in Figure 3.12. The results of the thermodynamic parameters are presented in Table 3.4. Results showed that the adsorption process is endothermic, reducing entropy, leading to more regularity and less randomization because of the fixation of LH onto the NPs surfaces. Therefore, the study of material biocompatibility begins with analyzing protein absorption onto surfaces [264]. Studies of various NP surfaces and proteins indicate the perturbation of protein structure at varying extents.

The number of binding sites on NPs is determined by the size of the NPs and protein. However, the hydrophobicity of the NP strongly influences its protein binding properties [169]. Therefore, quantitative characterization of nanoscale surfaces to determine the amount, structure, and distribution of adsorbed proteins is necessary to understand cell-nanostructured surface interactions. Although the protein may retain most of its native structure after adsorption on the NPs surface, in some cases, the thermodynamic stability of the protein is decreased, causing the protein to be more sensitive to chemical denaturants [265]. Considering that changes in protein structure or stability may lead to loss of biological function.

3.3 Characteristics of the Prepared Nanoparticles MoO_2-NPs and CS/GO- MoO_2-Nps

Characterization of MoO_2-NPs and CS/GO-MoO_2-Nps, which were prepared, was studied using different analytical instruments such as X-rays diffraction (XRD), Scanning electron microscopy (SEM), Energy dispersive X-rays spectroscopy (EDX), Fourier transform technique (FT-IR), UV-Visible spectroscopy, Dynamic Light Scattering (DLS), Zeta potential analysis and ELISA Reader.

3.3.1 X-rays Diffraction (XRD) of MoO_2-NPs and CS/GO-MoO_2-Nps

XRD analyzed the prepared molybdenum oxide for the determination of phase and symmetry. Figure 3.13 shows the XRD patterns for molybdenum oxide

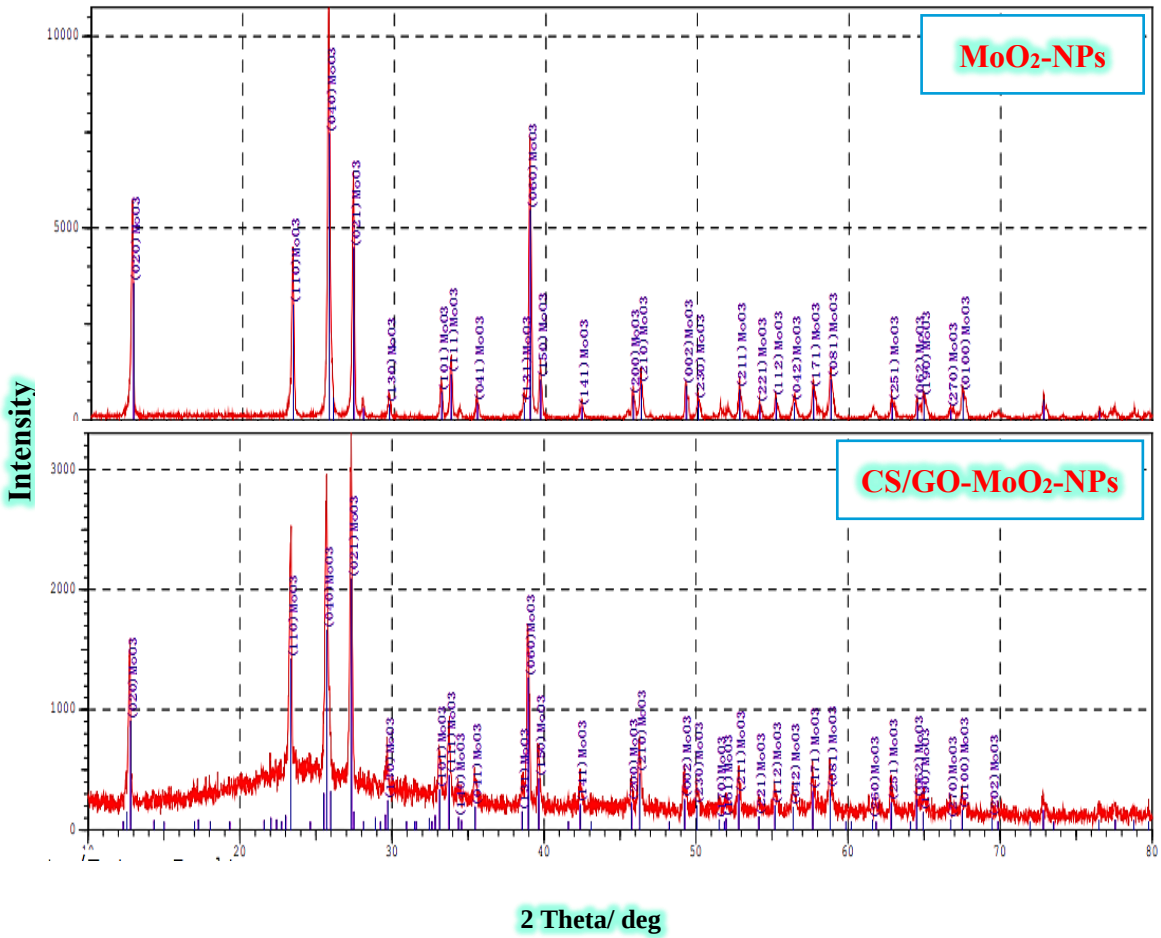

Figure 3.13 XRD Patterns of MoO_2-NPs and CS/GO-MoO_2-NPs.

X-rays analysis of the molybdenum oxide particles was performed using an X-rays diffractometer. Figure 3.13 represents the XRD patterns for MoO_2-NPs powders. According to the obtained results, the purity of the MoO_2-NPs was characterized, and it shows a high level of purity of MoO_2-NPs. The nanoparticles in which the number of peaks is observed at 25^0 angles due to the formation of high crystalline molybdenum oxide nanorods. The peaks were observed at 2θ 25.7, 27.3, 38.9, 46.2, 58.8, 67.5, and 72.8. Sharp peaks were obtained corresponding at (111), (110), (150), (200), (251), (260), and (312), indicating the MoO_2 and which were found to be highly crystalline [266, 267].

The addition of graphene oxide (GO) to the synthezed of MoO_2-NPs allowed for obtaining smaller crystallites. Graphene oxide has many functional groups that can serve as nucleation sites for MoO_2 particles. The obtained particles are smaller, which can be attributed to the better mixing conditions, and due to the lower temperature of MoO_2/GO, the hybrid nanostructures show lower crystallinity. Furthermore, based on literature, the crystallite size is estimated based on line broadening analysis using Scherrer's equation [4]. The Crystal size was 29 nm. Thus, the results confirm the addition of graphene oxide. It increases the crystal size of CS/GO-MoO_2-NPs.

3.3.2 Scanning Electron Microscopy (SEM) of MoO_2-NPs and CS/GO- MoO_2-Nps.

The SEM analysis was done to study the surface morphology of MoO_2-NPs nanoparticles and CS/GO-MnO_2-NPs, as shown in Figure 3.14.

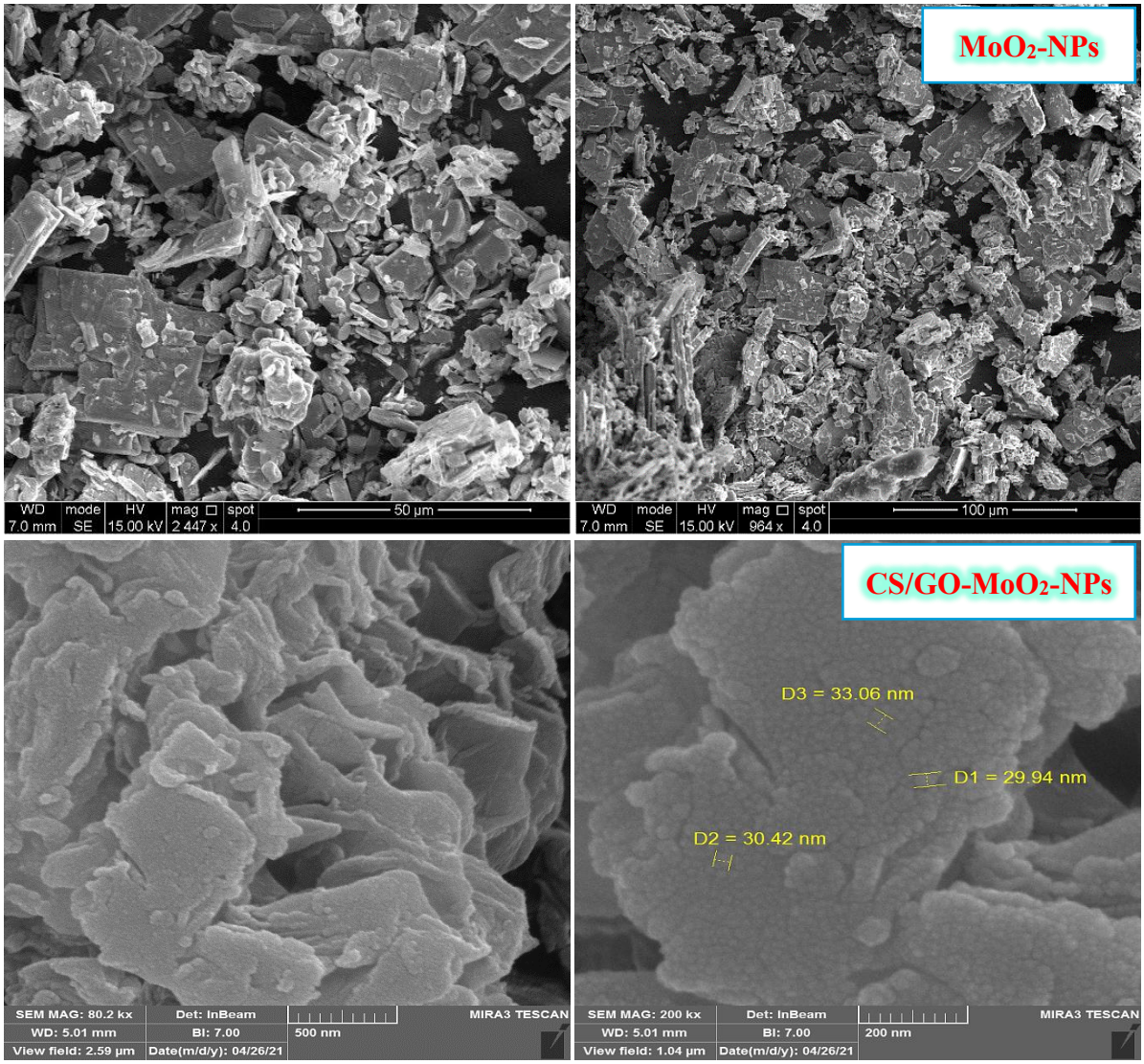

Figure 3.14 SEM Images of MoO_2-NPs, and CS/GO-MoO_2-NPs.

The surface morphology of MoO_2 nanoparticles was investigated using SEM. The size distribution of MoO_2-NPs nanoparticles was quite uniform, as evidenced by micrographs showing the SEM image of CS/GO-MoO_2-NPs composite. A large number of MoO_2 particles in nano-size were observed in low magnification. The high magnification SEM observation in Figure 3.14 indicates clearly that the graphene is well penetrated in MoO_2 particles, suggesting the successful formation of CS/GO-MoO_2-NPs nanocomposite.

The majority of the particles in the low magnification SEM image show that all of the MoO_2 particles were formed in nano-scales (with an average diameter of 29 nm), and were tightly packed in graphene. Based on the literature and the fact that the population of irregularly shaped particles was very small relative to the population of regular-shaped particles, it can be assumed that the MoO_2 nanoparticles had a very uniform shape. In low magnification, numerous MoO_2 nanoparticles were visible. The high magnification SEM observation Figure 3.14 shows that the graphene sheets were well penetrated in MoO_2 particles, indicating that the CS/GO-MoO_2 nanocomposite was successfully formed.

3.3.3 Energy Dispersive X-rays Spectroscopy (EDX) of MoO_2-NPs and CS/GO- MoO_2-Nps.

Figure 3.15 shows the elemental mapping pictures of CS/GO-MoO_2- NPs.

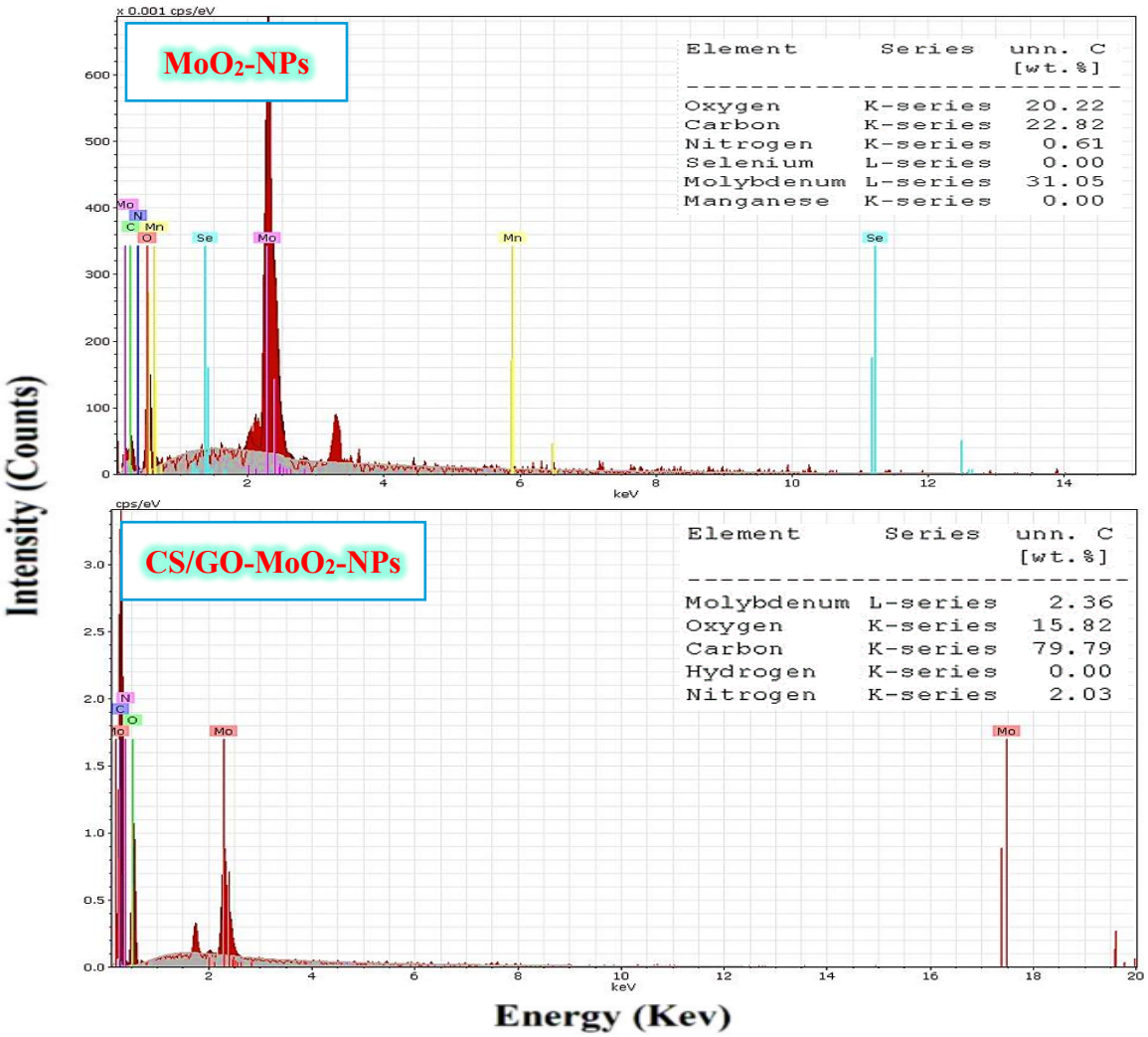

Figure 3.15 EDX Spectra of MoO_2-NPs, and CS/GO-MoO_2-NPs.

The typical EDX spectrum collected shows that the nanomaterial contains only elements of Mo and O. However, it is difficult to determine the Mo/O ratio of the nanoparticle quantitatively due to the uncertainty of intensity of the EDX detection for lighter elements. It should be observed that the present atoms were distributed similarly to C, N, O, and Mo atoms in the produced MoO_2-NPs. It can be seen that Mo and O are uniformly dispersed on CS, proving that MoO_2-NPs were successfully dispersed and loaded on GO.

3.3.4 FTIR spectrum of MoO_2-NPs and CS/GO- MoO_2-Nps.

The FTIR spectroscopy was done to study the functional groups present in the obtained product, as in Figure 3.16.

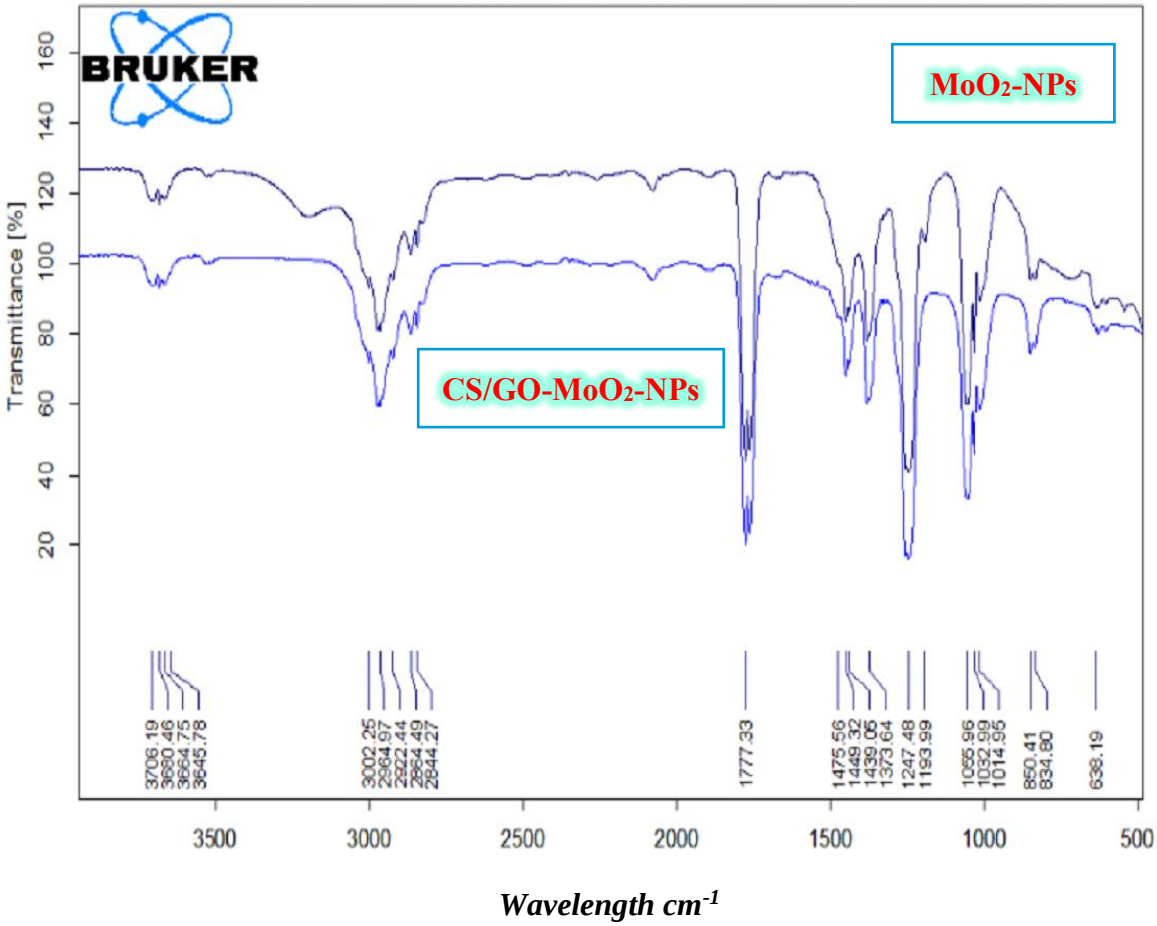

Figure 3.16 FTIR Spectra of MoO_2-NPs, and CS/GO-MoO_2-NPs.

In FT-IR spectra, for MoO_2, the peaks detected at 943, 850, and 835 cm^{-1} correspond to the vibrations of Mo=O and Mo–O–Mo, respectively. The band at 1645 cm^{-1} is attributed to the bending of hydroxyl groups on its surface. The peaks at 3664 cm^{-1} may be assigned to the stretching mode (νOH) of adsorbed H_2O and –OH groups. Peaks at 1373 cm^{-1}, 1548 cm-1, 1777 cm^{-1}, 2844 cm^{-1}, 3002 cm^{-1}, and 3680 cm^{-1}, are correspond to functional groups C-H (alkane), C-C (aromatic), C=O (carboxylic acid), O-H (carboxylic acid), N-H (amine), and O-H (alcohol), respectively [268].

3.3.5 Dynamic Light Scattering of MoO_2-NPs and CS/GO-MoO_2-Nps.

The results of dynamic light scattering (DLS) for these materials are shown in Figure 3.17.

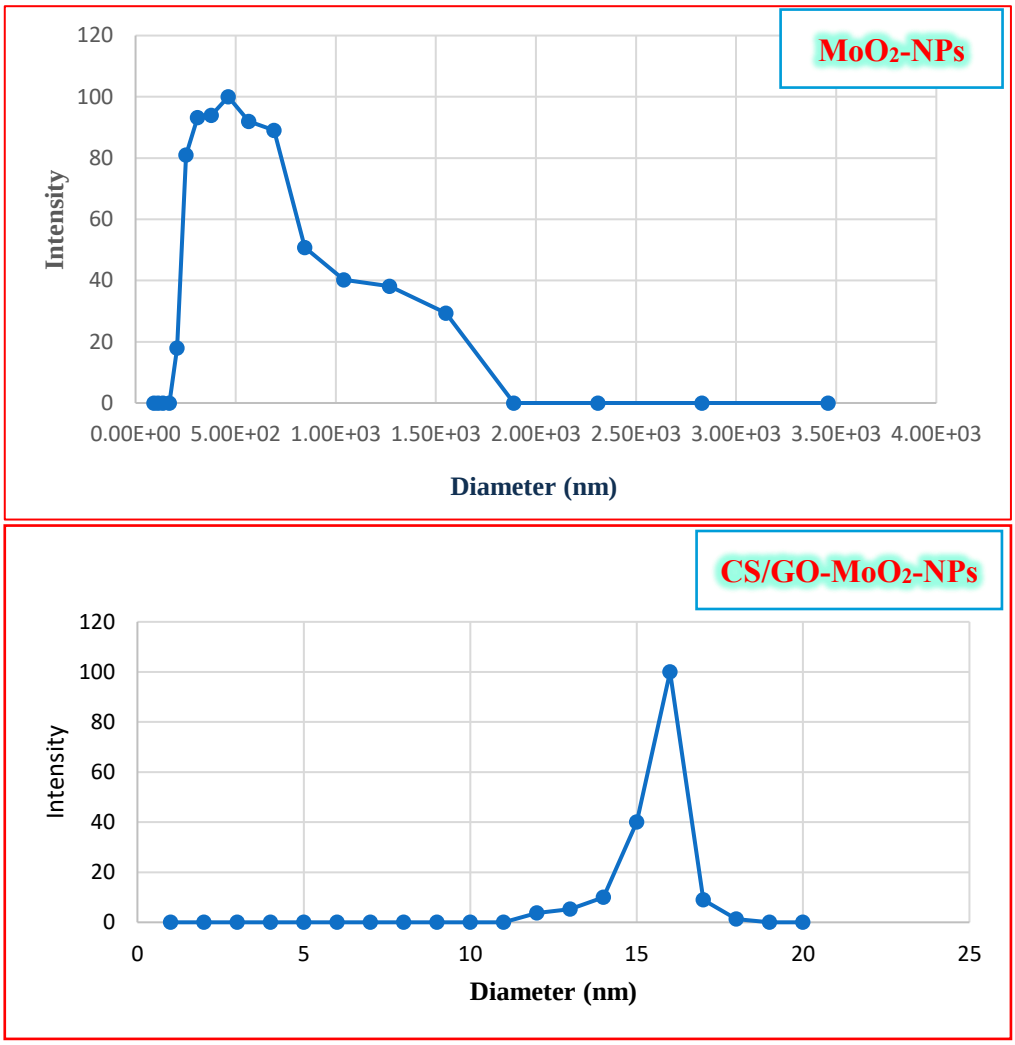

Figure 3.17 Dynamic Light Scattering of MoO_2-NPs, and CS/GO-MoO_2-Nps.

The obtained results show the difference in the particle size distribution that was determined by the DLS technique of MoO_2 on graphene and chitosan. The mean particle size of the MoO_2-NPs increased by increasing the chitosan polymer length, confirming their successful attachment, indicating a significant influence of formulation variables on the resultant particle size, indicating a homogenous distribution of MoO_2-NPs, and CS/GO-MoO_2-NPs.

3.3.6 Zeta Potential Analysis of MoO_2-NPs and CS/GO-MoO_2-Nps.

The obtained results of (ZPA) for the prepared materials are shown in Figure 3.18, the changes in the zeta potential during KCl titration.

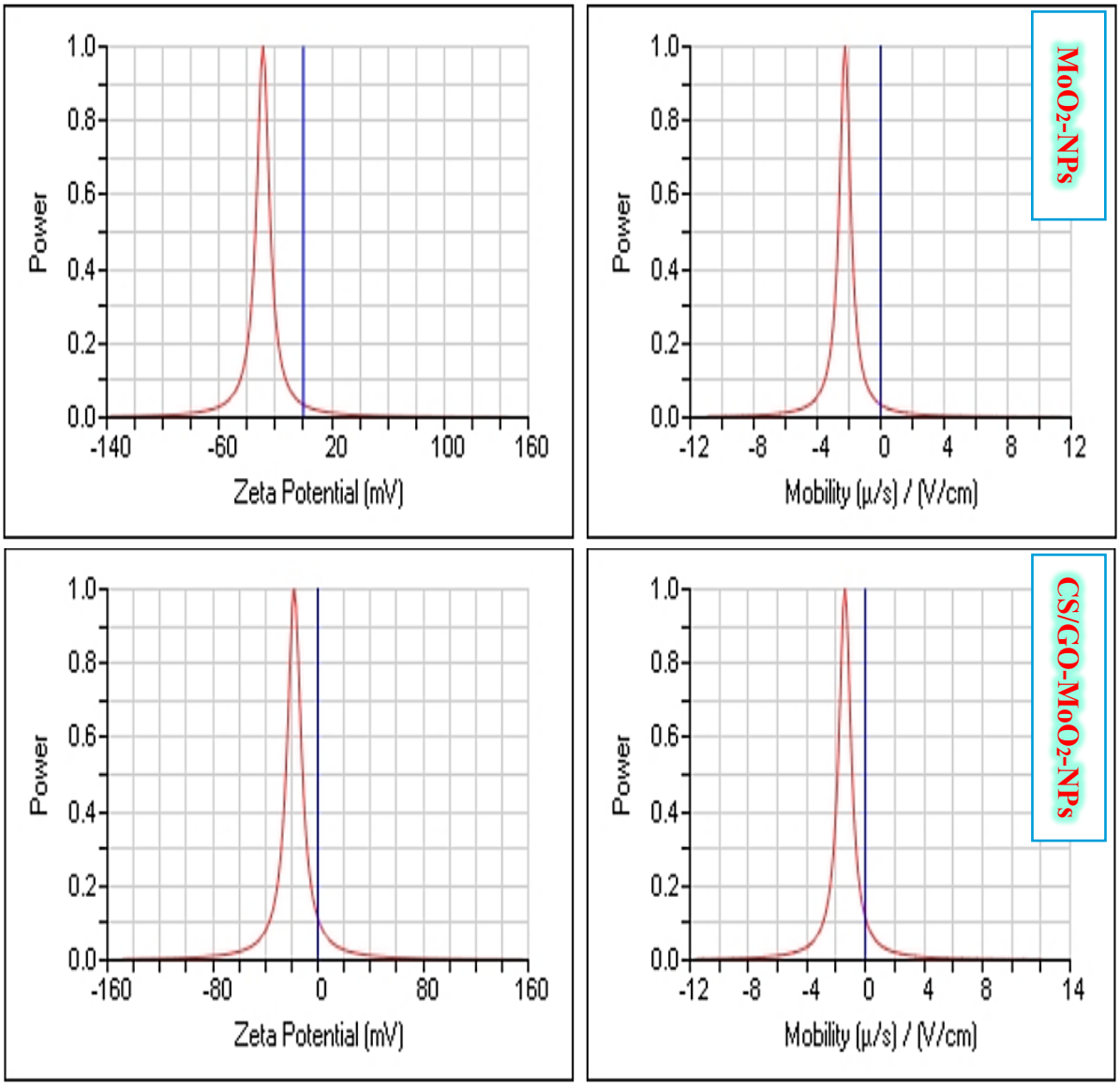

Figure 3.18 Zeta Potential Analysis of MoO_2-NPs, and CS/GO-MoO_2-NPs.

The charge or zeta potential of particles is determined by measuring their velocity while moving in an electrophoretic field. Particles and molecules with a zeta potential will migrate towards an electrode if a field is applied. Their speed is proportional to the field strength and their zeta potential. The phase analysis light scattering (PALS) technique was used in the tests. The whole measurement procedure is automated to simplify the measurement process.

The pH was 7.3, the zeta potential was -28.76 mV, and the diameter was roughly 50 nm. The addition of KCl resulted in a reduction in zeta potential as well as an increase in particle size. At pH 10.2, around the isoelectric point, the greatest size was discovered. In other words, knowing pH, adjusting it, and maintaining it at a stable value is required for MoO_2-NPs suspensions. Ions were adsorbed after adding graphene oxide and chitosan, causing a shift in the zeta potential Figure 3.18. The zeta potential increased when graphene oxide was adsorbed.

The zeta potential of chitosan adsorption, on the other hand, was moved to negative levels. With the use of additives, the zeta potential of the CS/GO-MoO_2-NP suspensions can be tuned and hence affect suspension stability [269]. Around neutral pH, adding a cationic surfactant enlarged the stable area (zeta potential above -17.91 mV). In strongly alkaline pH, the addition of anionic surfactant enlarged the stable zone. The addition of chitosan did not affect the stability of the MoO_2-NPs solution.

3.4 Adsorption Experiments

Initially, the results of the adsorption were entered in Langmuir and Freundlich equation. All the results did not obeyed Langmuir equations ($r<0.3$). While the application of Freundlich equation produce a high r-values (>0.7). Therefore, we consider only the Freundlich equation for all adsorption processes of the present study.

3.4.1 Adsorption of Follicle-Stimulating Hormone (FSH) on CS/GO-MoO_2-NPs

The adsorption isotherm of FSH on the surface of CS/GO-MoO_2-NPs surface is presented in Figure 3.19 and the logarithmic form in Figure 3.20.

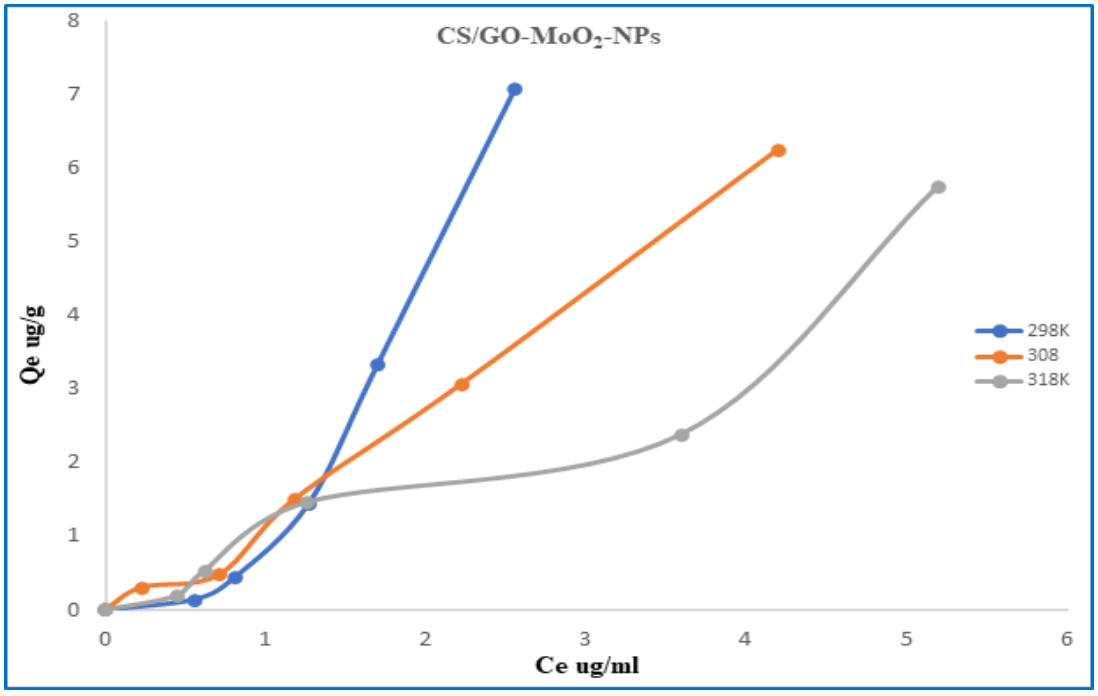

Figure 3.19 Adsorption Isotherms of FSH Hormone on the CS/GO-MoO_2-NPs Surface.

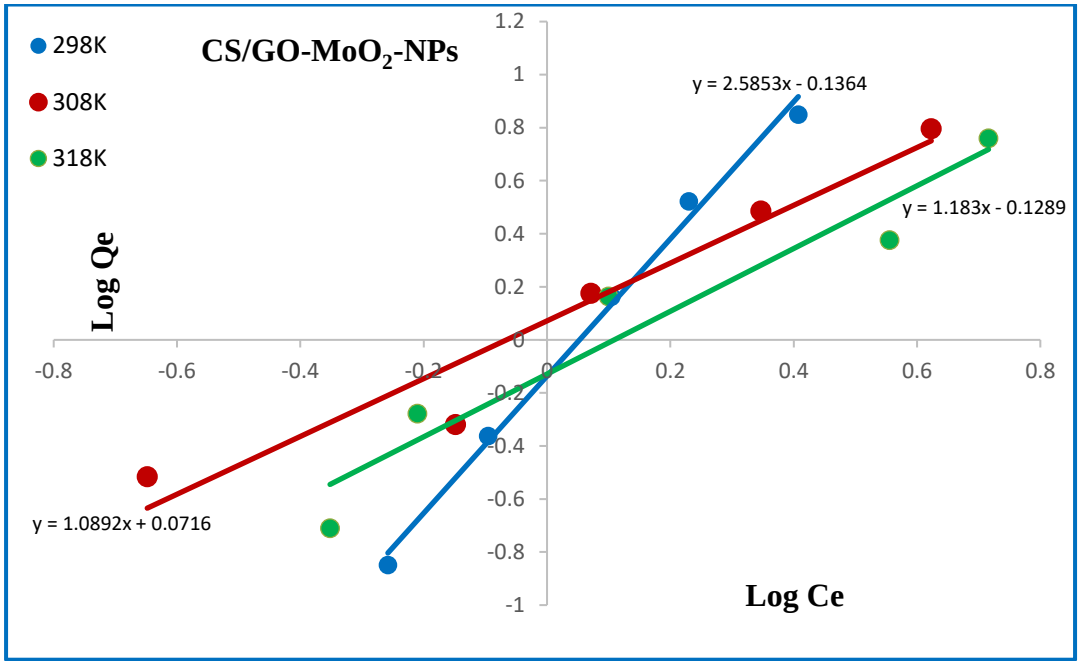

Figure 3.20 Freundlich Lines of the Adsorption of FSH Hormone on the CS/GO-MoO_2-NPs Surface.

This study tends to conjointly find a notable relation between FSH hormones that can be adsorbed on the surface of CS/GO-MoO_2-NPs spontaneously. Nanocomposite can adsorb relatively significant amounts of the FSH hormone 7.07 μg/g. Our results are consistent with those of a previous report, which established the main relationship between FSH hormones that can be adsorbed on the surface of nanoparticles (NPs) spontaneously and other factors such as thermodynamics of the adsorption process, adsorption isotherm, and difference of temperature. Furthermore, based on the literature, the results obtained from this research match results acquired by T.S.Najem [270], who found important variations between NPs used and the amount of the hormone. The raw data of the adsorption process are presented in Table 3.5.

Table 3.5 Adsorption of FSH on CS/GO-MoO_2-NPs

Temp ^{0}C	C_o FSH ng/ml	C_e FSH ng/ml	Qe ng/g	Log Ce	Log Qe
25 ^{0}C	0.835	0.552	0.142	-0.258	-0.849
	1.670	0.802	0.434	-0.096	-0.363
	4.175	1.272	1.452	0.104	0.162
	8.350	1.697	3.326	0.23	0.522
	16.700	2.556	7.072	0.407	0.850
35 ^{0}C	0.835	0.225	0.305	-0.648	-0.516
	1.670	0.710	0.480	-0.149	-0.319
	4.175	1.177	1.499	0.071	0.176
	8.350	2.221	3.064	0.347	0.486
	16.700	4.199	6.250	0.623	0.796
45 ^{0}C	0.835	0.445	0.195	-0.352	-0.71
	1.670	0.616	0.527	-0.210	-0.278
	4.175	1.257	1.459	0.099	0.164
	8.350	3.592	2.379	0.555	0.376
	16.700	5.200	5.750	0.716	0.760

To better description for the behavior of FSH adsorption on the surfaces of the NPs, adsorption isotherms were constructed for the adsorption of FSH on NPs, at 25, 35, and 45 °C (Figures 3.19, 3.20). The isotherms generally showed a slight increase in the quantity of adsorbed FSH (Qe) as FSH equilibrium concentration (Ce) increased. Thus, the adsorption tendency is very low at low FSH concentration and showed a rapid increase in Qe at higher FSH concentration.

Freundlich's adsorption isotherm was followed during the adsorption phase, showing that the nanocomposite surface was heterogeneous. Thermodynamic research discovered exothermic and spontaneous adsorption processes [271]. The overall findings indicated the ability of the composite nanoparticles to adsorb the FSH molecules effectively. Figure 3.21 shows the Vant's Hoff line of the adsorption of FSH on the CS/GO-MoO_2-NPs composites surface.

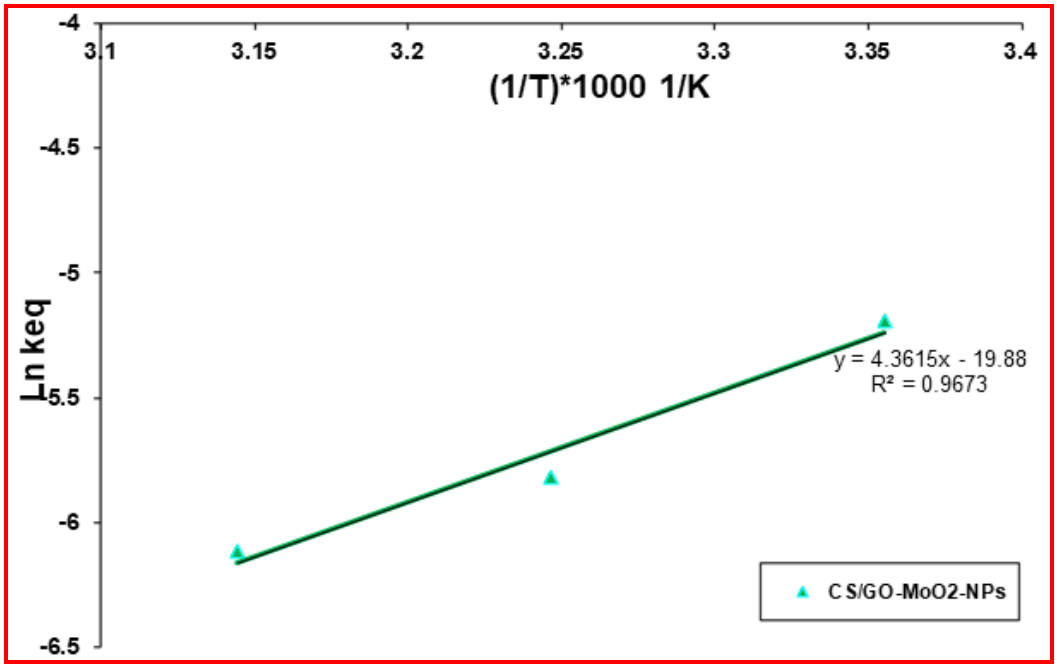

Figure 3.21 Vant's Hoff Lines of the Adsorption of FSH on the NPs Composites.

Thermodynamic functions of the adsorption of FSH on the NPs composites are presented in Table 3.6.

Table 3.6 Thermodynamic Functions of the Adsorption of FSH on the CS/GO-MoO_2-NPs Composites.

NPs	(1/T)*1000	Xm=Keq	ln Xm	Slope	ΔG° KJ/mol	ΔH° KJ/mol	ΔS° J/mol.k
CS/GO-MoO_2-NPs	3.356	0.005535	-5.197	4.835	12.875	-40.201	-178.107
	3.247	0.002977	-5.817				
	3.145	0.002212	-6.114				

The Vant-Hoff's lines for the adsorption of FSH on NPs are presented in Figure 3.21. The results of the thermodynamic parameters are presented in Table 3.6. Overall, protein stability depends on the balance between these enthalpy and entropic changes. The hydration of interior non-polar

groups causes minor denaturation in proteins because the energy of hydration is enhanced (that is, the entropic cost of denaturation, due to the structuring of the water molecules around the exposed groups, is reduced) [272]. Another possibility is that as the temperature rises from a low value, the hydrophobic contacts increase. At very low temperatures, the extended polypeptide chain folds up to form an active globular protein, which releases water molecules into the surrounding environment.

3.4.2 Adsorption of Luteinizing Hormone (LH) on CS/GO-MoO_2-NPs

Figure 3.22 represents the adsorption of LH hormone and the application of Freundlich lines of the adsorption of LH hormone on the CS/GO-MoO_2-NPs surface.

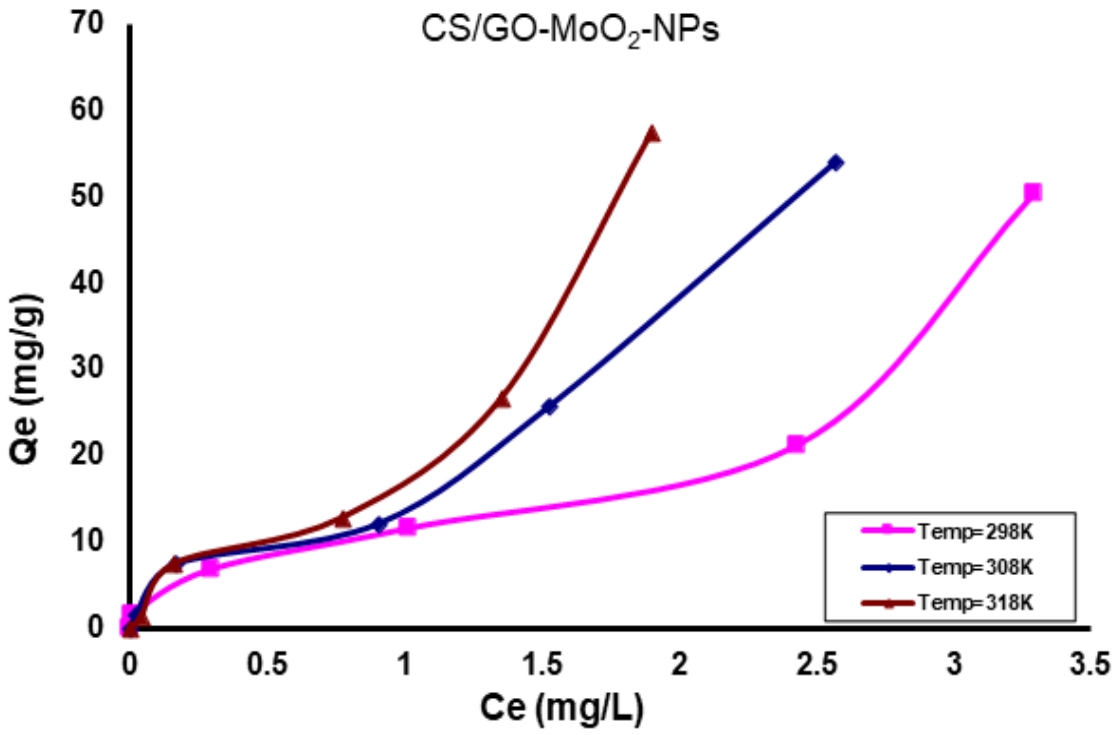

Figure 3.22 Adsorption Isotherms of LH Hormone on the CS/GO-MoO_2-NPs Surface.

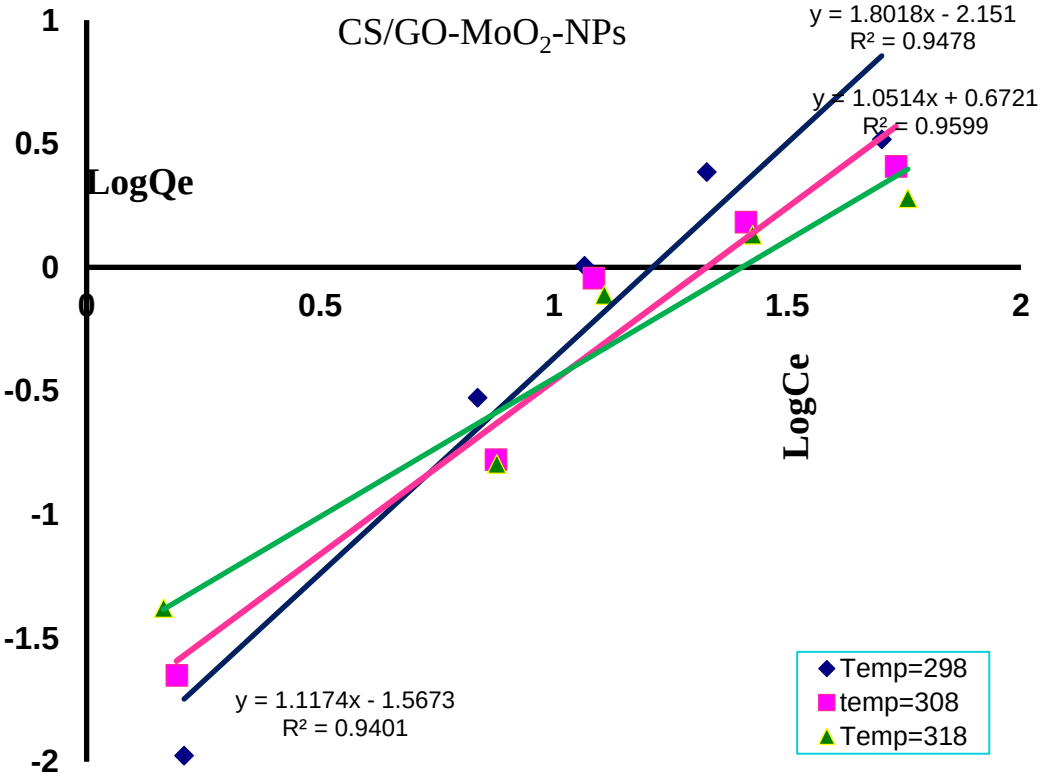

Figure 3.23 Freundlich Lines of the Adsorption of LH Hormone on the CS/GO-MoO_2-NPs Surface.

Table 3.7 Adsorption of LH on CS/GO-MoO_2-NPs

Temp ^{0}C	Co ng/ml	Ce ng/ml	Log Ce	Co-Ce	Q ng/g	Log Q	Ce/Q
25 ^{0}C	0.000	0.000	0.000	0.000	0.000	0.000	0.000
	0.334	0.011	-1.975	0.3234	1.617	0.20871	0.007
	1.67	0.297	-0.528	1.373	6.867	0.837	0.043
	3.34	1.014	0.006	2.326	11.630	1.066	0.087
	6.68	2.429	0.385	4.251	21.256	1.328	0.114
	13.36	3.29	0.517	10.07	50.35	1.702	0.065
35 ^{0}C	0.000	0.000	0.000	0.000	0.000	0.000	0.000
	0.334	0.022	-1.650	0.312	1.558	0.193	0.014
	1.67	0.167	-0.777	1.503	7.515	0.876	0.022
	3.34	0.905	-0.04345	2.435	12.176	1.086	0.074
	6.68	1.526	0.184	5.154	25.770	1.411	0.059
	13.36	2.565	0.409	10.795	53.973	1.732	0.048
45 ^{0}C	0.000	0.000	0.000	0.000	0.000	0.000	0.000
	0.334	0.042	-1.378	0.292	1.461	0.165	0.029
	1.67	0.16	-0.796	1.51	7.55	0.878	0.021
	3.34	0.772	-0.112	2.568	12.840	1.109	0.060
	6.68	1.354	0.132	5.326	26.630	1.425	0.051
	13.36	1.902	0.279	11.458	57.291	1.758	0.033

Figure 3.22 shows the adsorption isotherm of LH on the surface of the CS/GO-MoO_2-NPs. While Figure 3.23 introduces the Freundlich equation in its linear form for the adsorption of the hormones on the NPs surface. The adsorption of the hormone on the surface of CS/GO-MoO_2-NPs showed that the maximum quantity adsorbed on the surface of NPs at 45 °C is as follows LH (57.29 μg/g). This result indicates a proper capability of CS/GO-MoO_2-NPs to adsorb these hormones efficiently at their relatively very low concentration. The reason LH showed higher capability for adsorption is the molecular weight or the number of amino acids. The alpha subunit is identical in all hormones. At the same time, the beta chain contains (120) amino acids in LH, 111 [273]. The LH molecule appears to have more domains or groups capable of interacting with the surface of NPs than other hormones. Therefore, LH is the most adsorbable protein compared with the other two hormones [270].

The lines of the Freundlich equation demonstrated that the adsorption equation could be used to predict hormone adsorption on the surface of CS/GO-MoO_2-NPs. The applicability of the Freundlich equation indicates a surface's heterogeneity [274]. Freundlich isotherms imply that non-covalent protein-NPs conjugation produces heterogeneity by exerting various forces on the surface or the molecules of hormones. Adsorption properties of the LH hormone on the surface of CS/GO-MoO_2-NPs. The results showed that the amount of adsorption slightly increased with increasing temperature. The plotting of Vant-Hoff's equation for the adsorption process is presented in Figure 3.24. The results of the thermodynamic parameters are presented in Table 3.8.

Table 3.8 Thermodynamic Functions of the Adsorption of LH on the CS/GO-MoO_2-NPs Composites

NPs	(1/T)*1000	Xm=Keq	ln Xm	Slope	ΔG° KJ/mol	ΔH° KJ/mol	ΔS° J/mol.k
CS/GO-MoO_2-NPs	3.356	76.51976	4.337549	-3.205	-10.747	26.647	125.483
	3.247	105.1883	4.655752				
	3.145	150.6071	5.014674				

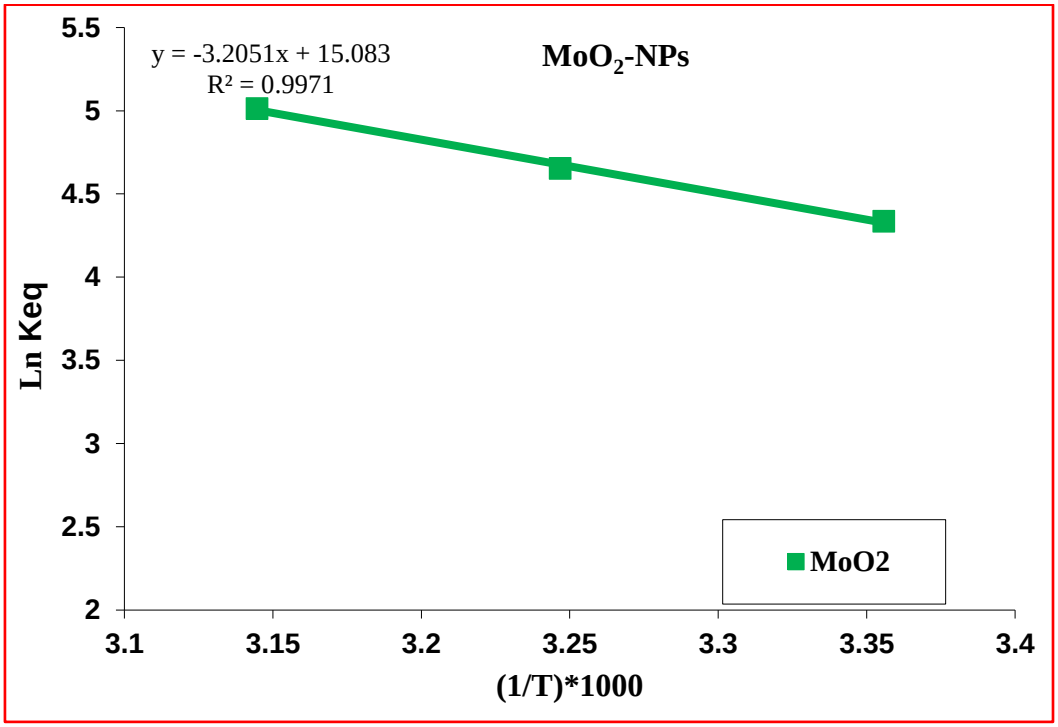

Figure 3.24 Vant's Hoff Lines of the Adsorption of LH on the NPs Composites.

The endothermic nature of the adsorption process is indicated by the positive value of ΔH° (26.647 kJ/mol). The adsorption of hormone over CS/GO-MoO_2-NPs on a surface may cause protein conformational changes. The degree of conformational alterations was calculated using a combination of a protein's native stability, hydrophobicity and charges, and the sorbent surface. Conformational entropy changes can drive the

adsorption of MoO_2-NPs, especially if the adsorption is endothermic. According to earlier research, the adsorption capacity of MoO_2-NPs increased as the temperature was rose, indicating an endothermic reaction. Table 3.8 shows the values of changes in free energy and entropy.

Thermodynamic values show that the CS/GO-MoO_2-NPs complexes involved electrostatic interaction as well as other non-covalent forces such as hydrophobic, hydrogen bonding, and - interaction, which were acquired from the surface of the functional groups of the NPs [275].

The adsorption energy was consistent with the adsorption energy determined from the sum of the electrostatic and Van der Waals forces, as previously stated. The stability of the adsorption system CS/GO-MoO_2-NPs depended on the equilibrium between the entropy and enthalpy change on adsorption [276].

3.5 Characteristics of the Prepared Nanoparticles MnO_2-NPs and CS/GO- MnO_2-Nps

The characterization of MnO_2-NPs and CS/GO-MnO_2-Nps was studied using different analytical instruments such as XRD, SEM, Energy dispersive spectroscopy (EDS), FT-IR, UV-Visible spectroscopy, DLS, and Zeta potential analysis.

3.5.1 X-rays Diffraction (XRD) of MnO_2-NPs and CS/GO-MnO_2-Nps

The crystal structure of MnO_2-NPs nanocomposites has been examined using XRD over the 2θ angle range from 10° to 80°. Figure 3.25 shows the XRD pattern of the prepared powder.

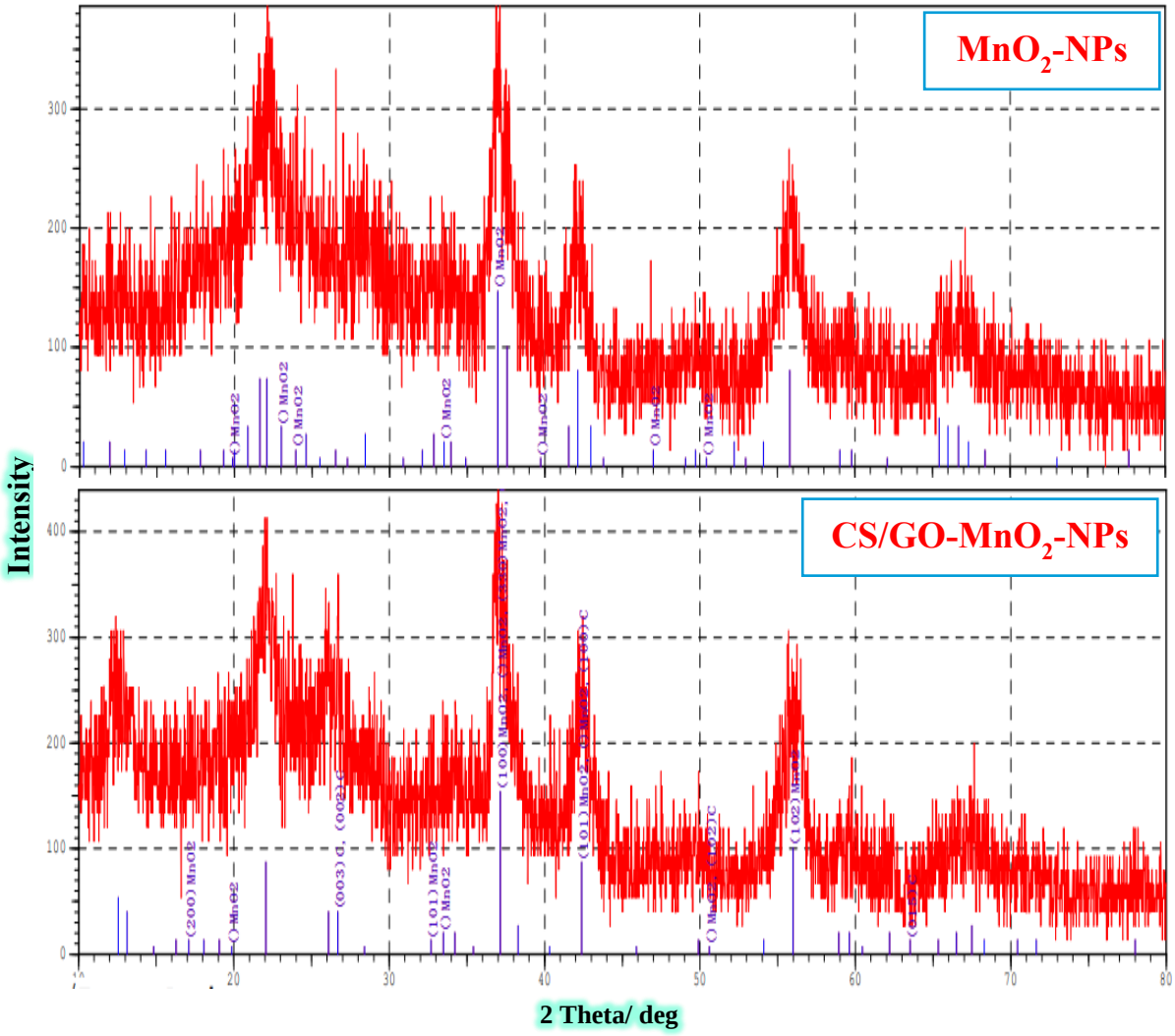

Figure 3.25 XRD Patterns of MnO_2-NPs and CS/GO-MnO_2-NPs.

The sharp diffraction peaks of MnO_2-NPs have been analyzed at 2θ =36.97°, 37.57°, 30.70, 42.12°, 55.79°, 66.68°, and 67.31°, consistent with MnO_2-NPs standard pattern (JCPDS: 44 - 0141). MnO_2 is known to come in a variety of polymorphs (i.e., exist in the various crystal structure) α-, β-, γ-, δ-, ε- and λ-types and so forth, each form differs from the other in the arrangement of the basic structural unit of ([MnO_6] octahedron).

MnO_2 may exist as a tunnel structure similar to chain such as α-, β-, and γ-types, layered or sheet structure like - MnO_2, and as a 3D structure like λ-type, according to these octahedron links. In their crystal structure, the phases α- MnO_2, β- MnO_2, and γ- MnO_2 have one-dimensional (1D); the phase δ-MnO_2 is a 2D-layered compound, the phase γ-MnO_2 has a 3D spinel structure [277].

The results obtained from the analyses of the XRD pattern displayed that the average size of MnO_2 NPs calculated by Debye-Scherer was about 28.2 nm shown in Figure 3.25 indicating its semi-crystalline nature. It shows the presence of 37.1˚, which is the highest peak belonging to the α-MnO_2 phase according to the standard (JCPDS: 44 - 0141), making it the predominant phase [277].

3.5.2 Scanning Electron Microscopy (SEM) of MnO_2-NPs and CS/GO- MnO_2-Nps.

A scanning electron microscope was used to deduce the particle size and morphology of the synthesized manganese dioxide nanoparticles as in Figure 3.26.

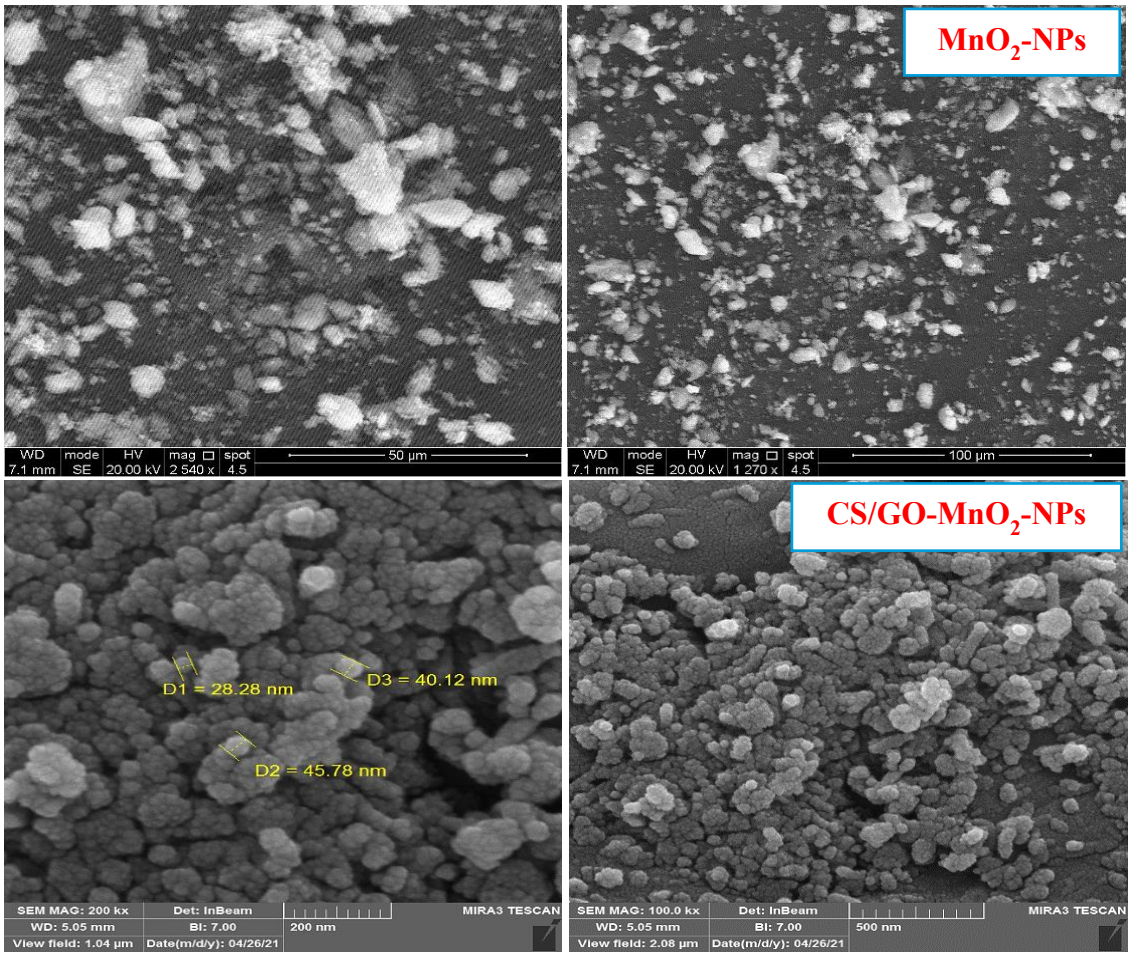

Figure 3.26 SEM Images of MnO_2-NPs, CS/GO-MnO_2-NPs.

Figure (3.26) shows that graphene crystalline nanoparticles almost cover the surface of MnO_2 and its dimensions are on the nano scale. Manganese dioxide (MnO_2) has various crystal structures because of the wide variety of corners and/or edges sharing arrangements of building block units [277]. Figure 3.26 shows SEM images with different magnifications, and the particles in the samples were compactly arranged and were almost spherical. The size of the synthesized manganese dioxide nanoparticles was in the range of (28.2 - 40.1) nm.

3.5.3 Energy Dispersive X-rays Spectroscopy (EDX) of MnO_2-NPs and CS/GO- MnO_2-Nps.

Figure 3.27 shows the elemental analysis of MnO_2 nanoparticles.

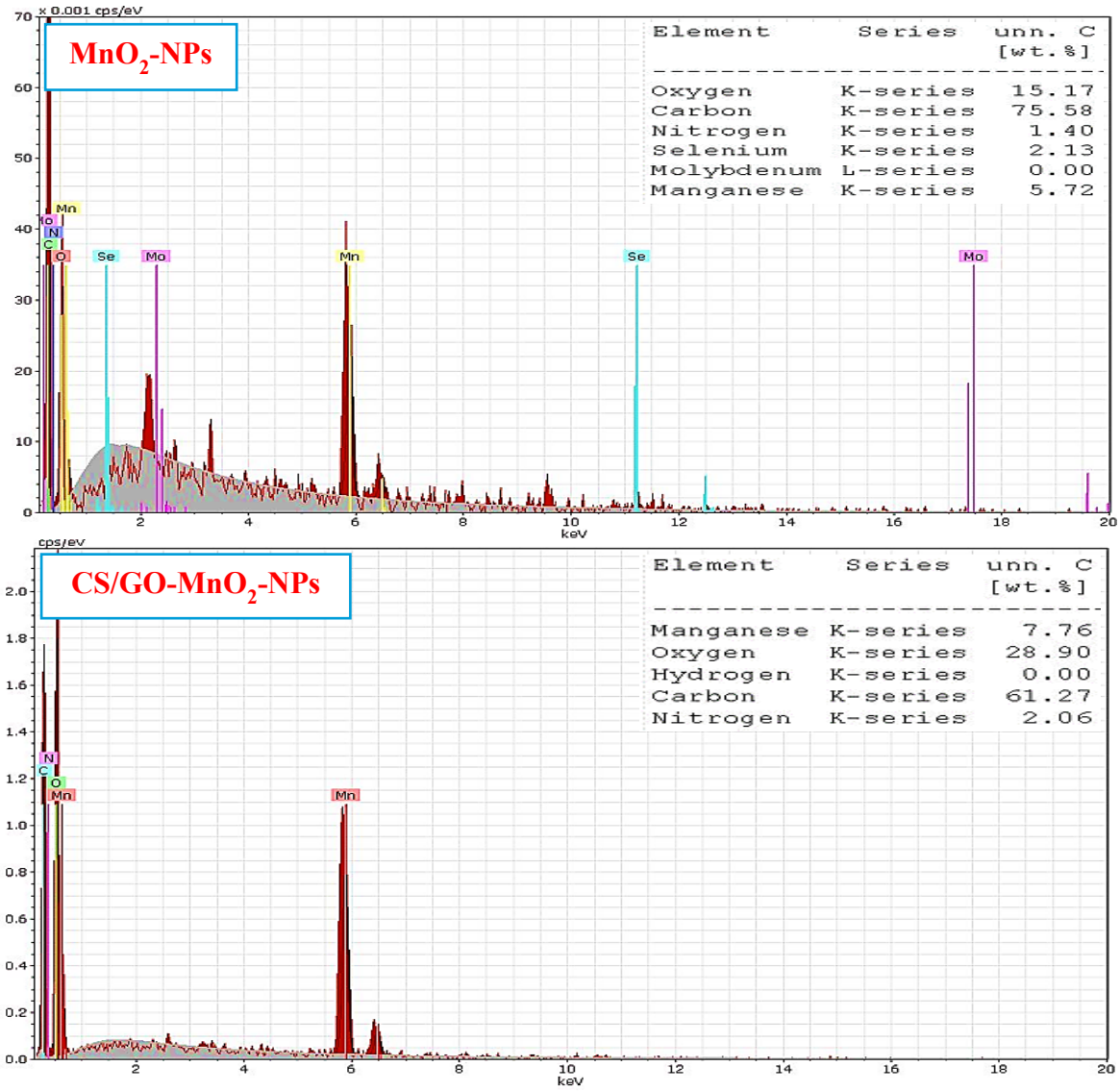

Figure 3.27 EDX Spectra of MnO_2-NPs, and CS/GO-MnO_2-NPs.

One analytical method for structural analysis of the material is energy-dispersive X-rays spectroscopy (EDX). This figure shows oxygen and Mn elements in the synthesized sample. It should be observed that the present atoms were distributed similarly to C, N, O, and Mn atoms in the produced MnO_2-NPs. The data from EDX revealed the percentage of manganese is 7.76%, and oxygen equaled 28.90%, confirming the existence of MnO_2-NPs.

3.5.4 Fourier Transform Infrared Spectrophotometer (FTIR) of MnO_2-NPs and CS/GO- MnO_2-Nps.

The FTIR spectroscopy was carried out to ascertain the purity and nature of manganese dioxide metal nanoparticles synthesized by the co-precipitation method, as shown in Figure 3.28.

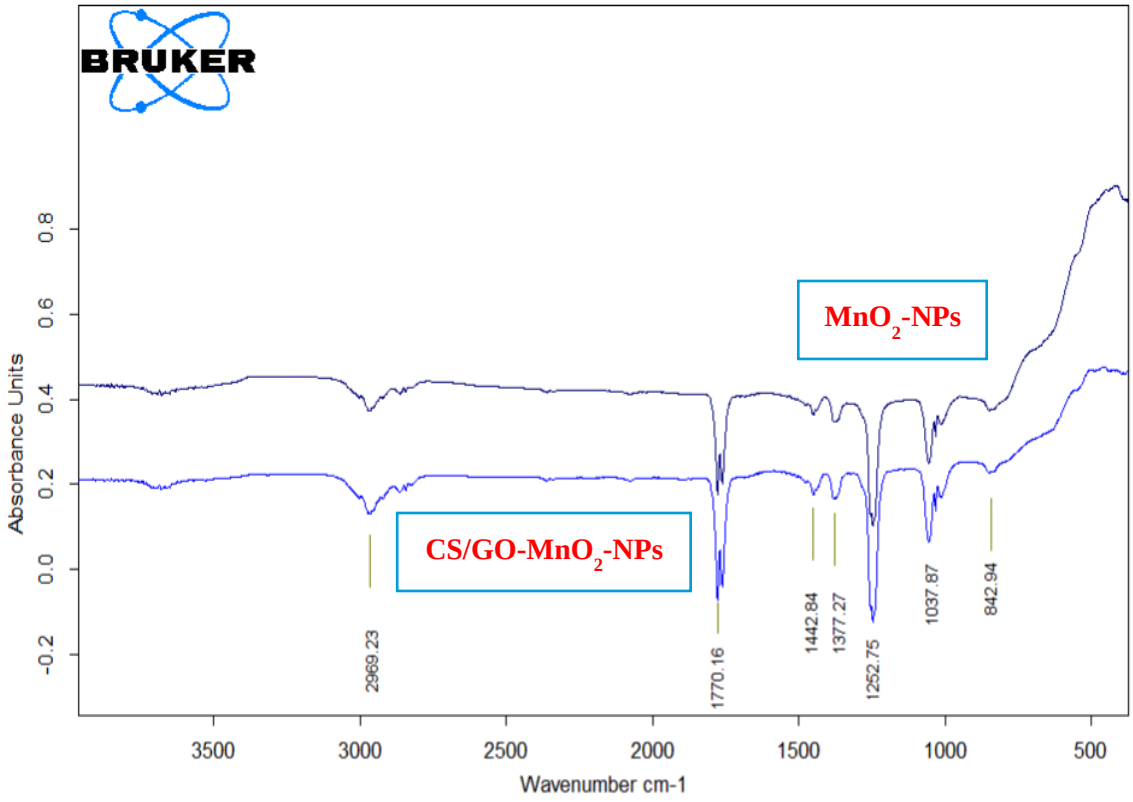

Figure 3.28 FTIR Spectra of MnO_2-NPs, and CS/GO-MnO_2-NPs.

The purity and nature of manganese dioxide metal nanoparticles produced by the co-precipitation technique were determined using FTIR spectroscopy. This method is based on high-precision and sensitivity interference. Figure 3.28 depicts the functional group present in the produced manganese dioxide nanoparticles. The two absorption bands at (588.31 and 432.07) cm^{-1} belong to the stretching collision of O–Mn–O, which denotes the presence of MnO_2, and are ascribed to Mn-O vibrations in the range of (400-800) cm^{-1}.

The broad bands of absorptions in the range of 4000 to 3000 cm^{-1} are attributed to both H–O–H stretching collision and hydroxyl groups, while the peak at 1641 cm-1 was attributed to bending collision of adsorbed water H_2O molecule, and the peaks at 3342, 1641, 1381, 1054, and 559 are attributed to the presence of O-H, C=O, C-C, Mn-C, Mn-O, etc [278].

3.5.5 Dynamic Light Scattering of MnO_2-NPs and CS/GO-MnO_2-Nps.

Figure 3.29 shows the measurement of the particles size distribution of MnO_2-NPs nanocomposite.

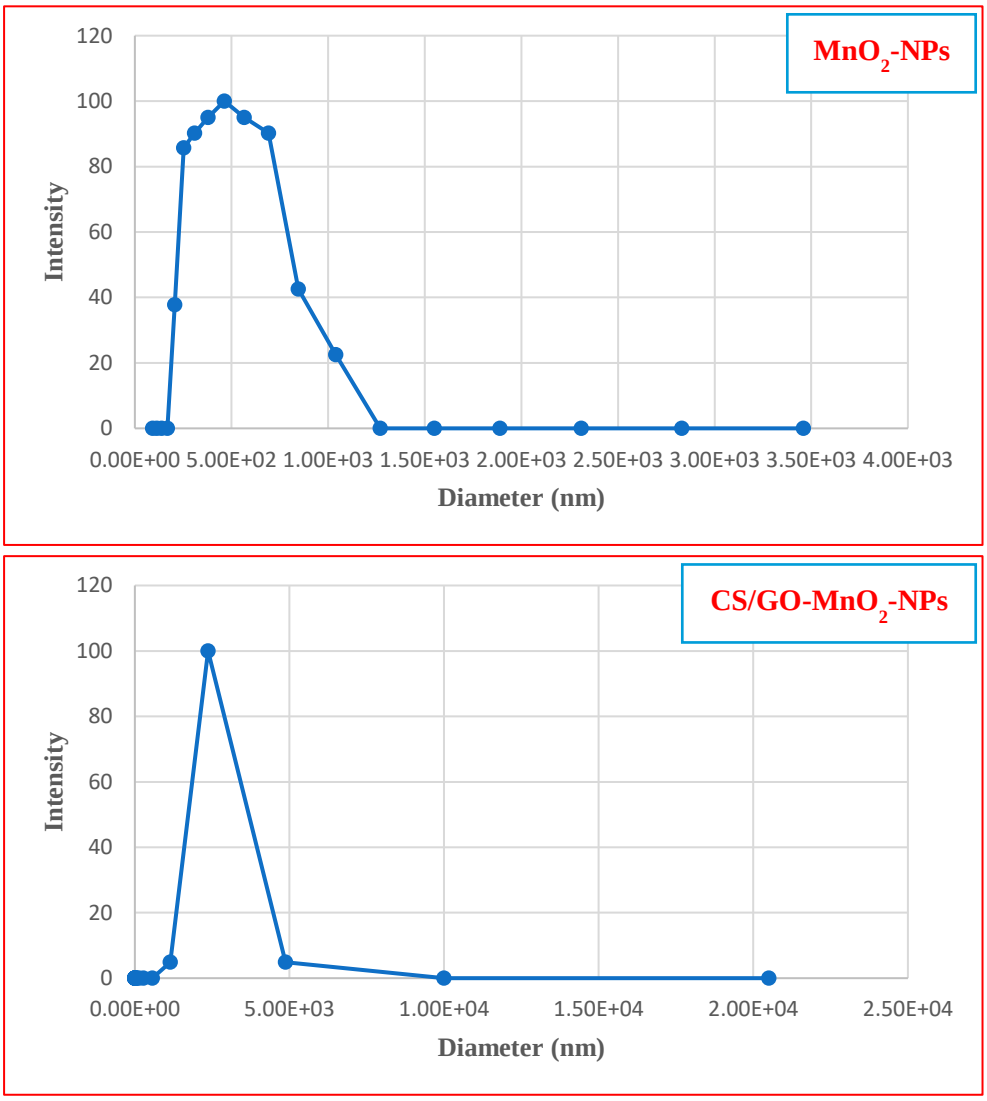

Figure 3.29 Dynamic Light Scattering of MnO_2-NPs, and CS/GO-MnO_2-NPs.

The Particle size distribution histogram was measured from DLS (dynamic light scattering). Figure 3.29 showed the sharp peak at 28.2 nm that indicated the size particle distribution of MnO_2-NPs. When graphene oxide and chitosan are used as additives, nanoparticles bigger are obtained, but they are less aggregated. The particle size distribution is narrower for graphene and chitosan than that obtained from manganese dioxide. The additives influence the particle size and the particle size distribution due to their adsorption on the surface of MnO_2 nanoparticles, which inhibit the aggregation of manganese oxide nanoparticles. This would mean that graphene oxide is the strongest adsorbed additive on the surface.

3.5.6 Zeta Potential Analysis of MnO_2-NPs and CS/GO-MnO_2-Nps.

The zeta potential values of MnO_2-NPs dispersions as a function of their pH are presented in Figure 3.30.

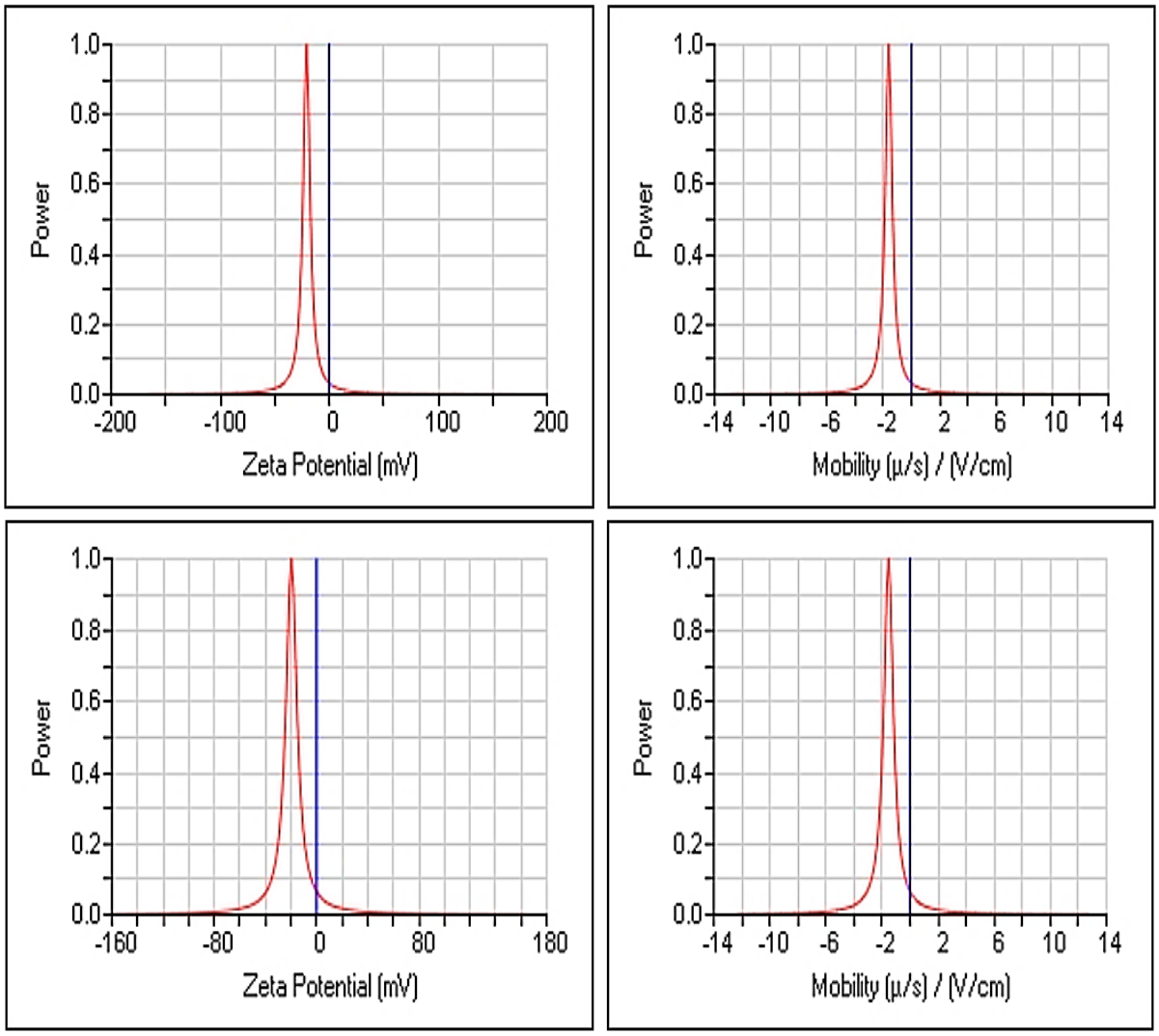

Figure 3.30 Zeta Potential Analysis of MnO_2-NPs, and CS/GO-MnO_2-NPs.

The electric potential formed by the presence of a charge on the particle surface, which can be positive or negative in polarity depending on the chemistry of the particles, is known as zeta potential. The degree of repulsion between similarly charged particles in a formulation is measured by the zeta potential.

Particle aggregation during storage is prevented by repulsive forces. As a result, a formulation's zeta potential indicates its likely physical stability [279]. Figure 3.30 shows the changes in the zeta potential. In addition, particle size. The pH was 7.3, the value of the zeta potential value was -19.67mV to -20.73, and it does seem to depend on the pH value. The zeta potential increases with decreasing value of pH. The dependence of the zeta potential of the dispersion of MnO_2-NPs on the pH value as in Figure 3.30 is similar to all the applied synthesis methods. The zeta potential is positive for pH values less than 5.5 and negative when the pH increases with the isoelectric point around pH = 5.6. The zeta-potential depends on the interaction between water ions and the nanoparticles [269].

3.6 Adsorption Experiments

Initially, the results of the adsorption were entered in Langmuir and Freundlich equation. All the results did not obeyed Langmuir equations ($r<0.3$). While the application of Freundlich equation produce a high r-values (>0.7). Therefore, we consider only the Freundlich equation for all adsorption processes of the present study.

3.6.1 Adsorption of FSH on CS/GO-MnO_2-NPs

FSH adsorption isotherms on the surface of NPs are depicted in Figure 3.31. For the adsorption of hormones on the surface of NPs, Figure 3.32 shows the Freundlich equation in its linear form.

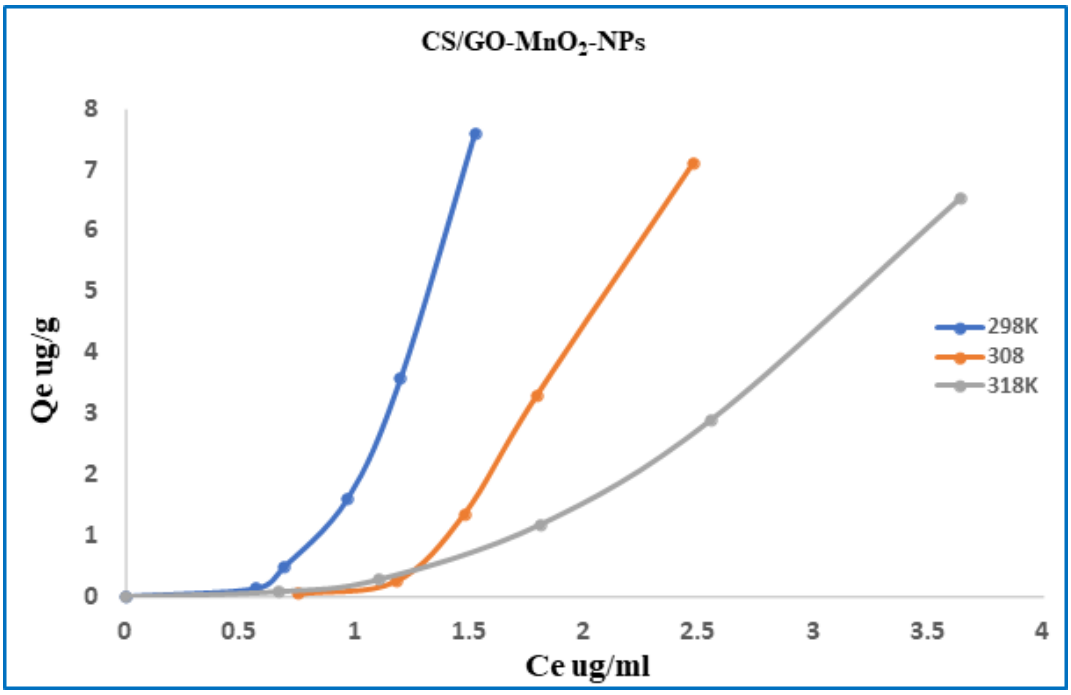

Figure 3.31 Adsorption Isotherms of FSH Hormone on the CS/GO-MnO_2-NPs Surface.

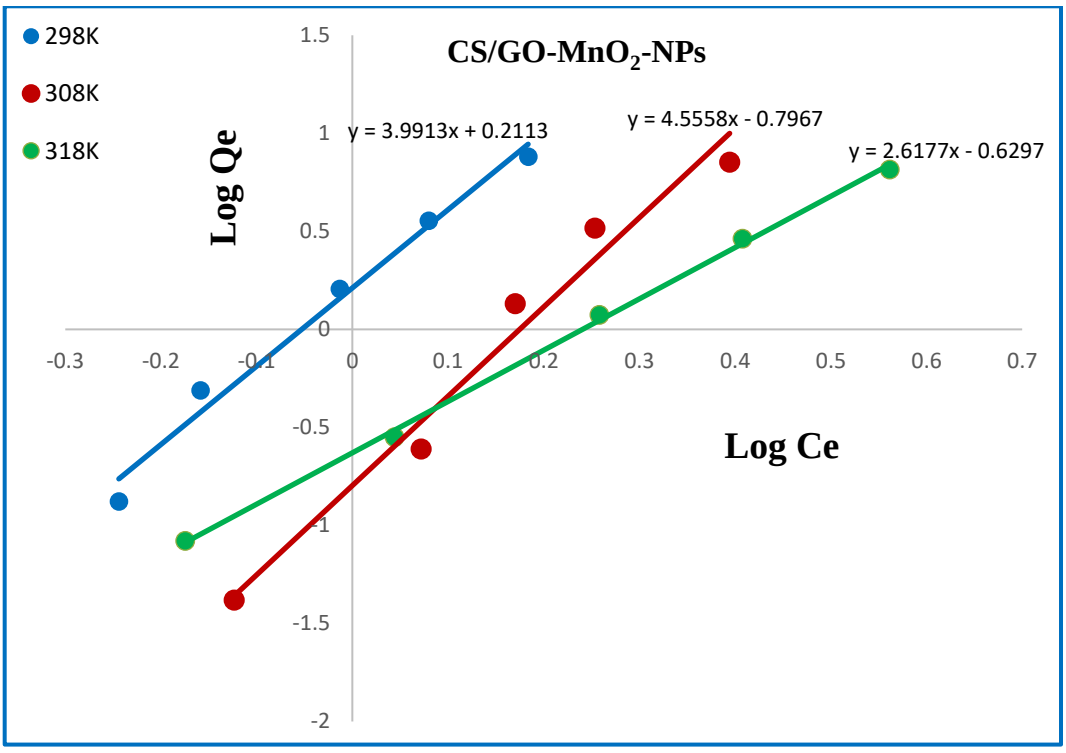

Figure 3.32 Freundlich Lines of the Adsorption of FSH Hormone on the CS/GO-MnO_2-NPs Surface.

Table 3.9 Adsorption of FSH on CS/GO-MnO_2-NPs

Temp ^0C	C_o FSH ng/ml	C_e FSH ng/ml	Qe ng/g	Log Ce	Log Qe
25 ^0C	0.835	0.57	0.132	-0.244	-0.878
	1.670	0.694	0.488	-0.159	-0.311
	4.175	0.97	1.602	-0.013	0.205
	8.350	1.202	3.574	0.080	0.553
	16.700	1.527	7.587	0.184	0.880
35 ^0C	0.835	0.752	0.042	-0.124	-1.382
	1.670	1.179	0.245	0.072	-0.610
	4.175	1.479	1.348	0.170	0.130
	8.350	1.793	3.279	0.254	0.516
	16.700	2.479	7.110	0.394	0.852
45 ^0C	0.835	0.668	0.083	-0.175	-1.079
	1.670	1.107	0.282	0.044	-0.550
	4.175	1.811	1.182	0.258	0.073
	8.350	2.556	2.897	0.407	0.462
	16.700	3.643	6.529	0.561	0.815

To clarify the behavior of FSH adsorption on the surface of the CS/GO-MnO_2-NPs, adsorption isotherms were constructed for the adsorption of FSH on NPs, at 25, 35, and 45 °C (Figures 3-31 and 3-32). Furthermore, the adsorption-isotherm shape changed at 45 °C. Hormonal effects may play an important role in the interaction with NPs, to determine if MnO_2-NPs exposure leads to minor changes, as the effect of CS/GO-MnO_2-NPs on FSH concentration significantly increased compared with controls in Figure 3.31. However, higher doses of CS/GO-MnO_2-NPs significantly increased serum FSH concentrations compared to MnO_2-NPs. The increase in protein concentration in large quantities and the increases in the amount of protein adsorbed onto the surface, which indicates a structural change within a protein molecule because of adsorption or desorption, may occur. These alterations could be the result of a strong adsorption driving force. As Martinez et al. (2019) discovered in a recent study, protein adsorption on surfaces may include the formation

of covalent chemical interactions. The adsorption of protein on different surfaces indicated the presence of different and distinct preferred binding regions on the surface active sites.

To elucidate the homogeneity of surface forces and the interaction behavior of the CS/GO-MnO_2-NPs surface with FSH, adsorption isotherms were constructed using Freundlich models for the adsorption of FSH on NPs to interpret the adsorption data of the investigated systems as shown in (Figure 3.32). The lines of the Freundlich equation demonstrated that the adsorption equation may be used to predict hormone adsorption on the surface of CS/GO-MnO_2-NPs. The applicability of the Freundlich equation indicates the heterogeneity of a surface [274]. Freundlich isotherms imply different forces on the surface or hormones to produce heterogeneity by non-covalent protein-NPs conjugation.

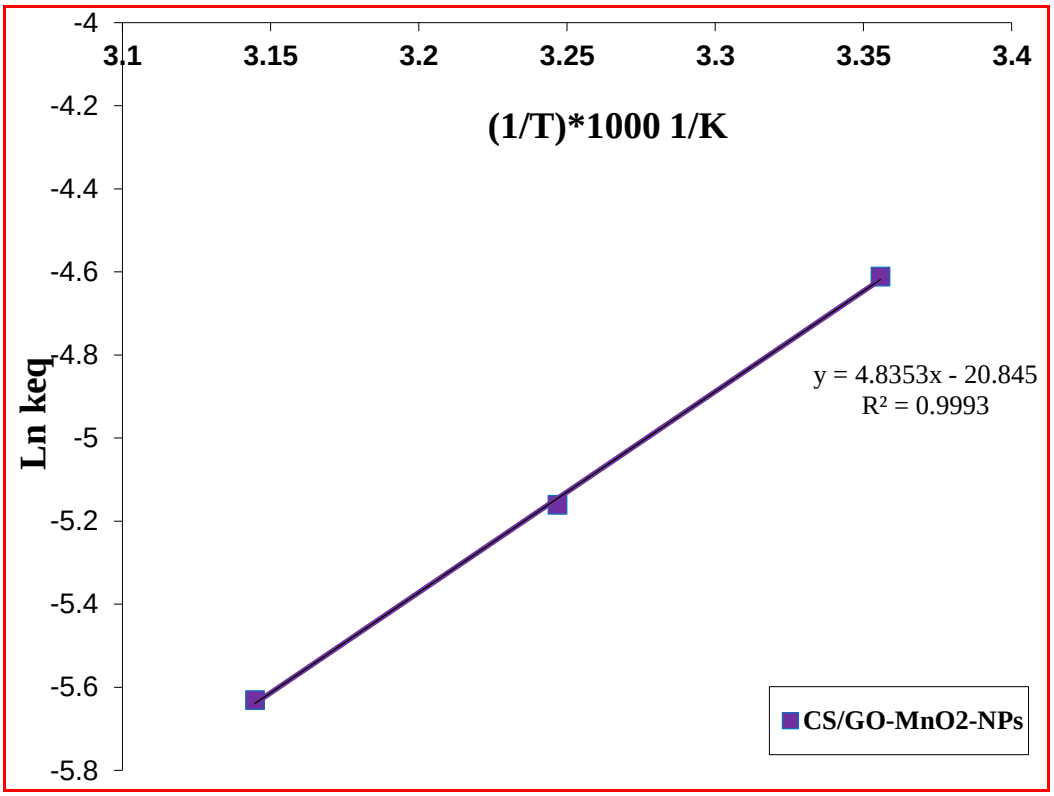

Figure 3.33 Vant's Hoff Lines of the Adsorption of FSH on the NPs Composites.

Table 3.10 Thermodynamic Functions of the Adsorption of FSH on the CS/GO-MnO_2-NPs Composites.

NPs	(1/T)*1000	Xm=Keq	ln Xm	Slope	ΔG° KJ/mol	ΔH° KJ/mol	ΔS° J/mol.k
CS/GO-MnO_2-NPs	3.356	0.00994	-4.611	4.362	11.425	-36.262	-160.021
	3.247	0.005736	-5.161				
	3.145	0.003584	-5.631				

Figure 3.33 represents Vant Hoff's equation for the adsorption of FSH hormone on the surface of CS/GO-MnO_2-NPs at (25, 35, and 45 ^{0}C). While Table 3.10 revealed the thermodynamic parameters of the adsorption of the hormones on the NPs surface. In general, the manganese oxide nanoparticles modified have attracted significant interest as promising controlled release protein delivery because of their ability to minimize the aggregation and irreversible denaturation of proteins. The obtained data demonstrate that the FSH encapsulation into the NPs is a gradual process driven by the hydrophobic interactions between the hydrophobic patch of FSH and the hydrophobic nanodomains of the nanoparticles.

Table 3.10 represents the thermodynamic parameters of FSH hormone adsorption on the surface of NPs. Adsorption is an exothermic and spontaneous process. The drop in entropy shows that the adsorption system's chaos has lessened. Protein molecules lost their ability to freely move in the solution and were organized on the surface of the NPs by various forces. The driving force for adsorption can be considerably influenced by conformational variations in the protein [280]. As temperature rises, the ΔH° of the polar group transfer from the protein inner to the outside section in contact with water molecules tends to be

negative due to increased molecular interactions that cause a negative ΔH° [281]. Above 25 ^{0}C, the ΔH° of non-polar group transfer from the protein interior into water is positive, overlapping the repulsion. At ambient temperature, the entropies of hydration of both non-polar and polar groups are negative indicating that both create order in the aqueous environment. However, these entropies differ in how they change with increasing temperature [282].

The stability of the native state depends on the balance between favorable entropy and unfavorable enthalpy change of adsorption. Unfavorable enthalpy changes predominate in weak surface attractions, which stabilize proteins. Conversely, unfavorable enthalpy effects predominate at the increased surface attraction, destabilizing the native state.

3.6.2 Adsorption of Luteinizing Hormone (LH) on CS/GO-MnO_2-NPs

Figure 3.34 shows the spontaneous adsorption of LH hormone on the surface of CS/GO-MnO_2-NPs and the applicability of the Freundlich equation.

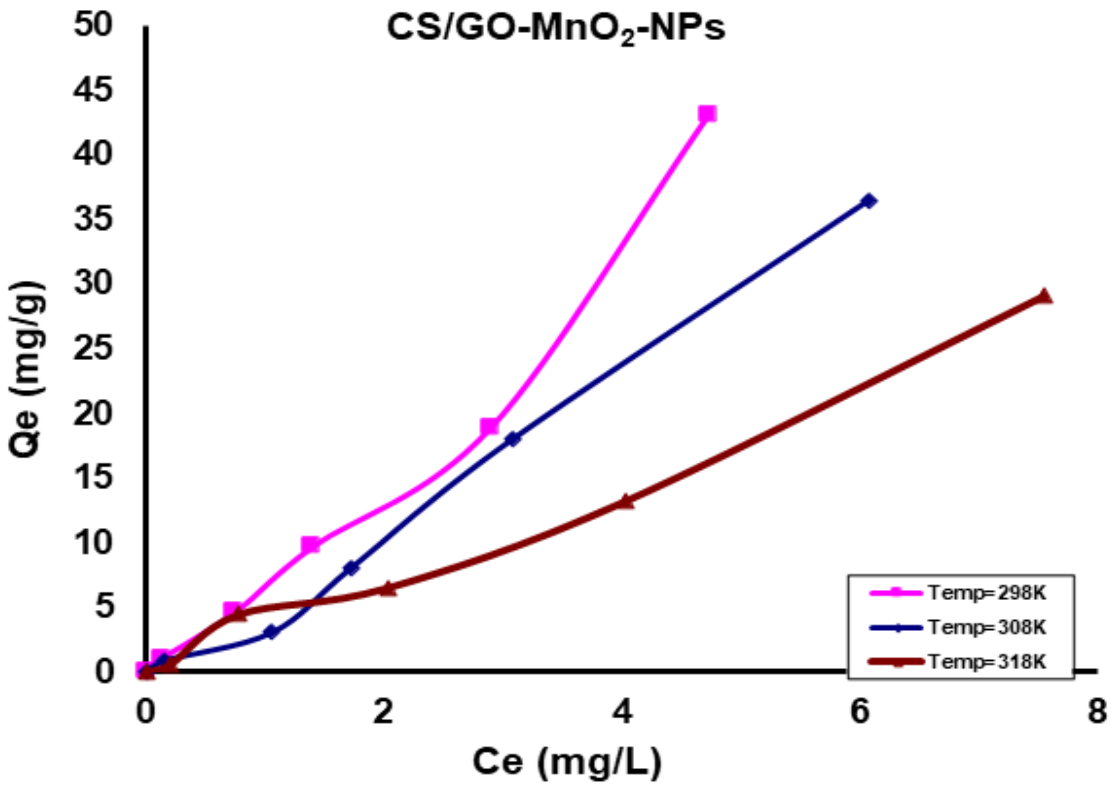

Figure 3.34 Adsorption Isotherms of LH Hormone on the CS/GO-MnO_2-NPs Surface.

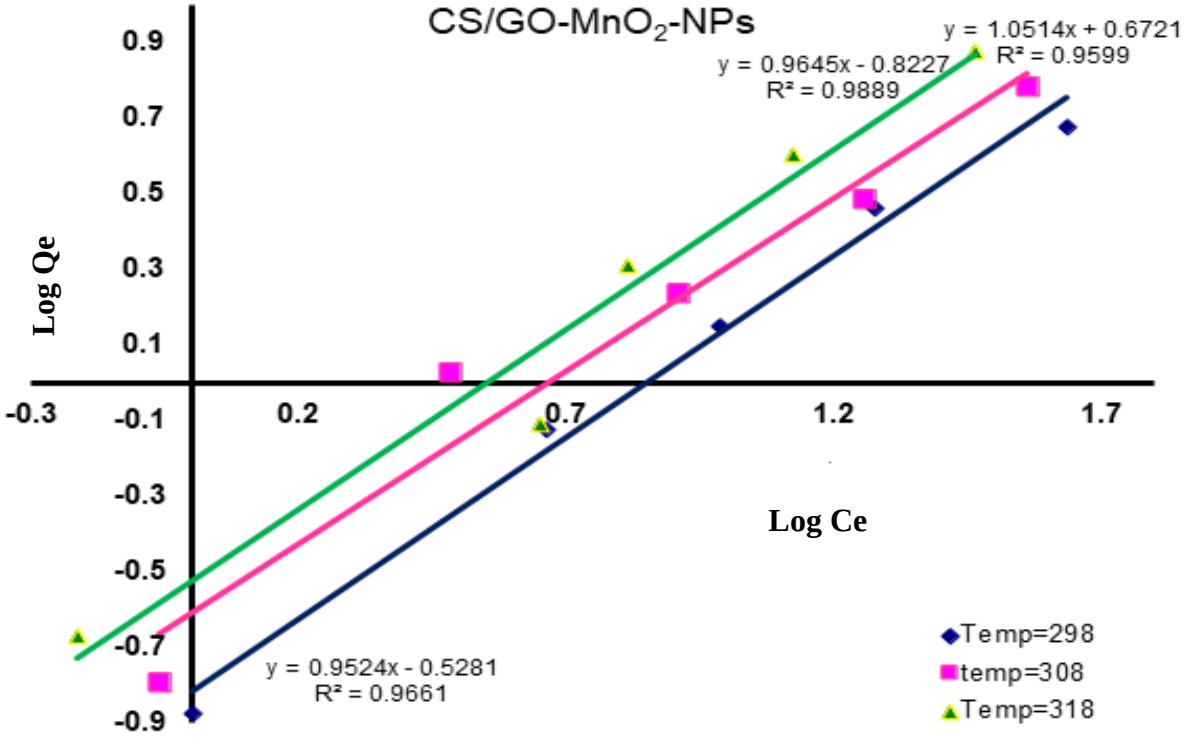

Figure 3.35 Freundlich Lines of the Adsorption of LH Hormone on the CS/GO-MnO_2-NPs Surface.

Adsorption data are often presented in adsorption isotherms, where, for constant temperature, the adsorbed amount is plotted against the protein concentration in the adjacent solution after adsorption. Adsorption isotherms for various proteins on CS/GO-MnO_2-NPs are displayed in Figure 3.25 [249]. By examining the isotherms, it is evident that protein adsorption is strongly influenced by interaction with NPs.

Table 3.11 Adsorption of LH on CS/GO-MnO_2-NPs

Temp C	Co ng/ml	Ce ng/ml	Log Ce	Co-Ce	Q ng/g	Log Q	Ce/Q
25 ^{0}C	0.000	0.000	0.000	0.000	0.000	0.000	0.000
	0.334	0.133	-0.87615	0.201	1.005	0.002166	0.132338
	1.67	0.751	-0.12419	0.918705127	4.593526	0.662146	0.163555
	3.34	1.405	0.147738	1.9348	9.674	0.985606	0.145255
	6.68	2.903	0.462801	3.777310835	18.88655	1.276153	0.153691
	13.36	4.735	0.675275	8.625487051	43.12744	1.634754	0.10978
35 ^{0}C	0.000	0.000	0.000	0.000	0.000	0.000	0.000
	0.334	0.1614	-0.7921	0.1726	0.863	-0.06399	0.187022
	1.67	1.0622	0.026206	0.6078	3.039	0.482731	0.349523
	3.34	1.729	0.237795	1.611	8.055	0.906066	0.214649
	6.68	3.08	0.488551	3.6	18	1.255273	0.171111
	13.36	6.067108	0.782982	7.292892258	36.46446	1.56187	0.166384
45 ^{0}C	0.000	0.000	0.000	0.000	0.000	0.000	0.000
	0.334	0.212	-0.67366	0.122	0.61	-0.21467	0.347541
	1.67	0.78	-0.10791	0.89	4.45	0.64836	0.175281
	3.34	2.036	0.308735	1.3042	6.521	0.814314	0.312191
	6.68	4.033	0.605628	2.647	13.235	1.121724	0.304722
	13.36	7.545	0.877659	5.815	29.075	1.46352	0.259501

Figure 3.36 showed the Vant's Hoff lines of the adsorption of LH on the CS/GO-MnO_2-NPs composites surface.

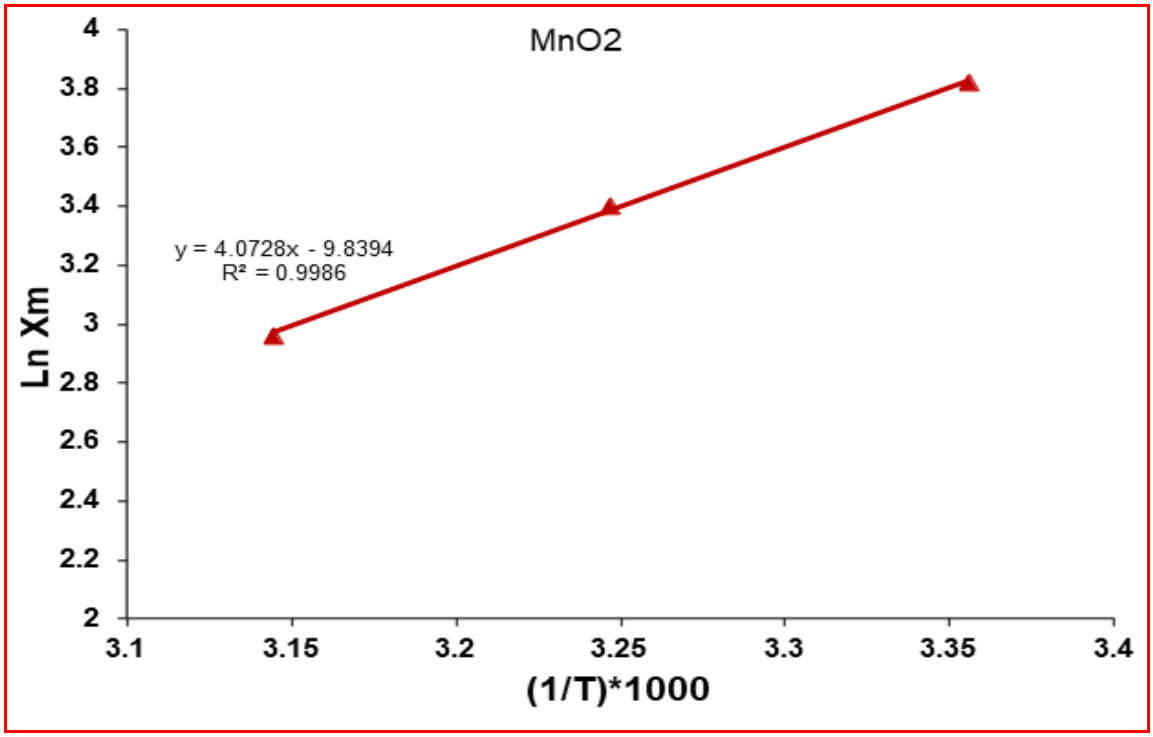

Figure 3.36 Vant's Hoff Lines of the Adsorption of LH on the NPs Composites.

Table 3.12 Thermodynamic Functions of the Adsorption of LH on the CS/GO-MoO_2-NPs Composites

NPs	(1/T)*1000	Xm=Keq	ln Xm	Slope	ΔG° KJ/mol	ΔH° KJ/mol	ΔS° J/mol.k
CS/GO-MnO_2-NPs	3.356	45.541	3.819	4.073	-9.461	-33.86	-81.880
	3.247	30.051	3.403				
	3.145	19.268	2.958				

The plotting of Vant-Hoff's equation for the adsorption process is presented in Figure 3.36. The results of the thermodynamic parameters are presented in Table 3.12. The flexibility of protein structure is usually judged by the hydrogen exchange rate and is expressed in the Gibbs energies of its micro unfolding [283], while the physical measure of the stability of protein structure is the work required for its macroscopic Gibbs energy of unfolding, ΔG.

The Gibbs free energy change (ΔG°) is negative as expected for a spontaneous process. The rise in ΔG° with the rise in temperature shows that the reaction is more favorable at higher temperatures. At higher temperatures, ions are readily desolvated, and hence adsorption becomes more favorable at higher temperatures. Since the adsorption is exothermic, the adsorption process is made unspontaneous because of negative entropy change (ΔS°). The same behavior was reported earlier [284].

3.7 Desorption (recovery) of FSH from NPs

Figure 3.37 shows the fraction of hormones desorbed from Nanoparticles' surfaces.

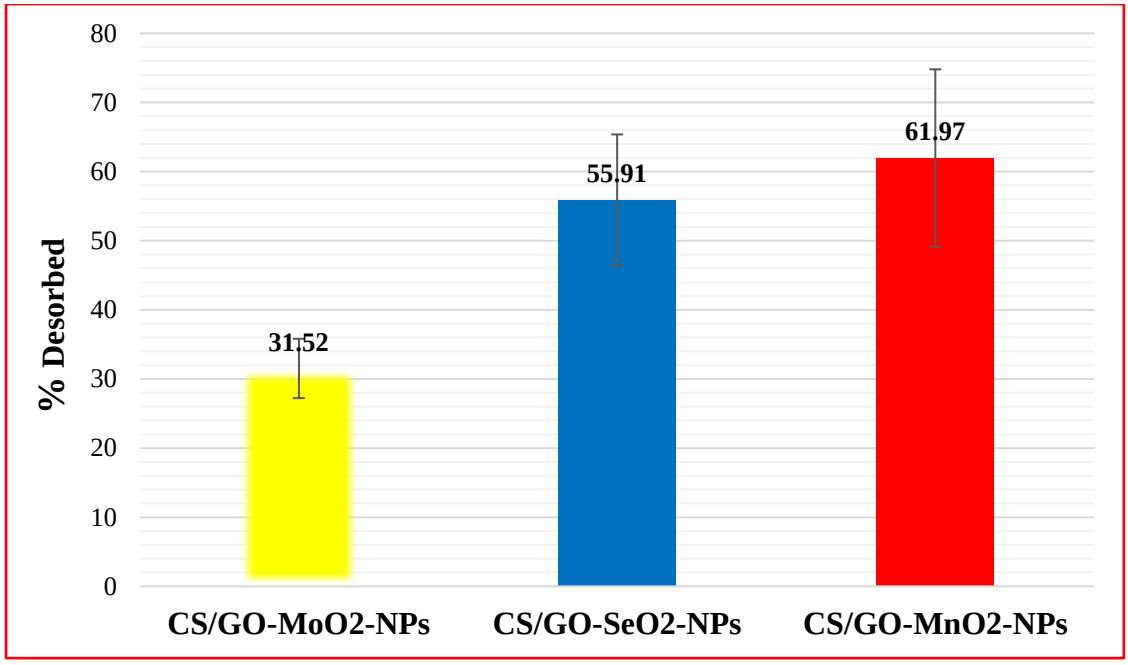

Figure 3.37 Desorption Percentages of FSH Hormones from NPs Surface.

The results showed that the desorption process depends on the temperature and the type of NPs (Figure 3.37). In general, as the amount desorbed grows, the adsorption forces weaken, making the bond between the adsorbent and the adsorbate easy to break. The results of desorption in are presented in Figure 3.37 revealed that the CS/GO-MnO_2-NPs have the

highest desorption percentage (61.97%), leading to the conclusion that the adsorption forces between CS/GO-MnO_2-NPs and adsorbed FSH are weaker than CS/GO-SeO_2-NPs (55.91%) and CS/GO-MoO_2-NPs (31.52%). FSH showed the highest desorption percentage due to the weak forces with CS/GO-MnO_2-NPs [271].

3.8 Desorption (recovery) of LH from NPs

The percentage of the quantities of hormones desorbed from the surface of Nanoparticles are presented in Figure 3.38.

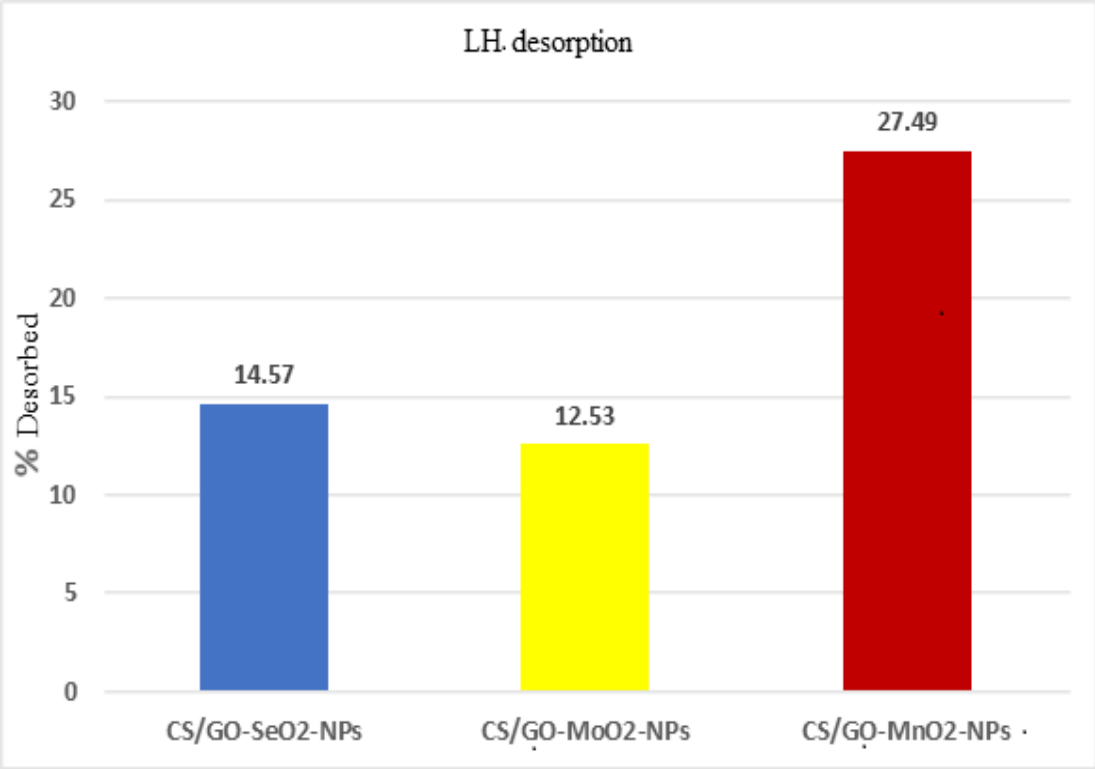

Figure 3.38 Desorption Percentages of LH Hormones from NPs Surface

The percentage of LH hormone desorbed from the surface of the three composites was measured from the amount of LH adsorbed on the surface of the nanomaterials. Results on the desorption process showed that LH desorption from NPs surfaces depends on the temperature and type of NPs, as shown in Figure 3.38.

In general, adsorption forces weaken at high amounts of desorbed composites, leading the linkage between the adsorbent and adsorbate highly susceptible to breakage. The higher the desorption percentage, the lower are the energy of adsorption and attraction forces. The results of desorption are shown in Figure 3.38, it revealed that the LH has the highest desorption percentage (27.49%) with CS/GO-MnO_2-NPs this leads to the conclusion that the adsorption forces between LH (12.53%) and CS/GO-SeO_2-NPs were stronger than LH (14.56%) and CS/GO-MoO_2-NPs. LH showed the highest desorption percentage due to the weak forces with NPs [270].

3.9 Clinical Characteristics

The clinical characteristics of PCOS patients and control groups are presented in Table 3.13.

Table 3.13. Clinical Characteristics of PCOS Patient and Control Groups.

Parameter	Control	PCOS	p
Age (Year)	32.725±6.189	32.088±8.337	N.S.
Weight (Kg)	75.813±11.342	74.875±9.614	N.S.
Height (Cm)	169.15±7.059	167.325±7.252	N.S.
BMI (Kg/m^2)	26.434±3.243	26.779±3.399	N.S.
Regular menstruation Yes/No	30/0	36/84	<0.001
Medication Yes/No	0/30	58/62	N.S.

The age range was 20 to 45 years for both patients and controls. The mean age of attaining menarche in PCOS patients was 32.088±8.337 years, and for controls was 32.725±6.189 years. The mean BMI of PCOS was insignificantly different from the controls.

In Table 3.13, the frequency analysis of Menstrual regulation showed that 36 (30 %) are regular and 84 (70 %) are Irregular. Frequency analysis of medication showed that 58 (48 %) take medication and 62 (52 %) do not. The frequency analysis of BMI showed that 14 (28 %) normal weight, 14 (28 %) overweight, moderate obese16 (32%), 6(12%) obese.

3.9.1 Mu Opioid Receptor (MOR)

The percentage of Mu Opioid Receptor (MOR) in PCOS and controls are shown in Figure 3.39.

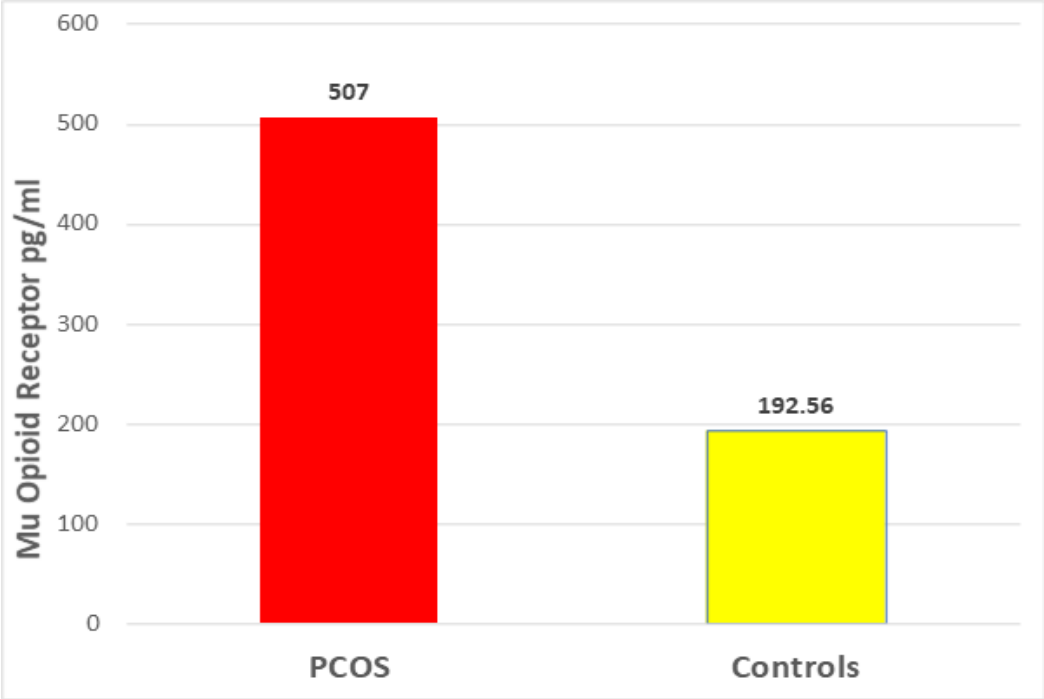

Figure 3.39. Mu Opioid Receptor (MOR) in PCOS and Controls.

The opioid system is involved in the development of PCOS. Although data is inconsistent, opioid activity appears to be changed in women with PCOS, both centrally and peripherally. The aberrant secretory pattern of gonadotropins, as well as the metabolic imbalance seen in women with PCOS, can be influenced by opioids. These systems' interactions are intricate. Opioids, which are thought to be inhibitory neurotransmitters, may have a counterintuitive stimulatory effect on hormone output in PCOS. By influencing important hormones such as LH, FSH, prolactin, and thyroid-stimulating hormone, the opioid system significantly impacts the central regulation of female reproductive function.

Similarly, there is evidence that opioids have peripheral effects on sensitive endocrine tissues [285]. The presence of opioid receptors on the cell surface of human granulosa cells has been found previously [286]. Opioid antagonists such as naltrexone have been used to restore cyclicity in women through improvement in insulin resistance, polycystic ovarian syndrome, hyperinsulinemia, and ovarian hyperstimulation syndrome [287]. In polycystic ovarian syndrome, endogenous opioids are elevated and may stimulate insulin secretion from the endocrine pancreas [288]. Beta-endorphin decreased, and adrenaline increased in women with PCOS. Earlier reports stated that the opioid system decreases sympathetic tone in the brain in normal conditions. Our results in this study confirm the over activity of the sympathetic nervous system, which was due to decreasing opioid system activity in women with PCOS [289]. It is found that Persistent opioid receptor engagement (either elicited exogenously or endogenously) occurs at the expense of distinct physiological programs (e.g., reproduction), thus eventually invoking disease [290]. In women with PCOS, growing evidence suggests dysregulation of the opioid system both centrally and peripherally, with complex interactions [291].

The relationship between insulin resistance and μ-opioid neurotransmission in limbic appetite and mood-regulating regions in women with PCOS suggests that insulin–opioid interactions may contribute to behavioral and reproductive pathologies of PCOS. Patients with PCOS who are insulin-resistant had greater limbic μ-opioid receptor availability (nondisplaceable binding potential) than controls [292].

Clinically, the links between the opioid regimen and changes in FSH and LH were explored by increasing the percentage of the opioid receptor with PCOS to 507 but in controls was 192.56 as shown in Figure 3.39. The

presence of MOR in human endometrium and the dynamic changes during the menstrual cycle suggest a possible role for opioids in reproduction events related to the human endometrium or endometriosis [293].

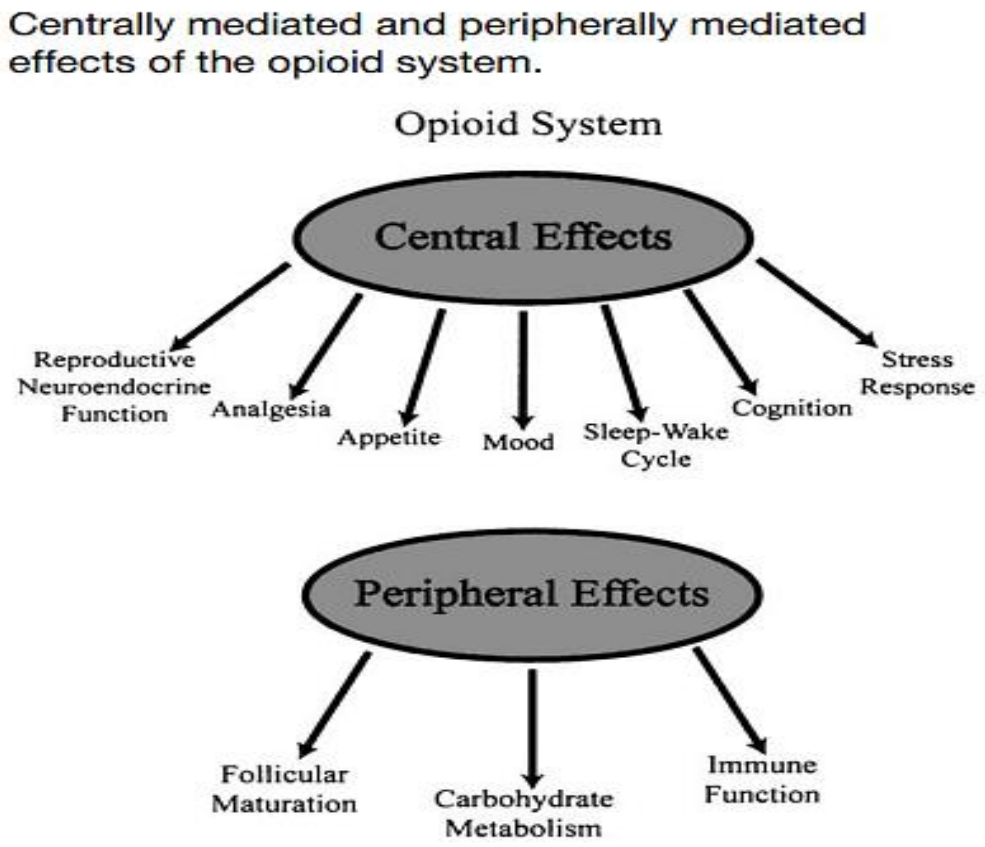

Figure 3.40. Opioids and Polycystic Ovary Syndrome.

Endogenous opioids serve important and well-studied functions in reproductive neuroendocrine function, stress response, and analgesia at the central level. As demonstrated in Figure 3.40, the opioid system also has an impact on behavior, hunger regulation, body temperature, respiratory activity, sleep-wake cycle, and follicular maturation in the reproductive cycle. The opioid abnormalities in PCOS and the impact of potential modulation by nanoparticles are presently unknown, but evidence suggests a decreased central opioid sensitivity in patients with PCOS, as in Figure 3.39.

3.9.2 Comparison of FSH and LH in case versus control group

The levels of the quantities of hormones desorbed from the surface of NPs are presented in Figure 3.41.

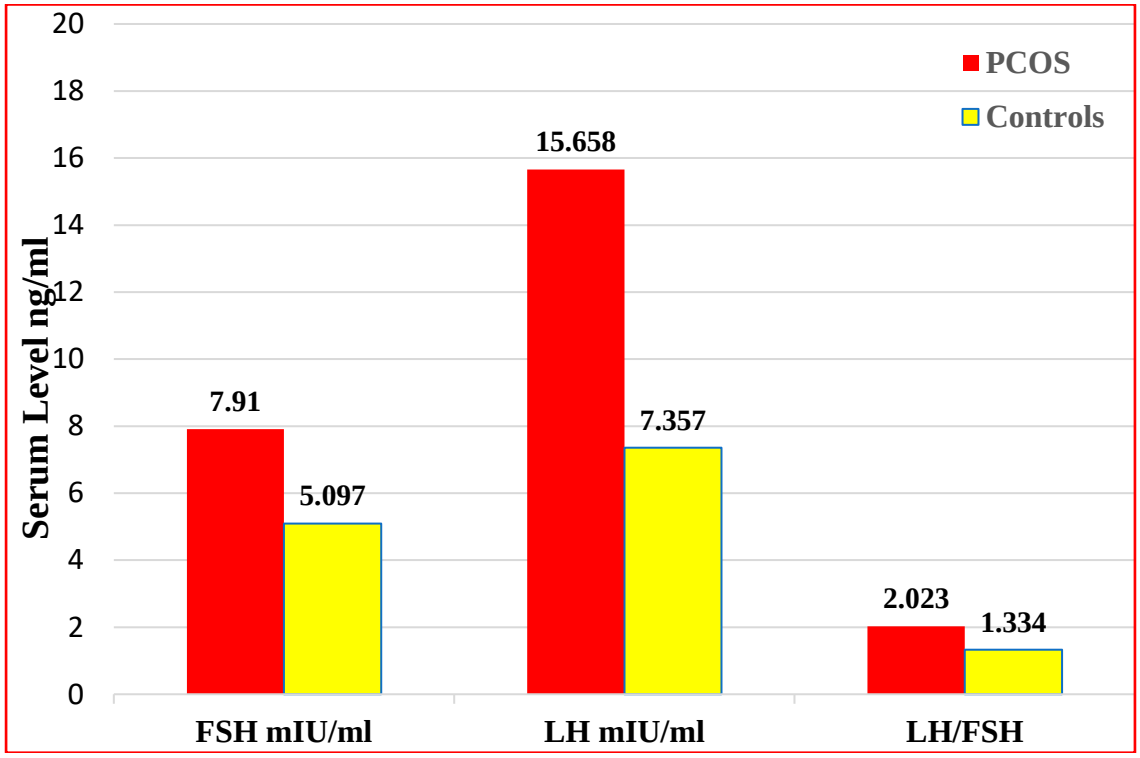

Figure 3.41 Serum Levels FSH and LH in Women with PCOS.

When the amount desorbed grows, the adsorption forces weaken, making the bond between the adsorbent and the adsorbate easy to break. The desorption results are shown in Figure 3.41 revealed that the FSH levels were significantly elevated with values from 5.097 to 7.91 ng/ml, as in Figure 3.41. An abrupt decline in FSH concentrations occurred shortly after reaching 2.023 ng/ml levels.

The commencement of the spermatogenic process, which involves the division of gonocytes to become spermatogonia, could be aided by increased FSH levels. The increased levels during this time could be linked to spermatid maturation, and the following fall implies that an intact and mature seminiferous epithelium is required to have a feedback effect on FSH secretion. It's worth noting that the onset of this rise coincides with rising LH levels, which continue to climb after FSH levels have dropped, implying that these two hormones have separate control systems.

The LH levels at different stages of development are illustrated in Figure 3.41. Serum LH levels ranged from 7.357 ng/ml to 15.658. Where the gradual rise was evident, and peak levels were reached. The surge in serum LH detected at this time suggests a functional pituitary-testicular link and may signal the start of the adult interstitial cell production. The rise in serum LH and testosterone levels is suggestive of the need for more testosterone to impose feedback on LH secretion.

3.9.3 Effects of Calcium in Women with PCOS

Figure 3.42 shows the effects of calcium in women with PCOS.

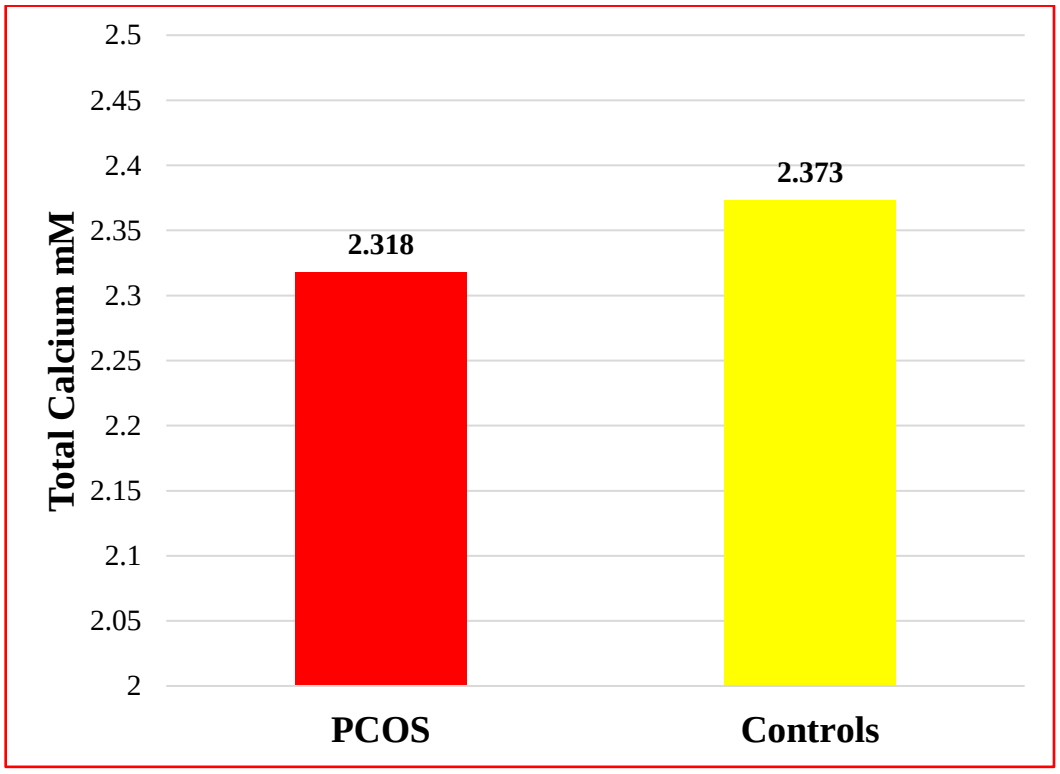

Figure 3.42 Effects of Calcium in Women with PCOS

Calcium plays a major role in mammals' oocyte maturation, which induces hyperandrogenism followed by menstrual irregularity. PCOS patients had lower serum calcium levels than patients without PCOS [294]. Some research suggested a possible role of calcium and vitamin D supplements in managing PCOS [295]. Besides, abnormalities in calcium homeostasis and parathyroid hormone (PTH) levels secondary to vitamin D deficiency may be responsible for the arrested follicular development and menstrual dysfunction in women with PCOS [296].

Many experiments have proved the effect of low calcium intake on weight gain and body composition [297]. The direct effect of calcium and vitamin D on the ovarian and/or adrenal steroid genesis pathway may be

justified by the observed reduction in circulating androgens [298]. A significant decrease in the level of vitamin D; has also been reported, glucose and phosphorus levels in overweight, obese women with PCOS correlated negatively with insulin and insulin resistance and positively with vitamin D levels [299].

3.9.4 Effects of Magnesium in Women with PCOS

Figure 3.43 shows the effects of magnesium in Women with PCOS.

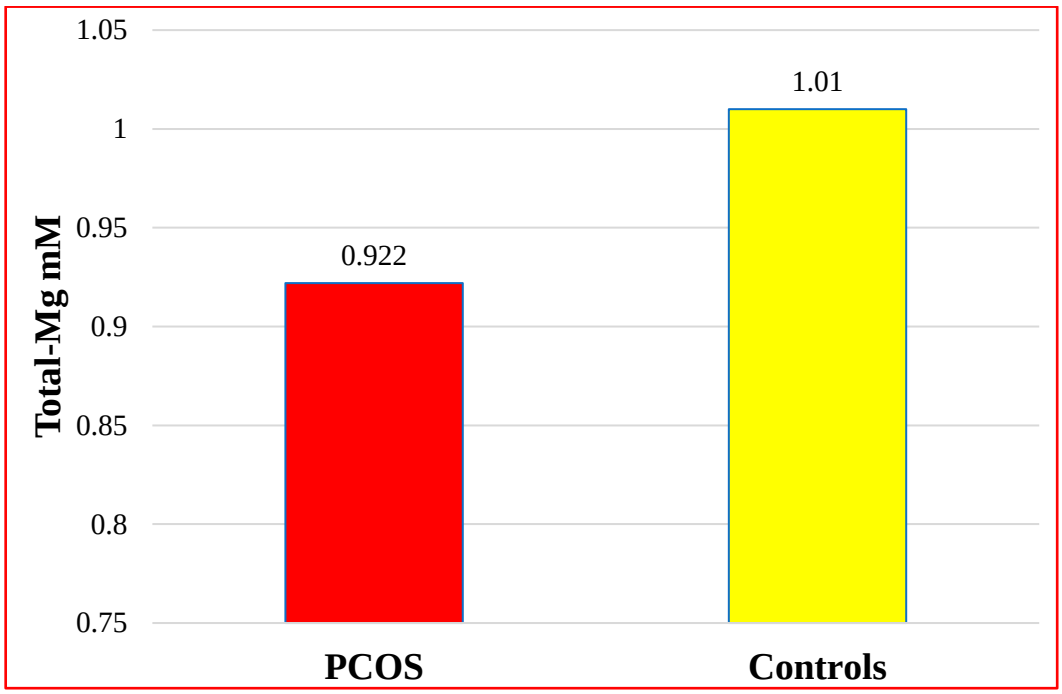

Figure 3.43 Effects of Magnesium in Women with PCOS

The current study demonstrated that magnesium was associated with a significant reduction in hirsutism in women with PCOS, where the ratio of the effect of magnesium on women with PCOS was 0.922 but did not affect serum total testosterone and did not affect other hormonal profiles [300].

Several potential mechanisms through which magnesium may improve ovarian functions are proposed, including the antioxidant and anti-inflammatory activities of magnesium [301, 302].

3.9.5 Effects of Albumin in Women with PCOS

Figure 3.44 shows the effects of albumin in Women with PCOS

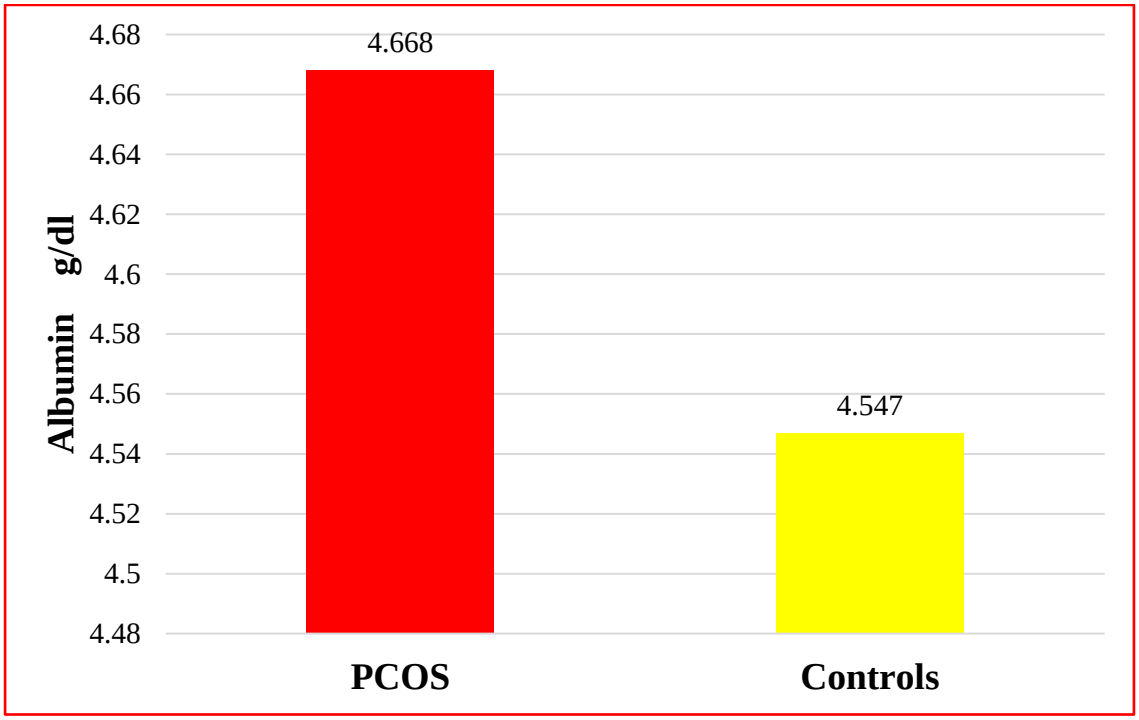

Figure 3.44 Effects of Albumin in Women with PCOS

Albumin excretion in women with PCOS correlates well with other cardiovascular risk factors, likely aggravating factors, such as hyperinsulinemia or borderline hypertension. These variables were relied upon for analysis given their likely or postulated relationship to albumin excretion and/or their prominent role in PCOS pathophysiology, as shown in Figure 3.44.

Albumin is a liver-produced negative acute phase response protein. Albumin levels in the blood are lower in people who are suffering from chronic inflammation [303]. Albumin provides the bulk of the overall antioxidant capacity of normal plasma, in addition to its activity as a sex steroid binding molecule [303, 304]. In premenopausal women with induced changes in their ovarian hormone status, the ratio of serum C-reactive protein (CRP) to serum albumin (CRP/albumin) was substantially linked to more severe metabolic dysfunction [305]. In premenopausal women with PCOS, the CRP/albumin ratio was likewise considerably greater than in controls, and this negatively predicted their bone quality [306]. Given CRP/capacity albumin's to detect chronic inflammation and metabolic impairment in premenopausal women at the same time.

3.9.6 The Ratio of Albumin/calcium in Women with PCOS

Figure 3.45 shows the ratio of calcium/albumin in Women with PCOS.

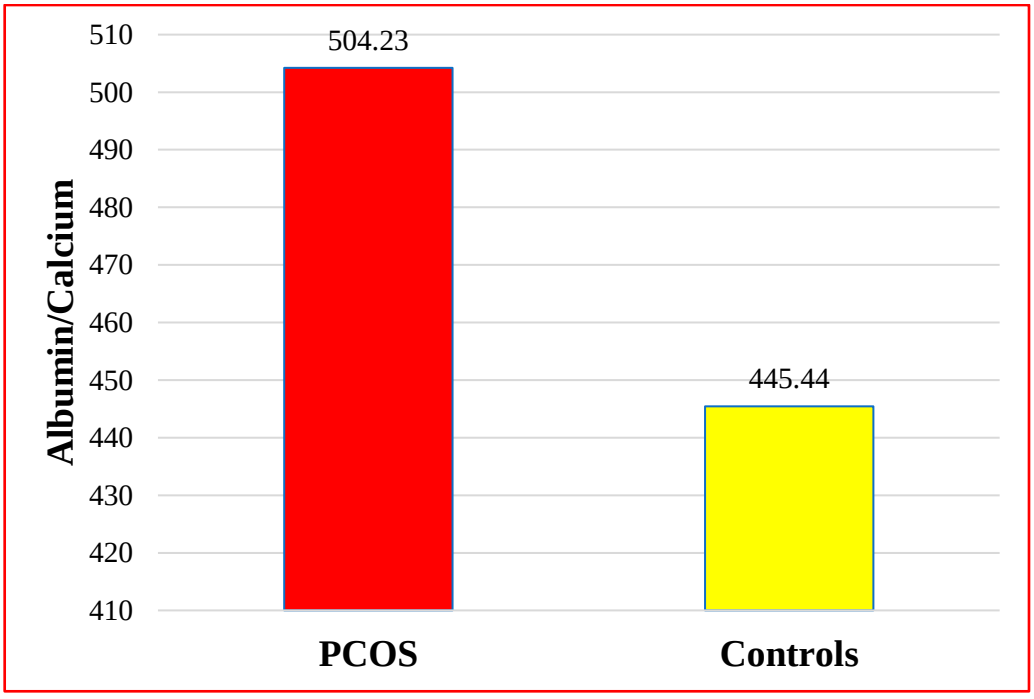

Figure 3.45 The Ratio of Calcium/Albumin in Women with PCOS.

The ratio of serum albumin levels over serum calcium (albumin / Ca) was found to be highly related to more severe metabolic dysfunction in premenopausal women with induced alterations to their ovarian hormone status [307].

In premenopausal women with PCOS, the albumin/calcium ratio was likewise considerably greater than in controls [308]. We anticipated that the albumin/calcium ratio could serve as a robust predictor of PCOS in a population of similarly aged women because of its potential to capture chronic inflammation and metabolic dysfunction in premenopausal women. For any given BMI value, the model found that women with PCOS have significantly higher albumin/calcium levels.

3.9.7 Ionized Calcium / Magnesium in Women with PCOS

Figure 3.46 shows ionized calcium/magnesium in Women with PCOS

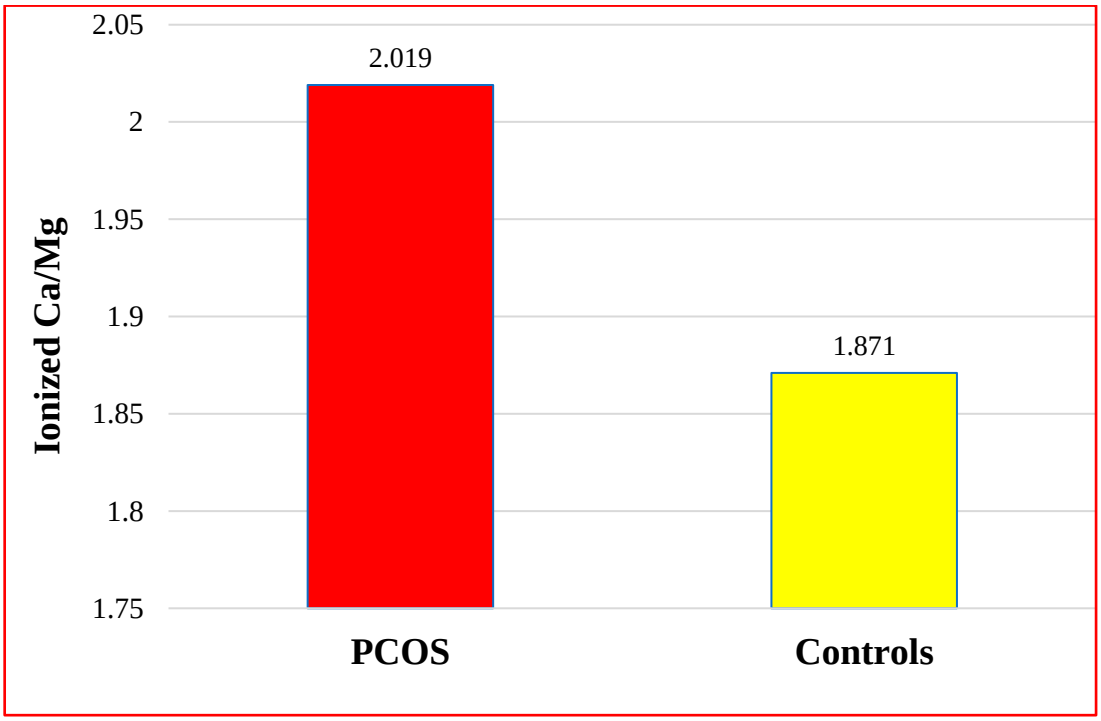

Figure 3.46 Ionized Calcium / Magnesium in Women with PCOS

Patients with the polycystic ovarian syndrome (PCOS) have a high rate of insulin resistance and glucose intolerance, putting them at risk for hypertension, diabetes, and cardiovascular disease. Insulin resistance, cardiovascular issues, diabetes mellitus, and hypertension are all linked to the high ionized calcium to magnesium (Ca^{2+}/Mg^{2+}) ratio, according to numerous studies. As a result, we wanted to compare the serum divalent cation profile of PCOS patients to that of healthy women of similar age. When compared to controls, PCOS patients had significantly lower serum Mg^{2+} and total magnesium levels, as well as a significantly higher serum Ca^{2+}/Mg^{2+} ratio. The serum concentrations of steroid hormones (estrogen, progesterone, and testosterone), as well as any of the cations in PCOS patients and controls, were found to have no association [309].

3.9.8 Total Calcium / Magnesium in Women with PCOS

Figure 3.47 shows the total Calcium / Magnesium in Women with PCOS

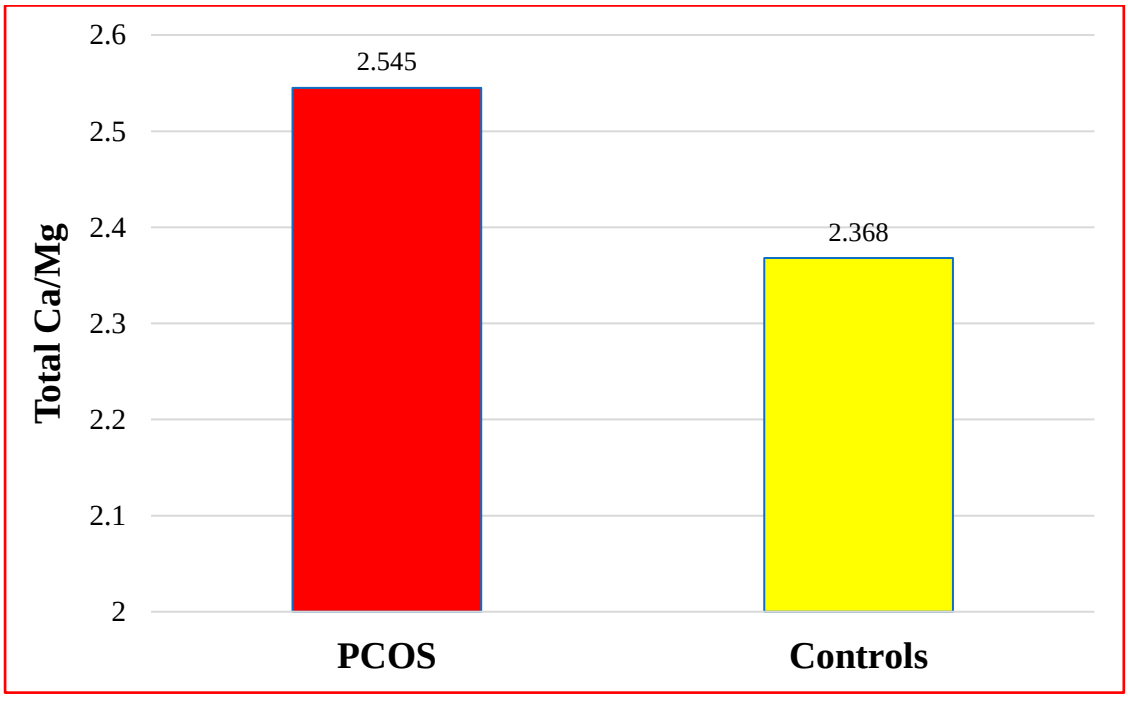

Figure 3.47 Total Calcium / Magnesium in Women with PCOS

The changes in serum Ca and Mg concentrations can affect such entities as vasculature, excitation-secretion coupling, and synaptic transmission [310]. The serum ionized Mg, Ca, and Ca/Mg ratio all changed with the menstruation phases, according to Shaba'a-safanah et al. (2009). Increased testosterone levels were associated with a decrease in ionized Mg. In PCOS patients, serum calcium levels were higher than in healthy control women. Some research looked at the effects of calcium consumption on heart disease and discovered a variety of relationships. In one study, calcium supplementation was found to have a beneficial effect on the treatment of hypercholesterolemia patients [311]. A high calcium intake is also linked to a plasma lipoprotein-lipid profile that predicts a lower risk of coronary heart disease compared to a low calcium intake. The amount of calcium consumed daily was found to be negatively associated with plasma LDL cholesterol, total cholesterol, and HDL cholesterol [309].

3.9.9 Prolactin Levels in Women with the PCOS

Figure 3.48 shows prolactin Levels in Women with the PCOS

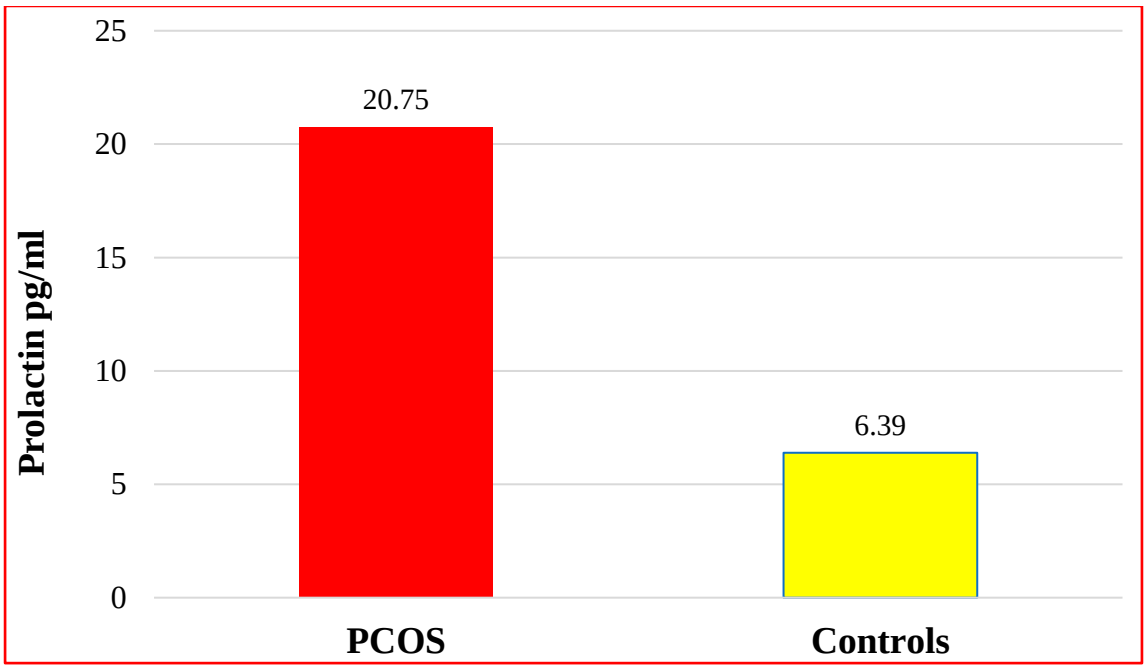

Figure 3.48 Prolactin Levels in Women with the PCOS

Prolactin levels appeared to be slightly higher in women without PCOS, but the difference did not reach a border of statistical significance. Elevated prolactin concentrations were higher in women without PCOS than in PCOS patients. Also, elevated mean prolactin was more frequent in the group of women without PCOS than in those with PCOS. It has been observed that a normal increase in prolactin occurs after ovulation and that a weak response follows the period of ovulation.

Polycystic ovaries, which indicate chronic anovulation, can be detected in a variety of endocrine disorders, including hyperprolactinemia, which is characterized by ovulation failure [312, 313]. PCOS had typical gonadotrophin, and androgen secretion [314], and mild hyperprolactinemia has been reported to occur in up to 67% of these patients [315, 316].

There are two theories that have been proposed to explain how polycystic ovarian syndrome develops. To begin with, persistent unopposed hyperoestrogenaemia is a possible reason for the normally increased LH levels [317]. Oestrogen also stimulates PRL secretion [318] and could therefore induce hyperprolactinemia in PCOS. Second, PCOS can cause a dopamine deficit in the hypothalamus [319]. Because hypothalamic dopamine is the main inhibitor of PRL production, a lack of it can lead to hyperprolactinemia. To find the reasons for hyperprolactinemia, specifically macroprolactinomas, it is recommended that PCOS patients have their prolactin levels checked [320]. In 30% of PCOS cases, a little increase in blood prolactin levels can be found in both the follicular and luteal phases [321]. According to research, an increase in blood prolactin levels might lead to a decrease in ovarian follicles and ovulation [322].

Hyperprolactinemia is a prevalent endocrine disorder that can affect men and women of all ages, depending on the studied group [323]. Pathological circumstances, physiologic changes, medications, and excess macroprolactin can all cause hyperprolactinemia [324, 325]. Pregnancy, stress, heavy activity, and lactation are all physiological causes; however, pathological causes include polycystic ovarian syndrome, chronic renal disease, chest wall surgery or trauma, cirrhosis, prolactinoma, and hypothyroidism. Hyperprolactinemia can also be caused by drugs. Antidepressants, antipsychotics, and anti-emetics medications are the most prevalent drugs that cause hyperprolactinemia [324, 325]. Idiopathic hyperprolactinemia refers to hyperprolactinemia caused by unknown factors, which accounts for 29% of all cases [326].

3.9.10 Testosterone Levels in Women with the PCOS

Figure 3.49 shows testosterone levels in women with the PCOS

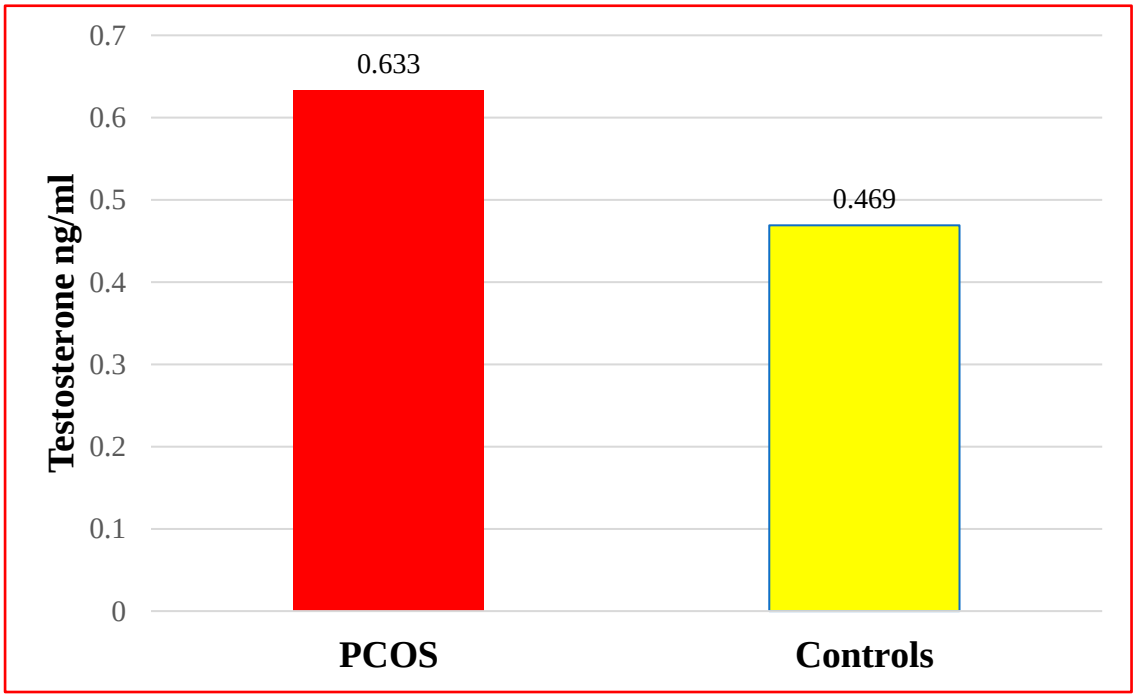

Figure 3.49 Testosterone Levels in Women with the PCOS

Testosterone levels were similar in women with PCOS who were 20–45 years of age. Testosterone levels were increased in younger and older women with PCOS compared with controls but were similar to controls in women 42–45 years of age. As expected, the testosterone level was higher in women with PCOS compared to controls. Figure 3.49 shows that the overall level of testosterone was lower in older women with PCOS. Our findings indicate that testosterone level decreases in women with PCOS in middle age. This reduction in hyperandrogenism may explain the tendency of women with PCOS to cycle regularly as they grow older [327], although the cause-and-effect relationship between these age-associated events remains speculative.

The cause of low testosterone levels and the incidence of age in women with PCOS is currently unknown. The reason is a low level of testosterone resulting in a decrease in the production of testosterone is suggested. Luteinizing hormone (LH) are thought to be major stimulators of testosterone secretion in PCOS. LH levels were higher in older PCOS women, therefore the decrease in testosterone levels cannot readily be explained by the change in LH levels [328].

In women with PCOS, hyperandrogenism is partially cured before menopause. This shift could explain why women with PCOS are more likely to cycle regularly as they become older. However, testosterone levels in older women with PCOS remain excessive, which may contribute to their increased risk of cardiovascular disease, endometrial cancer, and other disorders [329].

3.10 Effect of the Serum components on the hormone-composite interaction

3.10.1 Effect of the Serum components on the FSH-composites interaction

The correlations between serum components on the amount of FSH adsorbed on the surfaces of CS/GO-SeO_2-NPs, CS/GO-MoO_2-NPs, and CS/GO-MnO_2-NPs are presented in Table 3.14.

Table 3.14. Correlation between Serum Components with the Quantity of FSH Adsorbed on the Surfaces of the Prepared Composites.

FSH			
	CS/GO-SeO_2-NPs	**CS/GO-MoO_2-NPs**	**CS/GO-MnO_2-NPs**
Albumin	0.652**	0.405**	0.415**
T.Ca	-0.079	0.124	0.124
Albumin/Ca	0.674**	-0.138	-0.138
I.Ca	-0.102	0.132	0.132
T.Mg	0.165	0.321**	0.387**
I.Mg	0.165	0.321**	0.387**
T.Ca/Mg	0.050	-0.656**	-0.444**
I. Ca/Mg	0.071	-0.133	-0.175
FSH	0.710**	0.862**	0.426**
LH	0.071	-0.304**	-0.204
LH/FSH	0.032	-0.329**	-0.188
MOR	0.088	-0.364**	-0.164
PRL	0.047	-0.243*	-0.269**
Testosterone	0.168	-0.266**	-0.187
**. Correlation is significant at the 0.01 level (2-tailed).			

Regarding the adsorption of FSH on CS/GO-SeO_2-NPs surface. There is a significant correlation between serum albumin ($r = 0.652$, $p<0.01$) and Albumin/Ca ($r=0.674$, $p<0.01$) with the amount of FSH adsorbed [330].

For the adsorption of FSH on CS/GO-MoO_2-NPs surface. There is a significant correlation between the FSH adsorbed and serum albumin ($r = 0.405$, $p<0.01$) and magnesium ($r = 0.321$, $p<0.01$). While negative significant correlations were recorded between the amount of FSH adsorbed and T.Ca/Mg ($r = -0.656$, $p<0.01$), LH ($r = -0.304$, $p<0.01$), LH/FSH ($r = -0.656$, $p<0.01$), MOR ($r = -0.364$, $p<0.01$), prolactin ($r = -0.243$, $p<0.05$), and testosterone ($r=-0.266$, $p<0.01$) [331].

Regarding the adsorption of FSH on CS/GO-MnO_2-NPs surface. The results showed a significant correlation between the FSH adsorbed and serum albumin ($r = 0.415$, $p<0.01$), magnesium ($r = 0.387$, $p<0.01$), T.Ca/Mg ($r = -0.444$, $p<0.01$), and prolactin ($r = -0.269$, $p<0.01$) [332]. Having nanoparticles, In the presence of 20 ng of nanoparticle and serum, FSH additives enhanced the inhibition process. This feature hardly could be expected were the serum inhibition in itself an FSH effect on the nanoparticle. Because of this result and as shown in table 3.15 which shows the correlation between the components of the serum with the adsorption of FSH compounds we conclude that serum components with adsorption of compounds bind reversibly. The important observation is that the presence of serum components significantly reduces the charge of the nanocomposite. This result is reinforced by the measurements shown in Table 3.15, which indicate a decrease in the charge of the serum solution.

Table 3.15 Correlation between Serum Components with the Quantity of FSH Desorption on the Surfaces of the Prepared Composites.

FSH			
	CS/GO-SeO_2-NPs	**CS/GO-MoO_2-NPs**	**CS/GO-MnO_2-NPs**
Albumin	0.078	0.088	0.050
T.Ca	-0.063	-0.051	-0.026
Albumin/Ca	-0.027	-0.024	-0.049
I.Ca	-0.038	-0.028	-0.001
T.Mg	-0.139	-0.163	-0.130
I.Mg	-0.139	-0.163	-0.130
T.Ca/Mg	0.035	0.074	0.083
I. Ca/Mg	0.088	0.129	0.128
FSH	0.207	0.315	0.264
LH	0.148	0.120	-0.060
LH/FSH	0.248^{**}	0.160	0.035
MOR	0.232^{*}	0.135	-0.012
PRL	0.148	0.117	-0.063
Testosterone	0.202^{*}	0.284^{**}	0.092

The purpose of this investigation was to identify serum components through the uptake process, capable of inhibiting the morphological response induced by FSH hormone on CS/GO-SeO_2-NPs surface. Regarding the adsorption of FSH on CS/GO-SeO_2-NPs surface. There is a significant correlation between serum albumin ($r = 0.078$, $p<0.01$) and Albumin/Ca ($r = -0.027$, $p<0.01$) with the amount of FSH adsorbed [332].

For the adsorption of FSH on CS/GO-MoO_2-NPs surface. There is a significant correlation between the FSH adsorbed and serum albumin ($r = 0.088$, $p<0.01$) and magnesium ($r = -0.163$, $p<0.01$). While positive significant correlations were recorded between the amount of FSH adsorbed and T.Ca/Mg ($r = 0.074$, $p<0.01$), LH ($r = 0.120$, $p<0.01$), LH/FSH

(r =0.160, p<0.01), MOR (r =0.135, p<0.01), prolactin (r =0.117, p<0.05), and testosterone (r =-0.284, p<0.01) [331].

Regarding the adsorption of FSH on CS/GO-MnO_2-NPs surface. The results showed a significant correlation between the FSH adsorbed and serum albumin (r =0.050, p<0.01), magnesium (r =-0.130, p<0.01), T.Ca/Mg (r =0.083, p<0.01), and prolactin (r =-0.063, p<0.01) [271]. The results of this investigation provide further information on the effects of the Serum components on the FSH-composites interaction. We have specifically shown that albumin is the serum component that inhibits hormone-induced morphological alterations.

3.10.2 Effect of the Serum components on the LH-composites interaction

The correlations between serum components on the amount of LH adsorbed on the surfaces of CS/GO-SeO_2-NPs, CS/GO-MoO_2-NPs, and CS/GO-MnO_2-NPs are presented in Table 3.16.

Table 3.16. Correlation between Serum Components with the Quantity of LH Adsorbed on the Surfaces of the Prepare Composites.

LH			
	CS/GO-SeO_2-NPs	**CS/GO-MoO_2-NPs**	**CS/GO-MnO_2-NPs**
Albumin	-0.435**	-0.452**	-0.306**
T.Ca	0.321**	0.299**	0.316**
Albumin/Ca	-0.179	-0.102	0.150
I.Ca	0.304*	0.244*	0.308**
T.Mg	0.124	0.132	0.156
I.Mg	0.124	0.132	0.156
T.Ca/Mg	0.216*	0.308**	0.328**
I. Ca/Mg	0.340**	0.332**	0.237*
FSH	0.186	0.189	0.197
LH	0.391**	0.295*	0.278*
LH/FSH	0.116	0.118	0.200
MOR	-0.107	0.171	0.280**
PRL	0.039	0.037	0.194
Testosterone	-0.080	-0.086	0.160
**. Correlation is significant at the 0.01 level (2-tailed).			

The results of this investigation indicate that albumin is the primary serum component responsible for inhibiting morphological alterations induced by LH. The LH uptake was tested on the surface of the prepared CS / GO-SeO_2-NPs. The results in Table 3.16 indicate that the uptake of LH in the serum was significantly reduced. There is a significant

correlation between serum albumin (r =-0.435, p<0.01), calcium (r =0.321, p<0.01) and Albumin/Ca (r =-0.179, p<0.01) and T.Ca/Mg (r =0.216, p<0.01) with the amount of LH adsorbed [333]. For the adsorption of LH on CS/GO-MoO_2-NPs surface. There is a significant correlation between the LH adsorbed serum albumin (r =-0.452, p<0.01) and calcium (r =0.299, p<0.01). While significant correlations were recorded between the amount of LH adsorbed and T.Ca/Mg (r =0.308, p<0.01), LH (r =-0.295, p<0.01), LH/FSH (r =0.118, p<0.01), MOR (r =0.171, p<0.01), prolactin (r =0.037, p<0.05), and testosterone (r =-0.086, p<0.01) [334].

As for the adsorption of LH on CS/GO-MnO_2-NPs surface. The results showed a significant correlation between the LH adsorbed and serum albumin (r =-0.306, p<0.01), calcium (r =0.316, p<0.01), T.Ca/Mg (r=0.328, p<0.01), MOR (r =0.280, p<0.01) and prolactin (r =0.194, p<0.01). The results as shown in Table 3.16 indicate that the uptake of LH hormone in the serum was significantly reduced. Demonstrating the inhibition of binding of the components of the serum to the interaction of the LH compounds [271].

Table 3.17 Correlation between Serum Components with the Quantity of LH Desorption on the Surfaces of the Prepared Composites.

LH			
	CS/GO-SeO_2-NPs	**CS/GO-MoO_2-NPs**	**CS/GO-MnO_2-NPs**
Albumin	-0.267*	-0.244*	-0.211
T.Ca	0.102	-0.085	-0.106
Albumin/Ca	-0.110	-0.053	0.174
I.Ca	0.031	-0.059	-0.091
T.Mg	-0.056	0.014	0.009
I.Mg	-0.056	0.014	0.009
T.Ca/Mg	0.041	-0.103	-0.119
I. Ca/Mg	0.062	-0.073	-0.089
FSH	0.140	0.123	0.223*
LH	0.247**	0.082	0.265**
LH/FSH	0.016	-0.005	0.186*
MOR	0.163	0.154	0.204*
PRL	0.204*	-0.037	0.092
Testosterone	-0.016	-0.155	-0.035

The effect of Serum components on the LH-composites interaction adsorption CS/GO-SeO_2-NPs. This inhibitory effect has been ascribed to the content of the hormone in human serum, Experiments are presented in which the hormone-composite is reacted with human serum and varying concentrations of LH. Regarding the adsorption of LH on CS/GO-SeO_2-NPs surface. There is a significant correlation between serum albumin ($r = -0.267$, $p<0.01$), Albumin/Ca ($r = -0.110$, $p<0.01$), LH ($r = 0.247$, $p<0.01$), and prolactin ($r = 0.204$, $p<0.01$),with the amount of LH adsorbed [271].

While the adsorption of LH on CS/GO-MoO_2-NPs surface. There is a significant correlation between the LH adsorbed and serum albumin (r =-0.244, p<0.01) and magnesium (r =0.014, p<0.01). While negative significant correlations were recorded between the amount of LH adsorbed and T.Ca/Mg (r =-0.103, p<0.01), LH (r=-0.082, p<0.01), LH/FSH (r =-0.005, p<0.01), MOR (r =0.154, p<0.01), prolactin (r =-0.037, p<0.05), and testosterone (r =-0.155, p<0.01) [335].

As for the adsorption of LH on CS/GO-MnO_2-NPs surface. The results showed a significant correlation between the LH adsorbed and serum albumin (r =-0.211, p<0.01), T.Ca/Mg (r =-0.119, p<0.01), FSH (r =0.223, p<0.01), LH (r =0.265, p<0.01), LH/FSH (r =0.186, p<0.01) and MOR (r =0.204, p<0.01). Because of this result and as shown in table 3.17 which shows the correlation between the components of the serum with the adsorption of LH compounds we conclude that serum components with adsorption of compounds bind reversibly. The important observation is that the presence of serum components significantly reduces the charge of the nanocomposite [271]. This result is reinforced by the measurements shown in Table 3.17, which indicate a decrease in the charge of the serum solution.

Chapter 4
Conclusions & Recommendation

4.1 Conclusions

From the results of the present study, the following points can be concluded:

1. Novel composites were synthesized by coating a core of metal oxides with chitosan and graphene oxides.
2. The composites were characterized by advanced techniques and have the following formulas: CS/GO- SeO_2, CS/GO-MoO_2, CS/GO-MnO_2.
3. The synthesis composites have the ability to adsorb two important hormones (FSH and LH) from the blood of patients with PCOS.
4. The adsorbed hormones were recovered and separated from the composites with a good recovery percentage.
5. The thermodynamic functions ($\Delta G°$, $\Delta H°$, & $\Delta S°$) of the adsorption of LH and FSH on the prepared composites were calculated.
6. The biochemical characteristics of the PCOS patients were measured and correlated with the hormones quantities that adsorbed and desorbed on the surface of the synthesized composites.
7. The quantities of hormones adsorbed on the NPs composites were correlated with the biochemical concentration in the serum of patients with PCOS.

4.2 Recommendations and Future Works

The following points can be recommended:

1. The synthesis NPs composites need more to be investigated and modificated to increase their ability to adsorb certain hormones effectively and selectively from the human serum.
2. Other hormones can be used as adsorbates on the surface of the prepared composites as means for extraction of those valuable hormones from serum.
3. Synthesis of more NPs composites for extraction of proteins from human serum.

4.3 Publishing Papers and Conferences

A. Papers:

1. *Assel A. Hadi, Nada Y. Fairooz, Hussein K Al-Hakeim* "Separation of Follicular-Stimulating Hormone from Serum by Chitosan-Graphene Oxide-Selenium Oxide Nanocomposites" ISSN: (0005-2523 Volume 62, Issue 07, September, 2022) in the Azerbaijan Medical Journal.

2. *Assel A. Hadi, Nada Y. Fairooz, Hussein K Al-Hakeim* "Effect of Modified Nanoparticles on the Levels of Some Important Proteins in the Blood" ISSN: (0094243X, 15517616) April 14-15, 2022. Iraq in the AIP Journal of Physics.

3. *Assel A. Hadi, Nada Y. Fairooz, Hussein K Al-Hakeim* "Adsorption of Hormones FSH and LH on the Chitosan-Graphene Oxide-Molybdenum Oxide Nanocomposites" ISSN: (0005-2523

Volume 62, Issue 07, September, 2022) in the Azerbaijan Medical Journal.

B. Conference:

1. Iraq Academics Syndicate 2nd International Conference for Pure and Applied Sciences, Babylon, Iraq 14-15 November 2021. "Separation of Follicular-Stimulating Hormone from Serum by Chitosan-Graphene Oxide-Selenium Oxide Nanocomposites"

2. Iraq Academics Syndicate 4th International Scientific Conference of Engineering Sciences and Advances Technologies, Babylon, Iraq 14-15 April 2022. "Effect of Modified Nanoparticles on the Levels of Some Important Proteins in the Blood"

3. The 7th International Scientific Conference for Biological Sciences, Al-Mustansiriyah University, Iraq, 30-31 August 2022. “Adsorption of Hormones FSH and LH on the Chitosan-Graphene Oxide-Molybdenum Oxide Nanocomposites.”

4. The Seventeenth Scientific Symposium for Graduate Studies, University of Babylon, College of Science, Department of Chemistry, 28-4-2021, Wednesday, under the slogan "Postgraduate studies is a way to advance practical research and society"

5. The Eighteenth Scientific Symposium for Graduate Studies, University of Babylon, College of Science, Department of Chemistry, 12-5-2022 Thursday under the slogan "Sober scientific research is the way to advance higher studies"

References

1. Jeevanandam, J., *et al*., *Review on nanoparticles and nanostructured materials: history, sources, toxicity and regulations.* Beilstein journal of nanotechnology, 2018. **9**(1): p. 1050-1074.
2. Robinson, R.L.M., *et al*., *How should the completeness and quality of curated nanomaterial data be evaluated?* Nanoscale, 2016. **8**(19): p. 9919-9943.
3. Boverhof, D.R., *et al*., *Comparative assessment of nanomaterial definitions and safety evaluation considerations.* Regulatory Toxicology and Pharmacology, 2015. **73**(1): p. 137-150.
4. Cagliani, R., F. Gatto, and G.J.M. Bardi, *Protein adsorption: a feasible method for nanoparticle functionalization?* 2019. **12**(12): p. 1991.
5. Charbgoo, F., *et al*., *Gold nanoparticle should understand protein corona for being a clinical nanomaterial.* 2018. **272**: p. 39-53.
6. Wheeler, K.E., *et al*., *Environmental dimensions of the protein corona.* 2021. **16**(6): p. 617-629.
7. Chen, D., *et al*., *Plasma protein adsorption and biological identity of systemically administered nanoparticles.* 2017. **12**(17): p. 2113-2135.
8. Cagliani, R., F. Gatto, and G. Bardi, *Protein adsorption: a feasible method for nanoparticle functionalization?* Materials, 2019. **12**(12): p. 1991.
9. Rauscher, H., *et al*., *An overview of concepts and terms used in the European Commission's definition of nanomaterial.* Publications Office of the European Union, 2019.
10. Maria, L., J. Moses, and C. Anandharamakrishnan, *Ethical and Regulatory Issues in Applications of Nanotechnology in Food*, in *Food Nanotechnology*. 2019, CRC Press. p. 67-92.
11. Muhammad, S.F., *Nanotechnology Particle characteristic*. 2021, Salahaddin University-Erbil.
12. Li, X., *et al*., *Effects of physicochemical properties of nanomaterials on their toxicity.* Journal of biomedical materials research Part A, 2015. **103**(7): p. 2499-2507.
13. Wen, T., *et al*., *Comparative study of in vitro effects of different nanoparticles at non-cytotoxic concentration on the adherens junction of human vascular endothelial cells.* International journal of nanomedicine, 2019. **14**: p. 4475.
14. Bedi, P. and A. Kaur, *An overview on uses of zinc oxide nanoparticles.* World Journal of Pharmacy and Pharmaceutical Sciences, 2015. **4**(12): p. 1177-1196.

15. Liu, N. and M. Tang, *Toxicity of different types of quantum dots to mammalian cells in vitro: An update review.* Journal of Hazardous Materials, 2020. **399**: p. 122606.
16. Gao, H. and Q. He, *The interaction of nanoparticles with plasma proteins and the consequent influence on nanoparticles behavior.* Expert opinion on drug delivery, 2014. **11**(3): p. 409-420.
17. Grevendonk, L., *et al*., *Mitochondrial oxidative DNA damage and exposure to particulate air pollution in mother-newborn pairs.* Environmental Health, 2016. **15**(1): p. 1-8.
18. Alyani Nezhad, Z., *et al*., *Investigation of the dose enhancement effect of spherical bismuth oxide nanoparticles in external beam radiotherapy.* Nanomedicine Research Journal, 2020. **5**(1): p. 55-62.
19. Gatoo, M.A., *et al*., *Physicochemical properties of nanomaterials: implication in associated toxic manifestations.* BioMed research international, 2014. **2014**.
20. Verma, A. and F. Stellacci, *Effect of surface properties on nanoparticle–cell interactions.* small, 2010. **6**(1): p. 12-21.
21. Leite, Á.J. and J. Mano, *Biomedical applications of natural-based polymers combined with bioactive glass nanoparticles.* Journal of materials chemistry B, 2017. **5**(24): p. 4555-4568.
22. Pooja, D., *et al*., *Optimization of solid lipid nanoparticles prepared by a single emulsification-solvent evaporation method.* Data in brief, 2016. **6**: p. 15-19.
23. Abashkin, V., *et al*., *Prospects of Cationic Carbosilane Dendronized Gold Nanoparticles as Non-viral Vectors for Delivery of Anticancer siRNAs siBCL-xL and siMCL-1.* Pharmaceutics, 2021. **13**(10): p. 1549.
24. Fubini, B., *et al*., *Effect of chemical composition and state of the surface on the toxic response to high aspect ratio nanomaterials.* Nanomedicine, 2011. **6**(5): p. 899-920.
25. Jóźwiak, B., *et al*., *Remarkable thermal conductivity enhancement in carbon-based ionanofluids: effect of nanoparticle morphology.* ACS applied materials & interfaces, 2020. **12**(34): p. 38113.
26. Reshma, V. and P. Mohanan, *Quantum dots: Applications and safety consequences.* Journal of Luminescence, 2019. **205**: p. 287-298.
27. Pietroiusti, A., *et al*., *Low doses of pristine and oxidized single-wall carbon nanotubes affect mammalian embryonic development.* Acs Nano, 2011. **5**(6): p. 4624-4633.
28. Amigoni, L., *et al*., *Impact of Tuning the Surface Charge Distribution on Colloidal Iron Oxide Nanoparticle Toxicity Investigated in Caenorhabditis elegans.* Nanomaterials (Basel), 2021. **11**(6).

29. Sawalha, S.M., E. Ghadhban, and Z.T. Al-Dahan. *Impact of Gold nanoparticles sizes and concentrations on the Rhabdomyosarcoma cells*. in *IOP Conference Series: Materials Science and Engineering*. 2020. IOP Publishing.
30. Griffitt, R.J., *et al*., *Effects of particle composition and species on toxicity of metallic nanomaterials in aquatic organisms.* Environmental Toxicology and Chemistry: An International Journal, 2008. **27**(9): p. 1972-1978.
31. Botelho, M.C., *et al*., *Effects of titanium dioxide nanoparticles in human gastric epithelial cells in vitro.* Biomedicine & Pharmacotherapy, 2014. **68**(1): p. 59-64.
32. Gurr, J.-R., *et al*., *Ultrafine titanium dioxide particles in the absence of photoactivation can induce oxidative damage to human bronchial epithelial cells.* Toxicology, 2005. **213**(1-2): p. 66-73.
33. Qin, Y., *et al*., *Long-term intravenous administration of carboxylated single-walled carbon nanotubes induces persistent accumulation in the lungs and pulmonary fibrosis via the nuclear factor-kappa B pathway.* International journal of nanomedicine, 2017. **12**: p. 263.
34. Patel, J., *et al*., *Carbon Nanotube (CNTs): Structure, Synthesis, Purification, Functionalisation, Pharmacology, Toxicology, Biodegradation and Application as Nanomedicine and Biosensor: Carbon Nanotube (CNTs).* The Journal of Pharmaceutical Sciences and Medicinal Research, 2021. **1**(02): p. 017-044.
35. Sen, R., *et al*., *Synthesis and characterization of nickel ferrite (NiFe2O4) nanoparticles prepared by sol-gel method.* Materials Today: Proceedings, 2015. **2**(4-5): p. 3750-3757.
36. Guller, A.E., *et al*., *Cytotoxicity and non-specific cellular uptake of bare and surface-modified upconversion nanoparticles in human skin cells.* Nano Research, 2015. **8**(5): p. 1546-1562.
37. Alarifi, S., D. Ali, and S. Alkahtani, *Oxidative stress-induced DNA damage by manganese dioxide nanoparticles in human neuronal cells.* BioMed research international, 2017. **2017**.
38. Chawla, J. and A. Kumar, *Ranking carbon-based nanomaterials using cytotoxicity to minimize public health risks.* Int J Environ Eng Manag, 2013. **4**(3): p. 301-308.
39. Fan, Q., *et al*., *Effect of Micelle Encapsulation on Toxicity of CdSe/ZnS and Mn-Doped ZnSe Quantum Dots.* Coatings, 2021. **11**(8): p. 895.
40. Kuo, T.-R., *et al*., *Studies of intracorneal distribution and cytotoxicity of quantum dots: risk assessment of eye exposure.* Chemical research in toxicology, 2011. **24**(2): p. 253-261.

41. Turan, N.B., *et al*., *Nanoparticles in the aquatic environment: Usage, properties, transformation and toxicity—A review.* Process safety and environmental protection, 2019. **130**: p. 238-249.
42. Hitler, L., *et al*., *Mechanism, of biophysicochemical interactions and cellular uptake at the nano-bio interface: a review.* European Journal of Biophysics, 2017. **5**(4): p. 66-78.
43. Kobayashi, K., *et al*., *Effective dispersal of titanium dioxide nanoparticles for toxicity testing.* The Journal of toxicological sciences, 2019. **44**(8): p. 515-521.
44. Suttiponparnit, K., *et al*., *Role of surface area, primary particle size, and crystal phase on titanium dioxide nanoparticle dispersion properties.* Nanoscale Res Lett, 2011. **6**(1): p. 1-8.
45. Gardea-Torresdey, J.L., C.M. Rico, and J.C. White, *Trophic transfer, transformation, and impact of engineered nanomaterials in terrestrial environments.* Environmental science & technology, 2014. **48**(5): p. 2526-2540.
46. Fritz, B.R., *et al*., *Biology by design: from top to bottom and back.* Journal of Biomedicine and Biotechnology, 2010. **2010**.
47. Liu, M., *et al*., *The generation of myricetin–nicotinamide nanococrystals by top down and bottom up technologies.* Nanotechnology, 2016. **27**(39): p. 395601.
48. Wagener, P., *et al*., *Physical fabrication of colloidal ZnO nanoparticles combining wet-grinding and laser fragmentation.* Applied Physics A, 2012. **108**(4): p. 793-799.
49. Habiba, K., *et al*., *Fabrication of nanomaterials by pulsed laser synthesis.* Manufacturing Nanostructures, 2014: p. 263.
50. Li, M., *et al*., *Nanomilling of drugs for bioavailability enhancement: a holistic formulation-process perspective.* Pharmaceutics, 2016. **8**(2): p. 17.
51. Gao, L., *et al*., *Application of drug nanocrystal technologies on oral drug delivery of poorly soluble drugs.* Pharmaceutical research, 2013. **30**(2): p. 307-324.
52. Loh, Z.H., A.K. Samanta, and P.W.S. Heng, *Overview of milling techniques for improving the solubility of poorly water-soluble drugs.* Asian journal of pharmaceutical sciences, 2015. **10**(4): p. 255-274.
53. Mahesh, K.V., S.K. Singh, and M. Gulati, *A comparative study of top-down and bottom-up approaches for the preparation of nanosuspensions of glipizide.* Powder technology, 2014. **256**: p. 436-449.
54. Boldyreva, E., *Mechanochemistry of inorganic and organic systems: what is similar, what is different?* Chemical Society Reviews, 2013. **42**(18): p. 7719-7738.

55. Vinchhi, P., J.K. Patel, and M.M. Patel, *High-Pressure Homogenization Techniques for Nanoparticles*, in *Emerging Technologies for Nanoparticle Manufacturing*. 2021, Springer. p. 263-285.
56. Yadav, K.S. and K. Kale, *High pressure homogenizer in pharmaceuticals: understanding its critical processing parameters and applications.* Journal of Pharmaceutical Innovation, 2020. **15**(4): p. 690-701.
57. Li, Y., *et al*., *Preparation and characterization of paclitaxel nanosuspension using novel emulsification method by combining high speed homogenizer and high pressure homogenization.* International journal of pharmaceutics, 2015. **490**(1-2): p. 324-333.
58. Tehrani, A.A., *et al*., *Formation of nanosuspensions in bottom-up approach: theories and optimization.* DARU Journal of Pharmaceutical Sciences, 2019: p. 1-23.
59. Katakam, P., *et al*., *Top-down and bottom-up approaches in 3D printing technologies for drug delivery challenges.* Critical Reviews™ in Therapeutic Drug Carrier Systems, 2015. **32**(1).
60. Liu, G., J. Li, and S. Deng, *Applications of supercritical anti-solvent process in preparation of solid multicomponent systems.* Pharmaceutics, 2021. **13**(4): p. 475.
61. Swain, S., *et al*., *Nanoparticles for cancer targeting: current and future directions.* Current drug delivery, 2016. **13**(8): p. 1290-1302.
62. Chan, H.-K. and P.C.L. Kwok, *Production methods for nanodrug particles using the bottom-up approach.* Advanced drug delivery reviews, 2011. **63**(6): p. 406-416.
63. Zhang, J., *et al*., *Nanosuspension drug delivery system: preparation, characterization, postproduction processing, dosage form, and application*, in *Nanostructures for Drug Delivery*. 2017, Elsevier. p. 413-443.
64. Jia, X., *et al*., *Modern synthesis strategies for hierarchical zeolites: Bottom-up versus top-down strategies.* Advanced Powder Technology, 2019. **30**(3): p. 467-484.
65. Lee, S.H. and B.-H. Jun, *Silver nanoparticles: synthesis and application for nanomedicine.* International journal of molecular sciences, 2019. **20**(4): p. 865.
66. Lee, S.H., *et al*., *Multifunctional self-assembled monolayers via microcontact printing and degas-driven flow guided patterning.* Scientific reports, 2018. **8**(1): p. 1-8.
67. Gurunathan, S., *et al*., *Comparative assessment of the apoptotic potential of silver nanoparticles synthesized by Bacillus tequilensis and Calocybe indica in MDA-MB-231 human breast cancer cells:*

targeting p53 for anticancer therapy. International journal of nanomedicine, 2015. **10**: p. 4203.
68. Le Ouay, B. and F. Stellacci, *Antibacterial activity of silver nanoparticles: a surface science insight.* Nano today, 2015. **10**(3): p. 339-354.
69. Li, C., *et al*., *In vivo real-time visualization of tissue blood flow and angiogenesis using Ag2S quantum dots in the NIR-II window.* Biomaterials, 2014. **35**(1): p. 393-400.
70. Zhang, X.-F., *et al*., *Silver nanoparticles: synthesis, characterization, properties, applications, and therapeutic approaches.* International journal of molecular sciences, 2016. **17**(9): p. 1534.
71. Yang, Z., H. Liu, and D. Liu, *Spatial regulation of synthetic and biological nanoparticles by DNA nanotechnology.* NPG Asia Materials, 2015. **7**(2): p. e161-e161.
72. Mukherjee, P., *et al*., *Potential therapeutic application of gold nanoparticles in B-chronic lymphocytic leukemia (BCLL): enhancing apoptosis.* Journal of nanobiotechnology, 2007. **5**(1): p. 1-13.
73. Calzolai, L., *et al*., *Protein− nanoparticle interaction: identification of the ubiquitin− gold nanoparticle interaction site.* Nano letters, 2010. **10**(8): p. 3101-3105.
74. López-Marzo, A.M., R. Hoyos-de-la-Torre, and E. Baldrich, *NaNO3/NaCl oxidant and Polyethylene glycol (PEG) capped gold nanoparticles (AuNPs) as a novel green route for AuNPs detection in electrochemical biosensors.* Analytical chemistry, 2018. **90**(6): p. 4010-4018.
75. Hosnedlova, B., *et al*., *Nano-selenium and its nanomedicine applications: a critical review.* International journal of nanomedicine, 2018. **13**: p. 2107.
76. Mohammadifard, N., *et al*., *Trace minerals intake: risks and benefits for cardiovascular health.* Critical reviews in food science and nutrition, 2019. **59**(8): p. 1334-1346.
77. Zambonino, M.C., *et al*., *Green synthesis of selenium and tellurium nanoparticles: current trends, biological properties and biomedical applications.* International Journal of Molecular Sciences, 2021. **22**(3): p. 989.
78. Khurana, A., *et al*., *Therapeutic applications of selenium nanoparticles.* Biomedicine & Pharmacotherapy, 2019. **111**: p. 802-812.
79. Shakibaie, M., *et al*., *Biosynthesis and recovery of selenium nanoparticles and the effects on matrix metalloproteinase-2*

expression. Biotechnology and applied biochemistry, 2010. **56**(1): p. 7-15.
80. Iranifam, M., *et al*., *A novel selenium nanoparticles-enhanced chemiluminescence system for determination of dinitrobutylphenol.* Talanta, 2013. **107**: p. 263-269.
81. Wang, Q. and T.J. Webster, *Nanostructured selenium for preventing biofilm formation on polycarbonate medical devices.* Journal of Biomedical Materials Research Part A, 2012. **100**(12): p. 3205-3210.
82. Nie, T., *et al*., *Facile synthesis of highly uniform selenium nanoparticles using glucose as the reductant and surface decorator to induce cancer cell apoptosis.* Journal of Materials Chemistry B, 2016. **4**(13): p. 2351-2358.
83. Fernández-Llamosas, H., et al., *Biosynthesis of selenium nanoparticles by Azoarcus sp. CIB.* Microbial cell factories, 2016. **15**(1): p. 1-10.
84. Zhai, X., *et al*., *Antioxidant capacities of the selenium nanoparticles stabilized by chitosan.* Journal of nanobiotechnology, 2017. **15**(1): p. 1-12.
85. Tran, P.A., *et al*., *Low cytotoxic trace element selenium nanoparticles and their differential antimicrobial properties against S. aureus and E. coli.* Nanotechnology, 2015. **27**(4): p. 045101.
86. Phan, T.T.V., *et al*., *Chitosan as a stabilizer and size-control agent for synthesis of porous flower-shaped palladium nanoparticles and their applications on photo-based therapies.* Carbohydrate polymers, 2019. **205**: p. 340-352.
87. Sadeghian, S., G.A. Kojouri, and A. Mohebbi, *Nanoparticles of selenium as species with stronger physiological effects in sheep in comparison with sodium selenite.* Biological Trace Element Research, 2012. **146**(3): p. 302-308.
88. Kojouri, G.A. and S. Sharifi, *Preventing effects of nano-selenium particles on serum concentration of blood urea nitrogen, creatinine, and total protein during intense exercise in donkey.* Journal of equine veterinary science, 2013. **33**(8): p. 597-600.
89. Estevez, H., *et al*., *Effects of chitosan-stabilized selenium nanoparticles on cell proliferation, apoptosis and cell cycle pattern in HepG2 cells: comparison with other selenospecies.* Colloids and Surfaces B: Biointerfaces, 2014. **122**: p. 184-193.
90. Kazemi, M., *et al*., *Evaluation of Antifungal and Photocatalytic Activities of Gelatin-Stabilized Selenium Oxide Nanoparticles.* Journal of Inorganic and Organometallic Polymers and Materials, 2020: p. 1-9.

91. Yazdi, M.H., *et al*., *Selenium nanoparticle-enriched Lactobacillus brevis causes more efficient immune responses in vivo and reduces the liver metastasis in metastatic form of mouse breast cancer.* DARU Journal of Pharmaceutical Sciences, 2013. **21**(1): p. 1-9.
92. Wang, H., J. Zhang, and H. Yu, *Elemental selenium at nano size possesses lower toxicity without compromising the fundamental effect on selenoenzymes: comparison with selenomethionine in mice.* Free Radical Biology and Medicine, 2007. **42**(10): p. 1524-1533.
93. Piacenza, E., *et al*., *Antimicrobial activity of biogenically produced spherical Se-nanomaterials embedded in organic material against Pseudomonas aeruginosa and Staphylococcus aureus strains on hydroxyapatite-coated surfaces.* Microbial biotechnology, 2017. **10**(4): p. 804-818.
94. Cremonini, E., *et al*., *Biogenic selenium nanoparticles: characterization, antimicrobial activity and effects on human dendritic cells and fibroblasts.* Microbial biotechnology, 2016. **9**(6): p. 758-771.
95. Kheradmand, E., *et al*., *The antimicrobial effects of selenium nanoparticle-enriched probiotics and their fermented broth against Candida albicans.* DARU Journal of Pharmaceutical Sciences, 2014. **22**(1): p. 1-6.
96. Beheshti, N., *et al*., *Efficacy of biogenic selenium nanoparticles against Leishmania major: in vitro and in vivo studies.* Journal of Trace Elements in Medicine and Biology, 2013. **27**(3): p. 203-207.
97. Zhang, S.-Y., *et al*., *Synthesis of selenium nanoparticles in the presence of polysaccharides.* Materials Letters, 2004. **58**(21): p. 2590-2594.
98. Shoeibi, S. and M. Mashreghi, *Biosynthesis of selenium nanoparticles using Enterococcus faecalis and evaluation of their antibacterial activities.* Journal of Trace Elements in Medicine and Biology, 2017. **39**: p. 135-139.
99. Séby, F., *et al*., *A critical review of thermodynamic data for selenium species at 25 C.* Chemical Geology, 2001. **171**(3-4): p. 173-194.
100. Bounache, K., *et al*., *Visible Light Hydrogen Evolution over α-MoO3 and α-MoO3/ZnO Hetero-Junction.* Open Journal of Physical Chemistry, 2021. **11**(3): p. 144-156.
101. Paul, M., M. Dhanasekar, and S.V. Bhat, *Silver doped h-MoO3 nanorods for sonophotocatalytic degradation of organic pollutants in ambient sunlight.* Applied Surface Science, 2017. **418**: p. 113-118.
102. Sharma, R., *et al*., *Controlled growth of α-MoO3 nanostructures with enhanced optical and electrochemical properties without*

capping agents. Ceramics International, 2020. **46**(14): p. 23084-23097.
103. Zhang, Z., *et al*., *Synthesis of MoO3/V2O5/C composite as novel anode for Li-ion battery application.* Journal of nanoscience and nanotechnology, 2020. **20**(5): p. 2911-2916.
104. White, R.T., E.S. Thibau, and Z.-H. Lu, *Interface structure of MoO 3 on organic semiconductors.* Scientific reports, 2016. **6**(1): p. 1-9.
105. Kumar, K.U., *et al*., *Hybrid electrochromic device with Tungsten oxide (WO3-x) and nafion membrane: performance with varying tungsten oxide thickness.* arXiv preprint arXiv:1610.08807, 2016.
106. Kumar, A. and G. Pandey, *Synthesis, characterization, effect of temperature on band gap energy of molybdenum oxide nano rods and their antibacterial activity.* American Journal of Applied and Industrial Chemistry, 2017. **3**(3): p. 38-42.
107. Seisenbaeva, G.A., *et al*., *Thermal decomposition of the methoxide complexes MoO (OMe) 4, Re4O6 (OMe) 12 and (Re1− xMox) O6 (OMe) 12 (0.24≤ x≤ 0.55).* Materials chemistry and physics, 2004. **87**(1): p. 142-148.
108. Rajagopal, R. and K.-S. Ryu, *Influence of rare earth elements on porosity controlled synthesis of MnO2 nanostructures for supercapacitor applications.* Electrochimica Acta, 2018. **265**: p. 532-546.
109. Bora, P.J., *et al*., *Morphology controllable microwave absorption property of polyvinylbutyral (PVB)-MnO2 nanocomposites.* Composites Part B: Engineering, 2018. **132**: p. 188-196.
110. Khalilnejad, M., T. Mortezazadeh, and R. Ghasemi Shayan, *Application of Manganese Oxide (MnO) nanoparticles in multimodal molecular imaging and cancer therapy: A review.* Nanomedicine Journal, 2021. **8**(3): p. 166-178.
111. Castro, K.C.d., J.M. Costa, and M.G.N. Campos, *Drug-loaded polymeric nanoparticles: a review.* International Journal of Polymeric Materials and Polymeric Biomaterials, 2020: p. 1-13.
112. Zhu, S., *et al*., *Low-charge-carrier-scattering three-dimensional α-MnO2/β-MnO2 networks for ultra-high-rate asymmetrical supercapacitors.* ACS Applied Energy Materials, 2018. **2**(2): p. 1051-1059.
113. Selim, M.S., *et al*., *Superhydrophobic coating of silicone/β–MnO2 nanorod composite for marine antifouling.* Colloids and Surfaces A: Physicochemical and Engineering Aspects, 2019. **570**: p. 518-530.
114. Duan, Y., *et al*., *Morphology-controlled synthesis and microwave absorption properties of β-MnO2 microncube with rectangular pyramid.* Materials Characterization, 2016. **112**: p. 206-212.

115. Jiang, L., *Catalytic Performance and Characterization of Zn-doped Cryptomelane-type Manganese Dioxide For Ethanol Oxidation*. 2012, Miami University.
116. Xu, K., *et al*., *Hierarchical hollow MnO2 nanofibers with enhanced supercapacitor performance.* Journal of colloid and interface science, 2018. **513**: p. 448-454.
117. Petkov, V., *Nanostructure by high-energy X-ray diffraction.* Materials Today, 2008. **11**(11): p. 28-38.
118. Shnoudeh, A.J., *et al*., *Synthesis, characterization, and applications of metal nanoparticles*, in *Biomaterials and bionanotechnology*. 2019, Elsevier. p. 527-612.
119. Zhen, X., *et al*., *Ultralong Phosphorescence of Water-Soluble Organic Nanoparticles for In Vivo Afterglow Imaging.* Adv Mater, 2017. **29**(33).
120. Li, K. and B. Liu, *Polymer-encapsulated organic nanoparticles for fluorescence and photoacoustic imaging.* Chem Soc Rev, 2014. **43**(18): p. 6570-97.
121. Mahajan, P.G., *et al*., *Intracellular imaging of zinc ion in living cells by fluorescein based organic nanoparticles.* Sensors and Actuators B: Chemical, 2018. **267**: p. 119-128.
122. Montaseri, H., C.A. Kruger, and H. Abrahamse, *Review: Organic nanoparticle based active targeting for photodynamic therapy treatment of breast cancer cells.* Oncotarget, 2020. **11**(22): p. 2120-2136.
123. McClements, D.J.J.P.i.l.r., *Edible lipid nanoparticles: digestion, absorption, and potential toxicity.* 2013. **52**(4): p. 409-423.
124. Rajendran, S.R., C.C. Udenigwe, and R.Y.J.F.i.c. Yada, *Nanochemistry of protein-based delivery agents.* 2016. **4**: p. 31.
125. López-Lorente, A., B. Simonet, and M. Valcárcel, *Analytical potential of hybrid nanoparticles.* Analytical and bioanalytical chemistry, 2011. **399**(1): p. 43-54.
126. Sailor, M.J. and J.H. Park, *Hybrid nanoparticles for detection and treatment of cancer.* Advanced materials, 2012. **24**(28): p. 3779-3802.
127. Hante, N.K., C. Medina, and M.J. Santos-Martinez, *Effect on platelet function of metal-based nanoparticles developed for medical applications.* Frontiers in cardiovascular medicine, 2019. **6**: p. 139.
128. Guo, J., *et al*., *Gold nanoparticles enlighten the future of cancer theranostics.* International journal of nanomedicine, 2017. **12**: p. 6131.

129. Fernández-Barahona, I., *et al*., *Iron oxide nanoparticles: an alternative for positive contrast in magnetic resonance imaging.* Inorganics, 2020. **8**(4): p. 28.
130. Zhu, L., *et al*., *Magnetic nanoparticles for precision oncology: theranostic magnetic iron oxide nanoparticles for image-guided and targeted cancer therapy.* Nanomedicine, 2017. **12**(1): p. 73-87.
131. Pareek, V., *et al*., *Silver nanoparticles induce a triclosan-like antibacterial action mechanism in multi-drug resistant Klebsiella pneumoniae.* Frontiers in microbiology, 2021. **12**: p. 183.
132. Gul, A., *et al*., *Rutin and rutin-conjugated gold nanoparticles ameliorate collagen-induced arthritis in rats through inhibition of NF-κB and iNOS activation.* International immunopharmacology, 2018. **59**: p. 310-317.
133. Al-Trad, B., *et al*., *Effect of gold nanoparticles treatment on the testosterone-induced benign prostatic hyperplasia in rats.* International journal of nanomedicine, 2019. **14**: p. 3145.
134. Liu, X., *et al*., *Comprehensive understanding of magnetic hyperthermia for improving antitumor therapeutic efficacy.* Theranostics, 2020. **10**(8): p. 3793.
135. Wang, H., *et al*., *Molecular Studies of Peptide Assemblies and Related Applications in Tumor Therapy and Diagnosis*, in *Nanotechnology in Regenerative Medicine and Drug Delivery Therapy*. 2020, Springer. p. 255-286.
136. Polo, E., *et al*., *Magnetic nanoparticles for cancer therapy and bioimaging*, in *Nanooncology*. 2018, Springer. p. 239-279.
137. Asl, H.M., *Applications of nanoparticles in magnetic resonance imaging: a comprehensive review.* Asian Journal of Pharmaceutics (AJP): Free full text articles from Asian J Pharm, 2017. **11**(01).
138. Schubert, J. and M. Chanana, *Coating matters: Review on colloidal stability of nanoparticles with biocompatible coatings in biological media, living cells and organisms.* Current medicinal chemistry, 2019. **25**(35): p. 4556.
139. Natarajan, S., *et a*l., *Multifunctional magnetic iron oxide nanoparticles: diverse synthetic approaches, surface modifications, cytotoxicity towards biomedical and industrial applications.* BMC Materials, 2019. **1**(1): p. 1-22.
140. Mustafa, S., V.K. Devi, and R.S. Pai, *Effect of PEG and water-soluble chitosan coating on moxifloxacin-loaded PLGA long-circulating nanoparticles.* Drug delivery and translational research, 2017. **7**(1): p. 27-36.
141. Patel, Y.S., N. Das, and S. Das, *Novel Targeting Approaches of Nanoparticles for Anticancers Drug Delivery: A Focused Review.*

World Journal of Pharmaceutical and Medical Research, 2019. **5**(9): p. 44.
142. Zhang, M., *et al*., *Nanotechnology-based combination therapy for overcoming multidrug-resistant cancer*. Cancer biology & medicine, 2017. **14**(3): p. 212.
143. Toscano Guerra, E.M., *Detección de ácido pirazinoico como biomarcador de resistencia a pirazinamida en Mycobacterium tuberculosis mediante dos inmunoensayos empleando nanopartículas magnéticas, tmRNA y RpsA.* 2018.
144. Röhm, S., A. Krämer, and S. Knapp, *Function, structure and topology of protein kinases*, in *Proteinkinase Inhibitors*. 2020, Springer. p. 1-24.
145. Ponraj, T.E., *et al*., *Deterministic functions for measuring human protein structural variations with merit based ensemble learning scheme for native classification.* 2021: p. 1-13.
146. Meyer, L.E., *et al*., *Development of Ionic Liquid-Water-Based Thermomorphic Solvent (TMS)-Systems for Biocatalytic Reactions.* Biotechnology journal, 2019. **14**(10): p. 1900215.
147. Tadros, T.F., *15. Proteins as emulsifiers and their interaction with polysaccharides*, in *Industrial Applications II*. 2017, De Gruyter. p. 305-312.
148. Li-Chan, E. and I. Lacroix, *Properties of proteins in food systems: an introduction*, in *Proteins in food processing*. 2018, Elsevier. p. 1-25.
149. Ewalt, K.L., P. Schimmel, and J.M. Manning, *Protein.* 2021.
150. Singh, N., *et al*., *In vivo protein corona on nanoparticles: does the control of all material parameters orient the biological behavior?* 2021. **3**(5): p. 1209-1229.
151. Galmarini, S., *et al*., *Beyond unpredictability: the importance of reproducibility in understanding the protein corona of nanoparticles.* 2018. **29**(10): p. 3385-3393.
152. Haggstrom, M., *Reference ranges for estradiol, progesterone, luteinizing hormone and follicle-stimulating hormone during the menstrual cycle.* WikiJournal of Medicine, 2014. **1**(1): p. 1-5.
153. Abdalmageed, R.A.A., *Assessment of Serum Gonadotropin (LH and FSH) Levels among Sudanese Women with Polycystic Ovary Syndrome*. 2020, Sudan University of Science & Technology.
154. Ciocca, G., *et al*., *Is testosterone a food for the brain?* Sexual medicine reviews, 2016. **4**(1): p. 15-25.
155. Zehravi, M., *et al*., *Polycystic ovary syndrome and infertility: An update.* 2021.

156. May, T., *et al*., *Overlap of autism and conditions associated with atypical sex hormone levels or response: A systematic review and meta-analysis.* 2021. **80**: p. 101693.
157. Stamatiades, G.A. and U.B. Kaiser, *Gonadotropin regulation by pulsatile GnRH: signaling and gene expression.* Molecular and cellular endocrinology, 2018. **463**: p. 131-141.
158. Desai, N., *et al*., *Female and male gametogenesis*, in *Clinical reproductive medicine and surgery*. 2022, Springer. p. 23-54.
159. Surekha, G. and M. Nagarajan, *Follicle Stimulating Hormone Receptor and Estrogen Receptor Gene Polymorphism in Ovarian Function-Review.* Biomedical Research, 2018. **3**: p. 01-05.
160. Plant, T. and G. Marshall, *The Functional Significance of FSH in Spermatogenesis and the Control of Its Secretion in Male Primates.* Endocrine reviews, 2002. **22**: p. 764-86.
161. Zhu, D., *et al*., *Extragonadal effects of follicle-stimulating hormone on osteoporosis and cardiovascular disease in women during menopausal transition.* Trends in Endocrinology & Metabolism, 2018. **29**(8): p. 571-580.
162. Lee, M.W., *The Detrimental Side Effects of Retinol: Beyond Beauty Products.* 2020.
163. Kobayashi, N., *Comparative Study of a Sustainable and Resilient Towns/Farm Parks in the UK and Japan.* 2021.
164. Mahameed, A., *Comparative Study between Commercial Charcoal and Asphodelus ramosus Tuber Derived Activated Carbons for Adsorption of Heavy metals from Aqueous Solution*. 2017, An-Najah National University.
165. Barbosa, M. and M.C.L. Martins, *Peptides and proteins as biomaterials for tissue regeneration and repair*. 2017: Woodhead Publishing.
166. García-Álvarez, R. and M. Vallet-Regí, *Hard and Soft Protein Corona of Nanomaterials: Analysis and Relevance.* Nanomaterials, 2021. **11**(4): p. 888.
167. Monopoli, M.P., *et al*., *Biomolecular Coronas Provide the Biological Identity of Nanosized Materials*, in *Nano-Enabled Medical Applications*. 2020, Jenny Stanford Publishing. p. 205-229.
168. Wolfram, J., et al., *The nano-plasma interface: Implications of the protein corona.* Colloids and Surfaces B: Biointerfaces, 2014. **124**: p. 17-24.
169. Van Hong Nguyen, B.-J.L., *Protein corona: a new approach for nanomedicine design.* International journal of nanomedicine, 2017. **12**: p. 3137.

170. Pederzoli, F., *et al*., *Protein corona and nanoparticles: how can we investigate on?* Wiley Interdisciplinary Reviews: Nanomedicine and Nanobiotechnology, 2017. **9**(6): p. e1467.
171. Jordan, E.E., *In Vitro Assessment of Dendritic Cell Activation and Phenotypic Response to Gold Nanoparticle Treatments.* 2019.
172. Ellis, L.-J.A. and I. Lynch, *Mechanistic insights into toxicity pathways induced by nanomaterials in Daphnia magna from analysis of the composition of the acquired protein corona.* Environmental Science: Nano, 2020. **7**(11): p. 3343-3359.
173. Foroozandeh, P. and A.A. Aziz, *Merging worlds of nanomaterials and biological environment: factors governing protein corona formation on nanoparticles and its biological consequences.* Nanoscale research letters, 2015. **10**(1): p. 1-12.
174. Saptarshi, S.R., A. Duschl, and A.L. Lopata, *Interaction of nanoparticles with proteins: relation to bio-reactivity of the nanoparticle.* Journal of nanobiotechnology, 2013. **11**(1): p. 1-12.
175. Shannahan, J.H., *et al*., *Silver nanoparticle protein corona composition in cell culture media.* PloS one, 2013. **8**(9): p. e74001.
176. Rashad, M.M., *et al*., *Bovine serum albumin/chitosan-nanoparticle bio-complex; spectroscopic study and in vivo toxicological–Hypersensitivity evaluation.* Spectrochimica Acta Part A: Molecular and Biomolecular Spectroscopy, 2021. **253**: p. 119582.
177. Bai, J., *et al*., *Synthesis of novel hyper-cross-linked chiral porous polymers and their applications in enantioselective adsorption of amino acids.* Microporous and Mesoporous Materials, 2020. **294**: p. 109892.
178. Marczewski, A.W., *Analysis of kinetic Langmuir model. Part I: integrated kinetic Langmuir equation (IKL): a new complete analytical solution of the Langmuir rate equation.* Langmuir, 2010. **26**(19): p. 15229-15238.
179. Dods, S.R., *Characterising electrospun nanofibre adsorbents for bioprocessing*. 2016, UCL (University College London).
180. Andrade, J.D., *Surface and Interfacial Aspects of Biomedical Polymers: Volume 1 Surface Chemistry and Physics*. 2012: Springer Science & Business Media.
181. Yang, M., *The effect of posttranslational modifications on protein aggregation, morphology, and toxicity*. 2016, Michigan Technological University.
182. van der Vegt, N.F. and D. Nayar, *The hydrophobic effect and the role of cosolvents.* The Journal of Physical Chemistry B, 2017. **121**(43): p. 9986-9998.

183. Marzun, G., *et al*., *Adsorption of colloidal platinum nanoparticles to supports: charge transfer and effects of electrostatic and steric interactions.* Langmuir, 2014. **30**(40): p. 11928-11936.
184. Manickum, T. and W. John, *The current preference for the immuno-analytical ELISA method for quantitation of steroid hormones (endocrine disruptor compounds) in wastewater in South Africa.* Analytical and bioanalytical chemistry, 2015. **407**(17): p. 4949-4970.
185. Lu, Y., *et al*., *ELISA-based sensing in food safety and quality analysis*, in *Sensing Techniques for Food Safety and Quality Control*. 2017, Royal Society of Chemistry. p. 141-163.
186. Steve, D.L., *Analytical techniques used in the development of quantitative and qualitative assays for pharmaceutical and biological products in animal health.* 2017.
187. McElhaney, J., *ELISA and Multiplex Technologies for Cytokine Measurement in Inflammation and Aging Research.*
188. Lequin, R.M., *Enzyme immunoassay (EIA)/enzyme-linked immunosorbent assay (ELISA).* Clinical chemistry, 2005. **51**(12): p. 2415-2418.
189. Alhajj, M. and A.J.S. Farhana, *Enzyme linked immunosorbent assay*. 2021.
190. Lequin, R.M.J.C.c., *Enzyme immunoassay (EIA)/enzyme-linked immunosorbent assay (ELISA).* 2005. **51**(12): p. 2415-2418.
191. Gan, S.D. and K.R. Patel, *Enzyme immunoassay and enzyme-linked immunosorbent assay.* J Invest Dermatol, 2013. **133**(9): p. e12.
192. Azziz, R., *et al*., *Polycystic ovary syndrome.* Nature reviews Disease primers, 2016. **2**(1): p. 1-18.
193. Escobar-Morreale, H.F., *Polycystic ovary syndrome: definition, aetiology, diagnosis and treatment.* Nature Reviews Endocrinology, 2018. **14**(5): p. 270-284.
194. Alwahab, U.A., K.M. Pantalone, and B. Burguera, *A ketogenic diet may restore fertility in women with polycystic ovary syndrome: a case series.* AACE Clinical Case Reports, 2018. **4**(5): p. e427-e431.
195. Mahesh, V., *Hormone secretion and steroidogenesis in the polycystic ovary syndrome*, in *Steroid converting enzymes and diseases*. 2019, De Gruyter. p. 97-146.
196. Al-Janabi, L.M., *Comparative Study of Hormonal and IL-6 Levels Among Infertile Women With Polycystic Ovary Syndrome and Healthy Women.* INTERNATIONAL JOURNAL OF PHARMACEUTICAL QUALITY ASSURANCE, 2019. **10**(04): p. 601-604.
197. Franks, S., *Polycystic ovary syndrome.* Medicine, 2013. **41**(10): p. 553-556.

198. Copperman, A.B., D.E. Stein, and R.S. Corfman, *Induction of Monofolliculogenesis in Patients with Polycystic Ovary Syndrome.* Manual of Ovulation Induction & Ovarian Stimulation Protocols, 2016: p. 323.
199. Gowtham Kumar, S. and V. Sindhu, *Genomic Association of Polycystic Ovarian Syndrome: Single-Nucleotide Polymorphisms and Their Role in Disease Progression.* Computation in BioInformatics: Multidisciplinary Applications, 2021: p. 245-263.
200. Lanes, A., *Pregnancy and Neonatal Outcomes Associated with the Use of Assisted Reproductive Technologies*. 2017, Université d'Ottawa/University of Ottawa.
201. Balen, A.H., *et al*., *Ultrasound assessment of the polycystic ovary: international consensus definitions.* Human reproduction update, 2003. **9**(6): p. 505-514.
202. Hart, R., M. Hickey, and S. Franks, *Definitions, prevalence and symptoms of polycystic ovaries and polycystic ovary syndrome.* Best Practice & Research Clinical Obstetrics & Gynaecology, 2004. **18**(5): p. 671-683.
203. Panidis, D., *et al*., *Associations of menstrual cycle irregularities with age, obesity and phenotype in patients with polycystic ovary syndrome.* Hormones, 2015. **14**(3): p. 431-437.
204. De Leo, V., *et al*., *Genetic, hormonal and metabolic aspects of PCOS: an update.* Reproductive Biology and Endocrinology, 2016. **14**(1): p. 1-17.
205. Sadeeqa, S., *et al*., *PREVALENCE AND MANAGEMENT OF POLYCYSTIC OVARY SYNDROME AND ITS ASSOCIATION WITH DEMOGRAPHICS.* PAFMJ, 2020. **70**(2): p. 498-502.
206. Pandurevic, S., *et al*., *Body mass index rather than the phenotype impacts precocious ultrasound cardiovascular risk markers in polycystic ovary syndrome.* European Journal of Endocrinology, 2020. **1**(aop).
207. Adefris, M. and E. Fekadu, *Postmenopausal mild hirsutism and hyperandrogenemia due to granulosa cell tumor of the ovary: a case report.* Journal of medical case reports, 2017. **11**(1): p. 1-4.
208. Osuka, S., *et al*., *Kisspeptin in the hypothalamus of 2 rat models of polycystic ovary syndrome.* Endocrinology, 2017. **158**(2): p. 367-377.
209. Zehra, B. and A. Khursheed, *Polycystic ovarian syndrome: symptoms, treatment and diagnosis: a review.* J Pharmacogn Phytochem, 2018. **7**: p. 875-880.
210. Pezza, M. and V. Carlomagno, *Inositol in women suffering from acne and PCOS: a randomized study.* Global Dermatology, 2017. **4**(1).

211. Ebersole, A.M. and A.E. Bonny, *Diagnosis and treatment of polycystic ovary syndrome in adolescent females.* Clinical obstetrics and gynecology, 2020. **63**(3): p. 544-552.
212. Dedov, I., *et al*., *The prevalence and clinical features of polycystic ovary syndrome in a Moscow population.* Problems of Endocrinology, 2010. **56**(4): p. 3-8.
213. abdul Razak hassan al-sanjary, A., *Effect of simvastatin and combined oral contraceptive pills in the treatment of polycystic ovary syndrome.* ultrasound, 2016. **6**(8): p. 9.
214. Wolf, W.M., *et al*., *Geographical prevalence of polycystic ovary syndrome as determined by region and race/ethnicity.* International journal of environmental research and public health, 2018. **15**(11): p. 2589.
215. Deswal, R., *et al*., *The prevalence of polycystic ovary syndrome: a brief systematic review.* Journal of Human Reproductive Sciences, 2020. **13**(4): p. 261.
216. Conway, G., *et al*., *The polycystic ovary syndrome: a position statement from the European Society of Endocrinology.* European journal of endocrinology, 2014. **171**(4): p. P1-P29.
217. Williams, T., R. Mortada, and S. Porter, *Diagnosis and treatment of polycystic ovary syndrome.* American family physician, 2016. **94**(2): p. 106-113.
218. Kazemi, M., *et al*., *Evaluation of antifungal and photocatalytic activities of gelatin-stabilized selenium oxide nanoparticles.* Journal of Inorganic and Organometallic Polymers and Materials, 2020. **30**(8): p. 3036-3044.
219. Yao, X., *et al*., *Immobilizing highly catalytically molybdenum oxide nanoparticles on graphene-analogous BN: stable heterogeneous catalysts with enhanced aerobic oxidative desulfurization performance.* Industrial & Engineering Chemistry Research, 2018. **58**(2): p. 863-871.
220. Chen, S., *et al*., *Shape-controlled synthesis of one-dimensional MnO2 via a facile quick-precipitation procedure and its electrochemical properties.* Crystal Growth & Design, 2009. **9**(10): p. 4356-4361.
221. Xu, Y., *et al*., *Mesoporous composite nickel cobalt oxide/graphene oxide synthesized via a template-assistant co-precipitation route as electrode material for supercapacitors.* Journal of Power Sources, 2016. **306**: p. 742-752.
222. Mizwari, Z.M., A.A. Oladipo, and E. Yilmaz, *Chitosan/metal oxide nanocomposites: synthesis, characterization, and antibacterial activity.* International Journal of Polymeric Materials and Polymeric Biomaterials, 2021. **70**(6): p. 383-391.

223. Leoni, M., *The Scherrer formula and integral-breadth methods.* 2019.
224. Buldu, D.G., *A Thesis Submitted to The Graduate School of Engineering and Sciences of*. 2017, İzmir Institute of Technology.
225. Khan, S.A., *et al*., *Fourier transform infrared spectroscopy: fundamentals and application in functional groups and nanomaterials characterization*, in *Handbook of Materials Characterization*. 2018, Springer. p. 317-344.
226. Skoog, D.A., F.J. Holler, and S.R. Crouch, *Principles of instrumental analysis*. 2017: Cengage learning.
227. Furst, E.M. and T.M. Squires, *Microrheology*. 2017: Oxford University Press.
228. Bhattacharjee, S., *DLS and zeta potential–what they are and what they are not?* Journal of controlled release, 2016. **235**: p. 337-351.
229. Das, S., *et al*., *Formulation design, preparation and physicochemical characterizations of solid lipid nanoparticles containing a hydrophobic drug: effects of process variables.* Colloids and surfaces b: biointerfaces, 2011. **88**(1): p. 483-489.
230. Christopherson, R., *Polycystic Ovary Syndrome Metabolic Comorbidities: A Critical Appraisal of the Evidence With Practice Recommendations.* 2016.
231. Meeting, W.E.C.o.B.S. and W.H. Organization, *WHO Expert Committee on Biological Standardization: Sixtieth Report*. Vol. 977. 2013: World Health Organization.
232. Uddin, M., M. Islam, and M. Abedin, *Adsorption of phenol from aqueous solution by water hyacinth ash.* ARPN Journal of engineering and applied sciences, 2007. **2**(2): p. 11-17.
233. Bai, K., *et al*., *Preparation and antioxidant properties of selenium nanoparticles-loaded chitosan microspheres.* International journal of nanomedicine, 2017. **12**: p. 4527.
234. Sheikhalipour, M., *et al*., *Chitosan–selenium nanoparticle (Cs–Se NP) foliar spray alleviates salt stress in bitter melon.* Nanomaterials, 2021. **11**(3): p. 684.
235. Das, M.P., *et al*., *Extraction and characterization of gelatin: a functional biopolymer.* Int. J. Pharm. Pharm. Sci, 2017. **9**(239): p. 10.22159.
236. Srivastava, N. and M. Mukhopadhyay, *Biosynthesis and structural characterization of selenium nanoparticles mediated by Zooglea ramigera.* Powder technology, 2013. **244**: p. 26-29.
237. Dos Santos, T.C., *et al*., *Manufacture and characterization of chitosan/PLGA nanoparticles nanocomposite buccal films.* Carbohydrate polymers, 2017. **173**: p. 638-644.

238. Yusof, N.A.A., N.M. Zain, and N. Pauzi, *Synthesis of ZnO nanoparticles with chitosan as stabilizing agent and their antibacterial properties against Gram-positive and Gram-negative bacteria.* International journal of biological macromolecules, 2019. **124**: p. 1132-1136.
239. Zook, J.M., *et al*., *Stable nanoparticle aggregates/agglomerates of different sizes and the effect of their size on hemolytic cytotoxicity.* Nanotoxicology, 2011. **5**(4): p. 517-530.
240. Bantz, C., *et al*., *The surface properties of nanoparticles determine the agglomeration state and the size of the particles under physiological conditions.* Beilstein journal of nanotechnology, 2014. **5**(1): p. 1774-1786.
241. Abureesh, M.A., A.A. Oladipo, and M. Gazi, *Facile synthesis of glucose-sensitive chitosan–poly (vinyl alcohol) hydrogel: Drug release optimization and swelling properties.* International journal of biological macromolecules, 2016. **90**: p. 75-80.
242. Bahramzadeh, E., E. Yilmaz, and T. Adali, *Chitosan-graft-poly (N-hydroxy ethyl acrylamide) copolymers: Synthesis, characterization and preliminary blood compatibility in vitro.* International journal of biological macromolecules, 2019. **123**: p. 1257-1266.
243. Abureesh, M.A., *et al*., *Engineered mixed oxide-based polymeric composites for enhanced antimicrobial activity and sustained release of antiretroviral drug.* International journal of biological macromolecules, 2018. **116**: p. 417-425.
244. Thanh, N.T., N. Maclean, and S. Mahiddine, *Mechanisms of nucleation and growth of nanoparticles in solution.* Chemical reviews, 2014. **114**(15): p. 7610-7630.
245. Pomogailo, A.D. and G.I. Dzhardimalieva, *Nanostructured materials preparation via condensation ways*. 2014: Springer.
246. Elci, S.G., *et al*., *Surface charge controls the suborgan biodistributions of gold nanoparticles.* ACS nano, 2016. **10**(5): p. 5536-5542.
247. Mobasherat Jajroud, S.Y., et al., *Human hemoglobin adsorption onto colloidal cerium oxide nanoparticles: a new model based on zeta potential and spectroscopy measurements.* Journal of Biomolecular Structure and Dynamics, 2018. **36**(11): p. 2908-2916.
248. Felbeck, T., *et al*., *Monitoring of nanoclay–protein adsorption isotherms via fluorescence techniques.* Colloids and Surfaces B: Biointerfaces, 2017. **157**: p. 373-380.
249. Norde, W., W. Tan, and L. Koopal, *Protein adsorption at solid surfaces and protein complexation with humic acids.* Revista de la ciencia del suelo y nutrición vegetal, 2008. **8**(ESPECIAL): p. 64-74.

250. Rodler, A., *et al*., *Calorimetry for studying the adsorption of proteins in hydrophobic interaction chromatography.* Preparative Biochemistry and Biotechnology, 2019. **49**(1): p. 1-20.
251. Tao, K., *et al*., *How amylose molecular fine structure of rice starch affects functional properties.* Carbohydrate polymers, 2019. **204**: p. 24-31.
252. Hoque, M.A., *et al*., *Influence of salt and temperature on the interaction of bovine serum albumin with cetylpyridinium chloride: Insights from experimental and molecular dynamics simulation.* Journal of Molecular Liquids, 2018. **260**: p. 121-130.
253. Ashbaugh, H.S., M. Vats, and S. Garde, *Bridging Gaussian Density Fluctuations from Microscopic to Macroscopic Volumes: Applications to Non-Polar Solute Hydration Thermodynamics.* The Journal of Physical Chemistry B, 2021. **125**(29): p. 8152-8164.
254. Kinoshita, M. and T. Yoshidome, *Molecular origin of the negative heat capacity of hydrophilic hydration.* The Journal of chemical physics, 2009. **130**(14): p. 04B612.
255. Wu, C., *et al*., *Probing the protein conformation and adsorption behaviors in nanographene oxide-protein complexes.* Journal of nanoscience and nanotechnology, 2014. **14**(3): p. 2591-2598.
256. Goldenzweig, A. and S.J. Fleishman, *Principles of protein stability and their application in computational design.* Annual review of biochemistry, 2018. **87**: p. 105-129.
257. Pace, C.N., J.M. Scholtz, and G.R. Grimsley, *Forces stabilizing proteins.* FEBS letters, 2014. **588**(14): p. 2177-2184.
258. Hao, S., *et al*., *Protein folding mechanism revealed by single-molecule force spectroscopy experiments.* Biophysics Reports, 2021. **7**(5): p. 399-412.
259. Zelentsov, V., T. Datsko, and E. Dvornikova, *Adsorption Models For Treatment Of Experimental Data On Removal Fluorine From Water By Oxihydroxidesof Aluminum.* Romai Journal8, 2012. **1**: p. 209-215.
260. Piccin, J.S., *et al*., *Adsorption isotherms in liquid phase: experimental, modeling, and interpretations*, in *Adsorption processes for water treatment and purification*. 2017, Springer. p. 19-51.
261. Roach, P., D. Farrar, and C.C. Perry, *Interpretation of protein adsorption: surface-induced conformational changes.* Journal of the American Chemical Society, 2005. **127**(22): p. 8168-8173.
262. Hadži, S. and J. Lah, *Origin of heat capacity increment in DNA folding: The hydration effect.* Biochimica et Biophysica Acta (BBA)-General Subjects, 2021. **1865**(1): p. 129774.

263. Chalikian, T.V., *Does the release of hydration water come with a Gibbs energy contribution?* The Journal of Chemical Thermodynamics, 2021. **158**: p. 106409.
264. Di Marco, M., *et al*., *Overview of the main methods used to combine proteins with nanosystems: absorption, bioconjugation, and encapsulation.* International journal of nanomedicine, 2010. **5**: p. 37.
265. Parveen, R., T.N. Shamsi, and S. Fatima, *Nanoparticles-protein interaction: Role in protein aggregation and clinical implications.* International journal of biological macromolecules, 2017. **94**: p. 386-395.
266. Özdokur, K.V., *et al*., *Development of pulsed deposited manganese and molybdenum oxide surfaces decorated with platinum nanoparticles and their catalytic application for formaldehyde oxidation.* International Journal of Hydrogen Energy, 2016. **41**(14): p. 5927-5933.
267. KUMAR, A. and G. PANDEY, *Photocatalytic Activity of Co: TiO2 Nanocomposites and their Application in Photodegradation of Acetic Acid.* Chemical Science, 2017. **6**(3): p. 385-392.
268. Safonov, A.I., D.Y. Panin, and N.I. Timoshenko, *The use of molybdenum activator for deposition of fluoropolymer coatings with different structures by the hot wire chemical vapor deposition method.* Interfacial Phenomena and Heat Transfer, 2019. **7**(2).
269. Marsalek, R., *Particle size and zeta potential of ZnO.* APCBEE procedia, 2014. **9**: p. 13-17.
270. Al-Hakeim, H.K., F.F.M. Al-Kazaz, and H.K.A. Alobaid, *Adsorption of LH, FSH, and TSH on Magnetic Nanoparticles.* Journal of Bionanoscience, 2015. **9**(6): p. 439-447.
271. Al-Kazazz, F.F., H.K. Al-Hakeim, and H.K. Al-Aobaid, *Study the Interaction Between LH, FSH, and TSH with New Synthesized Magnetic Nanoparticles Coated with Dextran.* Medical Journal of Babylon, 2016. **13**(2): p. 421-34.
272. Urbic, T., S. Najem, and C.L. Dias, *Thermodynamic properties of amyloid fibrils in equilibrium.* Biophysical chemistry, 2017. **231**: p. 155-160.
273. Strickland, T.W., T.F. Parsons, and J.G. Pierce, *Structure of LH and hCG*, in *Luteinizing Hormone Action and Receptors*. 2019, CRC Press. p. 1-15.
274. Mahmoodi, F., P. Darvishi, and B. Vaferi, *Prediction of coefficients of the Langmuir adsorption isotherm using various artificial intelligence (AI) techniques.* Journal of the Iranian Chemical Society, 2018. **15**(12): p. 2747-2757.
275. Li, J. and D.J. Mooney, *Designing hydrogels for controlled drug delivery.* Nature Reviews Materials, 2016. **1**(12): p. 1-17.

276. Kubiak, K., Z. Adamczyk, and M. Cieśla, *Fibrinogen adsorption mechanisms at the gold substrate revealed by QCM-D measurements and RSA modeling.* Colloids and Surfaces B: Biointerfaces, 2016. **139**: p. 123-131.
277. Shaker, K.S. and A.H. AbdAlsalm, *Synthesis and characterization nano structure of MnO2 via chemical method.* Engineering and Technology Journal, 2018. **36**(9 Part A).
278. Cherian, E., A. Rajan, and G. Baskar, *Synthesis of manganese dioxide nanoparticles using co-precipitation method and its antimicrobial activity.* International Journal of Modern Science and Technology, 2016. **1**(01): p. 17-22.
279. Shah, R., *et al*., *Optimisation and stability assessment of solid lipid nanoparticles using particle size and zeta potential.* Journal of Physical Science, 2014. **25**(1).
280. Kim, J. and K. Doudrick, *Emerging investigator series: protein adsorption and transformation on catalytic and food-grade TiO 2 nanoparticles in the presence of dissolved organic carbon.* Environmental Science: Nano, 2019. **6**(6): p. 1688-1703.
281. Givens, B.E., *et al*., *Adsorption of bovine serum albumin on silicon dioxide nanoparticles: Impact of p H on nanoparticle–protein interactions.* Biointerphases, 2017. **12**(2): p. 02D404.
282. Aghili, Z., *et al*., *Investigating the interaction of Fe nanoparticles with lysozyme by biophysical and molecular docking studies.* PloS one, 2016. **11**(10): p. e0164878.
283. Privalov, P.L., *Microcalorimetry of macromolecules: The physical basis of biological structures*. Vol. 16. 2012: John Wiley & Sons.
284. Tahir, S. and N. Rauf, *Thermodynamic studies of Ni (II) adsorption onto bentonite from aqueous solution.* The Journal of Chemical Thermodynamics, 2003. **35**(12).
285. Vuong, C., *et al*., *The effects of opioids and opioid analogs on animal and human endocrine systems.* Endocrine reviews, 2010. **31**(1): p. 98-132.
286. Lunger, F., *et al*., *Opiate receptor blockade on human granulosa cells inhibits VEGF release.* Reproductive biomedicine online, 2016. **32**(3): p. 316-322.
287. Seeber, B., *et al*., *Chapter Ten - Opioids and reproduction*, in *Vitamins and Hormones*, G. Litwack, Editor. 2019, Academic Press. p. 247-279.
288. Böttcher, B., *et al*., *Impact of the opioid system on the reproductive axis.* Fertility and Sterility, 2017. **108**(2): p. 207-213.
289. Zangeneh, F., *et al*., *Opioid system (β-endorphin) and stress hormones profiling in women with polycystic ovary syndrome.* Annual Research & Review in Biology, 2015: p. 409-418.

290. Jaschke, N., *et al*., *From Pharmacology to Physiology: Endocrine Functions of μ-Opioid Receptor Networks.* Trends in Endocrinology & Metabolism, 2021. **32**(5): p. 306-319.
291. Eyvazzadeh, A.D., et al., *The role of the endogenous opioid system in polycystic ovary syndrome.* Fertility and Sterility, 2009. **92**(1): p. 1-12.
292. Berent-Spillson, A., *et al*., *Insulin resistance influences central opioid activity in polycystic ovary syndrome.* Fertility and Sterility, 2011. **95**(8): p. 2494-2498.
293. Totorikaguena, L., *et al*., *Mu opioid receptor in the human endometrium: dynamics of its expression and localization during the menstrual cycle.* Fertility and Sterility, 2017. **107**(4): p. 1070-1077.e1.
294. Li, M., *et al*., *Serum Macroelement and Microelement Concentrations in Patients with Polycystic Ovary Syndrome: a Cross-Sectional Study.* Biol Trace Elem Res, 2017. **176**(1): p. 73-80.
295. Kadoura, S., M. Alhalabi, and A.H. Nattouf, *Effect of Calcium and Vitamin D Supplements as an Adjuvant Therapy to Metformin on Menstrual Cycle Abnormalities, Hormonal Profile, and IGF-1 System in Polycystic Ovary Syndrome Patients: A Randomized, Placebo-Controlled Clinical Trial.* Advances in pharmacological sciences, 2019. **2019**: p. 9680390-9680390.
296. Thys-Jacobs, S., *et al*., *Vitamin D and calcium dysregulation in the polycystic ovarian syndrome.* Steroids, 1999. **64**(6): p. 430-5.
297. Hahn, S., *et al*., *Low serum 25-hydroxyvitamin D concentrations are associated with insulin resistance and obesity in women with polycystic ovary syndrome.* Experimental and Clinical Endocrinology & Diabetes, 2006. **114**(10): p. 577-583.
298. Pal, L., *et al*., *Therapeutic implications of vitamin D and calcium in overweight women with polycystic ovary syndrome.* Gynecol Endocrinol, 2012. **28**(12): p. 965-8.
299. Mahmoudi, T., *et al*., *Calciotropic hormones, insulin resistance, and the polycystic ovary syndrome.* Fertil Steril, 2010. **93**(4): p. 1208-14.
300. Maktabi, M., M. Jamilian, and Z. Asemi, *Magnesium-zinc-calcium-vitamin D co-supplementation improves hormonal profiles, biomarkers of inflammation and oxidative stress in women with polycystic ovary syndrome: a randomized, double-blind, placebo-controlled trial.* Biological trace element research, 2018. **182**(1): p. 21-28.
301. Barbagallo, M., N. Veronese, and L.J. Dominguez, *Magnesium in aging, health and diseases.* Nutrients, 2021. **13**(2): p. 463.
302. Rizzo, M., A. Abbatecola, and M. Barbieri, *Evidence for anti-inflammatory effects of combined administration of vitamin E and C*

in older persons with impaired fasting glucose: impact on insulin action. Alternative Medicine Review, 2009. **14**(1): p. 84-85.
303. Levitt, D.G. and M.D. Levitt, *Human serum albumin homeostasis: a new look at the roles of synthesis, catabolism, renal and gastrointestinal excretion, and the clinical value of serum albumin measurements.* Int J Gen Med, 2016. **9**: p. 229-55.
304. Zeginiadou, T., *et al*., *Nonlinear binding of sex steroids to albumin and sex hormone binding globulin.* Eur J Drug Metab Pharmacokinet, 1997. **22**(3): p. 229-35.
305. Kalyan, S., *et al*., *Cardiovascular and metabolic effects of medroxyprogesterone acetate versus conjugated equine estrogen after premenopausal hysterectomy with bilateral ovariectomy.* Pharmacotherapy, 2010. **30**(5): p. 442-52.
306. Kalyan, S., *et al*., *Competing Factors Link to Bone Health in Polycystic Ovary Syndrome: Chronic Low-Grade Inflammation Takes a Toll.* Sci Rep, 2017. **7**(1): p. 3432.
307. Kalyan, S., *et al*., *Assessing C reactive protein/albumin ratio as a new biomarker for polycystic ovary syndrome: a case–control study of women from Bahraini medical clinics.* BMJ open, 2018. **8**(10): p. e021860.
308. Kalyan, S., *et al*., *Competing factors link to bone health in polycystic ovary syndrome: chronic low-grade inflammation takes a toll.* Scientific reports, 2017. **7**(1): p. 1-8.
309. Muneyyirci-Delale, O., *et al*., *Divalent cations in women with PCOS: implications for cardiovascular disease.* Gynecological endocrinology, 2001. **15**(3): p. 198-201.
310. Shaba'a, S.M., *Is lipid profile in women with polycystic ovary syndrome related to calcium or magnesium in serum?* journal of kerbala university, 2009. **7**(2).
311. Abdul Kadhem, M., *et al*., *Is lipid profile in women with polycystic ovary syndrome related to calcium or magnesium in serum?* journal of kerbala university, 2008. **4**(4): p. 150-157.
312. Barber, T.M. and S. Franks, *Obesity and polycystic ovary syndrome.* Clinical endocrinology, 2021. **95**(4): p. 531-541.
313. Young, S.L. and B.A. Lessey. *Progesterone function in human endometrium: clinical perspectives*. in *Seminars in reproductive medicine*. 2010. © Thieme Medical Publishers.
314. Pasquali, R., *et al*., *PCOS Forum: research in polycystic ovary syndrome today and tomorrow.* Clinical endocrinology, 2011. **74**(4): p. 424-433.
315. Delcour, C., *et al*., *PCOS and Hyperprolactinemia: what do we know in 2019?* Clinical Medicine Insights: Reproductive Health, 2019. **13**: p. 1179558119871921.

316. Szosland, K., P. Pawłowicz, and A. Lewiński, *Prolactin secretion in polycystic ovary syndrome (PCOS).* Neuroendocrinology Letters, 2015. **36**(1).
317. Murdoch, A., W. Dunlop, and P. Kendall-Taylor, *Studies of prolactin secretion in polycystic ovary syndrome.* Clinical endocrinology, 1986. **24**(2): p. 165-175.
318. Franks, S., *Regulation of prolactin secretion by oestrogens: physiological and pathological significance.* Clinical Science, 1983. **65**(5): p. 457-462.
319. Cumming, D., *et al*., *Evidence for decreased endogenous dopamine and opioid inhibitory influences on LH secretion in polycystic ovary syndrome.* Clinical endocrinology, 1984. **20**(6): p. 643-648.
320. Davoudi, Z., *et al*., *Prolactin Level in Polycystic Ovary Syndrome (PCOS): An approach to the diagnosis and management.* Acta Biomed, 2021. **92**(5): p. e2021291.
321. Melgar, V., *et al*., *Current diagnosis and treatment of hyperprolactinemia.* Revista Médica del Instituto Mexicano del Seguro Social, 2016. **54**(1): p. 110-121.
322. Webster, J., *Dopamine agonist therapy in hyperprolactinemia.* The Journal of reproductive medicine, 1999. **44**(12 Suppl): p. 1105-1110.
323. Soto-Pedre, E., *et al*., *The epidemiology of hyperprolactinaemia over 20 years in the Tayside region of Scotland: the Prolactin Epidemiology, Audit and Research Study (PROLEARS).* Clinical endocrinology, 2017. **86**(1): p. 60-67.
324. Serri, O., *et al*., *Diagnosis and management of hyperprolactinemia.* Cmaj, 2003. **169**(6): p. 575-581.
325. Vilar, L., M. Fleseriu, and M.D. Bronstein, *Challenges and pitfalls in the diagnosis of hyperprolactinemia.* Arquivos Brasileiros de Endocrinologia & Metabologia, 2014. **58**: p. 9-22.
326. Vilar, L., *et al*., *Controversial issues in the management of hyperprolactinemia and prolactinomas–An overview by the Neuroendocrinology Department of the Brazilian Society of Endocrinology and Metabolism.* Archives of endocrinology and metabolism, 2018. **62**: p. 236-263.
327. Carmina, E. and R.A. Lobo, *Is there really increased cardiovascular morbidity in women with polycystic ovary syndrome?* Journal of women's health, 2018. **27**(11): p. 1385-1388.
328. Giton, F., *et al*., *Determination of Bioavailable Testosterone [Non–Sex Hormone–Binding Globulin (SHBG)-Bound Testosterone] in a Population of Healthy French Men: Influence of Androstenediol on Testosterone Binding to SHBG.* Clinical chemistry, 2007. **53**(12): p. 2160-2168.

329. Winters, S.J., *et al*., *Serum testosterone levels decrease in middle age in women with the polycystic ovary syndrome.* Fertility and sterility, 2000. **73**(4): p. 724-729.
330. Maffre, P., *et al*., *Effects of surface functionalization on the adsorption of human serum albumin onto nanoparticles–a fluorescence correlation spectroscopy study.* Beilstein journal of nanotechnology, 2014. **5**(1): p. 2036-2047.
331. Lutsey, P.L., *et al*., *Serum magnesium, phosphorus, and calcium are associated with risk of incident heart failure: the Atherosclerosis Risk in Communities (ARIC) Study.* The American journal of clinical nutrition, 2014. **100**(3): p. 756-764.
332. Deilamy Pour, H., *et al*., *Synergistic effects of selenium and magnesium nanoparticles on growth, digestive enzymes, some serum biochemical parameters and immunity of Asian sea bass (Lates calcarifer).* Biological Trace Element Research, 2021. **199**(8): p. 3102-3111.
333. Roelfsema, F., *et al*., *Dynamic interactions between LH and testosterone in healthy community-dwelling men: impact of age and body composition.* The Journal of Clinical Endocrinology & Metabolism, 2020. **105**(3): p. e628-e641.
334. Watkins, J.D., *et al*., *Plasma glucagon-like peptide-1 responses to ingestion of protein with increasing doses of milk minerals rich in calcium.* British Journal of Nutrition, 2021: p. 1-9.
335. Gjergjizi, B., *et al*., *SERS-based ultrafast and sensitive detection of luteinizing hormone in human serum using a passive microchip.* Sensors and Actuators B: Chemical, 2018. **269**: p. 314-321.